


2023

Solid State NMR Analysis of Insect Wing Membranes

Samuel Eddy
sdeddy@mix.wvu.edu

Follow this and additional works at: <https://researchrepository.wvu.edu/etd>

 Part of the [Materials Chemistry Commons](#), and the [Physical Chemistry Commons](#)

Recommended Citation

Eddy, Samuel, "Solid State NMR Analysis of Insect Wing Membranes" (2023). *Graduate Theses, Dissertations, and Problem Reports*. 12255.
<https://researchrepository.wvu.edu/etd/12255>

This Dissertation is protected by copyright and/or related rights. It has been brought to you by the The Research Repository @ WVU with permission from the rights-holder(s). You are free to use this Dissertation in any way that is permitted by the copyright and related rights legislation that applies to your use. For other uses you must obtain permission from the rights-holder(s) directly, unless additional rights are indicated by a Creative Commons license in the record and/ or on the work itself. This Dissertation has been accepted for inclusion in WVU Graduate Theses, Dissertations, and Problem Reports collection by an authorized administrator of The Research Repository @ WVU. For more information, please contact researchrepository@mail.wvu.edu.

Solid State NMR Analysis of Insect Wing Membranes

Samuel Eddy

Dissertation submitted to the
Eberly College of Arts and Sciences
At West Virginia University

In partial fulfillment of the requirements for the degree of
Doctor of Philosophy in
Department of Chemistry/Physical Chemistry

Terry Gullion, Ph.D., Chair
Fabien Goulay Ph.D.
Justin Legleiter Ph.D.
Blake Mertz Ph.D.
Matt Kasson Ph.D.

C. Eugene Bennett Department of Chemistry

Morgantown West Virginia

2023

Keywords: Solid State NMR, DNP, C13-C13 DQ/SQ Natural Abundance, Insect Wing, Wing

Membrane, Chitin, Cicada, Honeybee, Butterfly, Ladybug

© Copyright by
Samuel Eddy
2023

Abstract

Solid State NMR Analysis of Insect Wing Membranes

Samuel Eddy

Solid State NMR is a powerful tool for analyzing the chemical composition of insects. Previous studies have used Solid State NMR to investigate the chemical composition and investigate the sclerotization (tanning) process of insect exoskeletons. Acquiring sufficient exoskeleton sample for analysis has been relatively simple. This is however not the case for other components of an insect's physiology, particularly the wing membrane material. The wings of an insect only compose a small percentage of their overall body mass, and many hundreds to thousands of insects must be processed in order to achieve a few milligrams of wing membrane sample. The wing membranes which are in our interest are particularly challenging to collect as they are very small, surrounded by unwanted veins, extremely thin and nearly transparent. Compounding these difficulties is the factor of NMR signal strength due to low ^{13}C isotopic natural abundance. The task of isotopically labelling living organisms such as insects ranges from challenging to impossible. Consequently NMR signal enhancement techniques are necessary to generate high quality useful spectra.

Solid State NMR has been used to investigate the chemical composition of the wing membranes of cicadas (*Magicicada cassini*), honeybees (*Apis mellifera ligustica*), ladybugs (*Hippodamia convergens*), and amber phantom butterflies (*Haetera piera*). DNP-MAS Solid State NMR has been used to investigate the chemical composition of cicada wing membranes of a small natural abundance sample, yielding high quality one-dimensional and two-dimensional spectra.

Dedication

This is dedicated to my wife Meredith Eddy and my parents Matthew and Gaylyn Eddy.
You always believed in me and supported me, without that I would not have made it this far.

This is the day which the LORD has made;

Let's rejoice and be glad in it.

Psalm 118:24

But in all these things we overwhelmingly conquer through Him who loved us.

Romans 8:37

Acknowledgements

I would first like to acknowledge my research advisor Dr. Terry Gullion. I want to thank you for all your support and guidance throughout this endeavor. Your patience and insightful instruction made all of this possible. I would also like to thank Dr. Frederic Mentink-Vigier from the National High Magnetic Field Lab, who made the DNP and low temperature studies possible. I would like to thank Allen Burns who expertly machined many tools and fixtures which made this work possible. I would like to thank Gregory Lusk for providing insight and assistance in electronic circuit design and repair. I would like to thank Trenton M. Paul, Kayla Hollis, Garrett Riggleman, and John Gullion who spent many hours with me dissecting insect wings.

I would like to thank my family for supporting my continuing education and work towards this terminal degree, your patience and support were invaluable, and without it I would not have been able to do this. Thank you all for everything.

Table of Contents

Abstract	ii
Dedication.....	iii
Acknowledgments.....	iv
List of Figures.....	vii
List of Tables	ix
Chapter 1 introduction.....	1
Chapter 2 NMR background.....	14
2.1 The Zeeman energy	14
2.2 The Sensitivity Issue	16
2.3 Spin Temperature	20
2.4 Cross Polarization: A Thermodynamic view	24
2.5 Spin Dynamics in the Rotating Frame	27
2.6 The Cross Polarization Experiment	30
2.7 Dynamic Nuclear Polarization, the Overhauser Effect.....	33
2.8 Signal Averaging	39
2.9 Chemical Shift Anisotropy and Magic-Angle Spinning NMR.....	40
Chapter 3 harvesting Insect Wing membranes	50
3.1 Cicada	50
3.2 Honeybee.....	52
3.3 Ladybug	53
3.4 Amber Phantom Butterfly	54
3.5 Measuring the Thickness of Insect Wing Membranes.....	55
3.6 Purifying Chitin from Cicada Slough	58
3.7 NMR Experiment Parameters	62
Chapter 4 Results and Discussion.....	66
4.1 Introduction	66
4.2 Membrane Thickness of Insect Wings.....	67

4.3 Surface Hairs	69
4.4 ¹ H- ¹³ C CPMAS NMR of Ladybug Elytra.....	76
4.5 ¹ H- ¹³ C CPMAS NMR of Cicada, Ladybug, Honeybee and Butterfly wing membranes	84
4.6 MAS-DNP NMR	88
Chapter 5 NMR of Chitin	98
Chapter 6 Summary and Important Findings	105

List of Figures

Figure 1.1 Cross section of the exoskeleton.....	3
Figure 1.2 Formation of the insect wing	4
Figure 1.3 Cicada wing	4
Figure 2.1 The Zeeman splitting for a spin $I=1/2$ nucleus in an applied Zeeman field.....	15
Figure 2.2 Static Magnetic field, increasing temperature yields a decrease in magnetization.....	20
Figure 2.3 Fixed Magnetization with decreasing Zeeman field	21
Figure 2.4 An arrangement of non-equilibrium spin populations.....	23
Figure 2.5 CP pulse sequence with an inset graph of cross polarization ^{13}C magnetization buildup.....	31
Figure 2.6 Energy diagram for an electron-nuclear spin system	34
Figure 2.7 Single crystal ^{13}C Solid state NMR spectrum of the carboxylate carbon in alanine ...	41
Figure 2.8 The crystal unit cell of L-Alanine	42
Figure 2.9 The static powder pattern ^{13}C NMR spectra of the carboxylate carbon of L-alanine ..	43
Figure 2.10 A depiction of the sample rotation axis set at the magic angle relative to the Zeeman field	45
Figure 2.11 ^{13}C spectra of the carboxylate carbon of L-Alanine spun at different spinning rates from static 0 Hz to 3000 Hz.....	46
Figure 2.12 ^{13}C NMR spectra of the carboxylate carbon of L-alanine in solution, solid with a spinning rate of 3000 Hz, and a static sample	47
Figure 2.13 ^{13}C MAS NMR spectrum of $[\text{Cs}(\text{p-tert-butylcalix}[4]\text{arene -H})(\text{MeCN})]$	48
Figure 3.1 An image of a cicada wing.....	51
Figure 3.2 A close-up image of a cicada wing held in place for dissection	51
Figure 3.3 A honeybee forewing.....	52
Figure 3.4 A ladybug wing	53
Figure 3.5 An amber phantom butterfly	54
Figure 3.6 The 100-micrometer scale at A) 10x, B) 20x, and C) 50x magnification	55

Figure 3.7 Wire viewed under the microscope as scale reference	56
Figure 3.8 Image of the cicada sloughs prior to processing	59
Figure 3.9 Image of the final chitin product after drying	61
Figure 4.1 Edges of wing membranes.....	68
Figure 4.2 Wing membrane hair images	70
Figure 4.3 Volume of a honeybee wing membrane hair was calculation.....	71
Figure 4.4 The process of generating splines to determine the length of the butterfly hairs	73
Figure 4.5 N-acetylglucosamine, the chitin repeat unit	77
Figure 4.6 ¹³ C CPMAS spectra of the wild type rice weevil (<i>Sitophilus Oryzae</i>) cuticle	77
Figure 4.7 The comparison of the ¹ H- ¹³ C CPMAS spectra of ladybug elytra.....	80
Figure 4.8 A diagram of how catechols facilitate sclerotization crosslinking between protein and chitin via a histidine residue	81
Figure 4.9 The ¹³ C CPMAS spectra of the ladybug elytron after acetone washing compared to the spectra of the ladybug membrane.....	83
Figure 4.10 Comparison of the ¹³ C CPMAS spectra of the membranes harvested from the butterfly, cicada, ladybug, and honeybee	85
Figure 4.11 The ¹³ C CPMAS spectra of the wing membranes of the Cicada, Ladybug and Honeybee.....	87
Figure 4.12 The ¹ H- ¹³ C CPMAS spectra of cicada wing membrane, showing results with DNP off (top scaled by 5x) and DNP on (bottom)	90
Figure 4.13 The natural abundance ¹³ C- ¹³ C double-quantum/single-quantum spectra of the cicada wing membrane.....	91
Figure 4.14 (Left) The center section of the 2D spectra in Figure 4.13 4.2.....	93
Figure 5.1 NMR spectra of purified chitin at 300°K and at 100°K.....	98
Figure 5.2 Two zoomed in and cutout portions of the spectra from in Figure 5.1	100
Figure 5.3 Diagram of a crystal unit cell.....	101
Figure 5.4 Structure of α-Chitin at 100°K and 300°K	102

List of Tables

Table 3.1 Pixel to micron measurements at 10x, 20x, and 50x magnification.....	57
Table 4.1 Summary of the physical characteristics of the insect wing membranes	75
Table 4.2 ¹³ C isotropic chemical shifts for components common to insect cuticle.....	76
Table 5.1 α -Chitin unit cell parameters at 100°K and 300°K	101

Chapter 1 Introduction

Insects are six-legged invertebrates that form the class *Insecta*, which is found in the arthropod phylum. The term “insect” comes from the Latin *insectum*, which means divided into segments. The segmented insect body is composed of the head, thorax, and abdomen. Insects are among the earliest land animals and have existed for over 400 million years [1]. For comparison, the earliest mammal like creatures appeared 225 million years ago [2]. Insects are, by far, the most widely varied class of animals and account for over 75 percent of all species of animals identified [3-6]. Insects are found on every continent; for example, the Antarctic midge is the sole, native insect of Antarctica [7]. Insects play an essential role in our world; after all, as E. O. Wilson pointed out, “If all mankind were to disappear, the world would regenerate back to the rich state of equilibrium that existed ten thousand years ago. If insects were to vanish, the environment would collapse into chaos.” Insects are the most dominant form of animal life on the planet. The number of insect species is greater than one million and exceeds the number of species of all other taxa combined [3]. The population of insects is estimated to exceed a quintillion (10^{18}), or over one hundred million insects for every person [8]. The dominance of insects can be attributed to many factors, with their robust exoskeleton and their ability to fly as among the most important.

Insects lack bones or an endoskeletal structure to support them. Instead, they have exoskeletons [3, 9-13]. The exoskeleton is a rigid barrier that completely surrounds the insect's body. It serves to protect the insect from predators and environmental hazards, provides body support, inhibits moisture loss, and is a means of locomotion for the insect. [3, 9-13]. It must be mechanically and chemically sophisticated to perform all these functions for the insect. The

exoskeleton of an insect is often referred to as cuticle, and these terms are often used interchangeably.

Figure 1.1 shows a cross section of the exoskeleton. The exoskeleton is a layered structure consisting of (spanning from the inside to the outside) the basement membrane, epidermis, endocuticle, mesocuticle, exocuticle, and epicuticle. The exocuticle, mesocuticle, and endocuticle are collectively referred to as the procuticle [3, 9-13]. The basement membrane is made of polysaccharide and serves to separate the body cavity from the epidermis. The only living part of the exoskeleton is the epidermis, which is a single layer of cells and houses dermal glands, sensory receptors, and oenocytes [11]. The oenocytes produce lipids that coat the epicuticle. Trichogen cells produce the seta (hairs) that appear on the outer surface of the exoskeleton [11]. The epidermal cells produce, in the following order: the epicuticle, exocuticle, mesocuticle, and endocuticle [3, 9-13]. These nonliving layers are collectively known as the cuticle. The epicuticle is typically 0.5 to 2.0 μm thick [11]. The exact chemical composition of the epicuticle is not known but does contain quinones and polyphenols. It is important to note that no chitin has been observed to occur in the epicuticle. The procuticle region is typically between 10 and 200 μm thick and contains chitin and protein [11]. The proteins in the exocuticle are cross-linked to a great extent; however, less cross-linking of the proteins is observed in the thicker endocuticle. The degree of cross-linking has a strong effect on the overall properties of the exoskeleton. Cross-linking between chitin and protein has also been detected in the cuticle by solid-state NMR experiments. Not all insects have a mesocuticle, which is thought to be a transitional layer between the endocuticle and exocuticle.

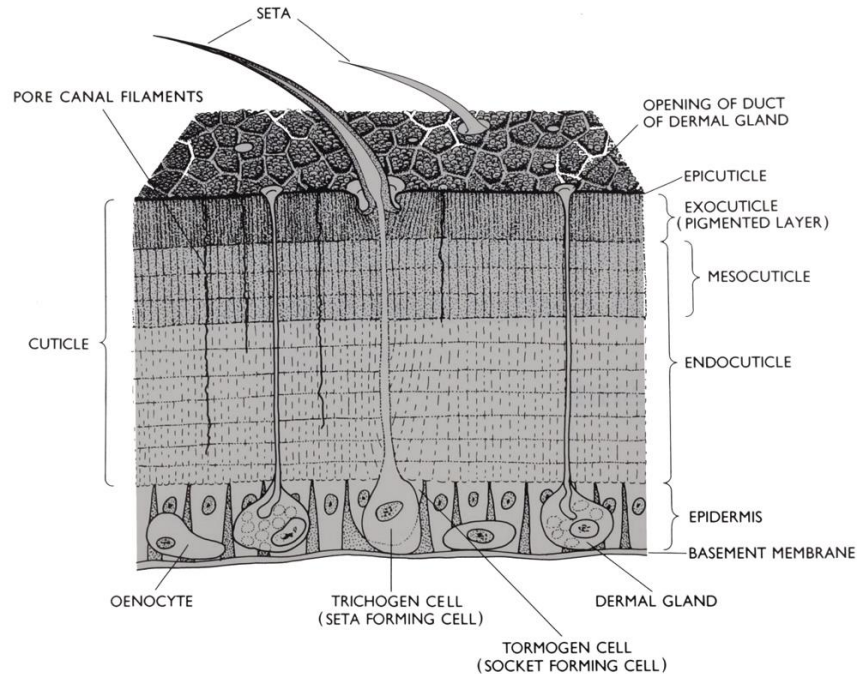


Figure 1.1 Cross section of the exoskeleton. Taken from Klowden [11].

The insect wing is considered an extension of the exoskeleton. However, the wing and the exoskeleton are structurally very different. Figure 2 shows the textbook model of insect wing formation during pupal development. Wing formation begins with an outgrowth sandwich structure of epidermal cells lining the interior of a folded portion of epicuticle, such that the layers from top to bottom are epicuticle, epidermis, another epidermal layer, and epicuticle [11]. In the center of this sandwich formation are hollow trachea, which facilitate the transport of hemolymph throughout the body of the insect. [11]. The sandwich structure becomes thinner as the pupation process progresses, and the epidermal cells lining the inner surface of the epicuticle degenerate and are reabsorbed once the insect has emerged in its adult form [11]. The trachea become chitin-rich veins, and the wing membrane is made of chitin-free epicuticle according to this model. Thus, if the membrane is made of only epicuticle, then the membrane would be

expected to be only a few microns thick [11,14]. Figure 1.3 is a picture of a mature cicada wing showing the motif of veins surrounding regions of membrane.

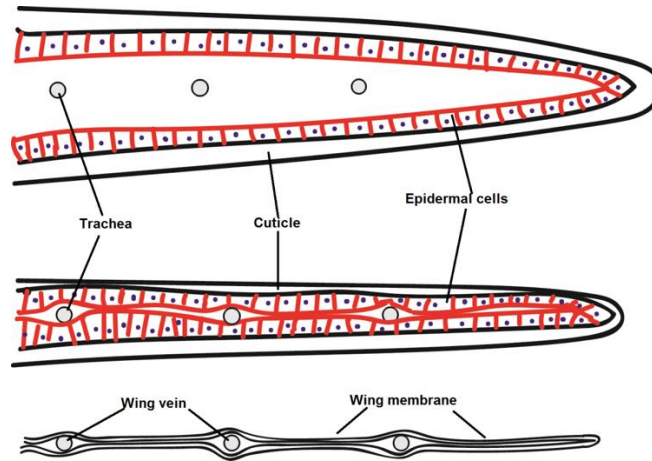


Figure 1.2. Formation of the insect wing.



Figure 1.3. Cicada wing. The dark lines are veins, and the translucent regions outlined by veins are membranes.

The macroscopic structure of insect wings is similar throughout the species of insects. Flying insects typically have two pairs of wings, the forewing and the hindwing. Wings responsible for flight (see caveat below) are made of a network of veins and a thin membrane. The hollow veins provide structural rigidity, serve as a conduit for hemolymph and sensory information, and prevent tears in the membrane from spreading throughout the wing. The latter property is especially important since insect wings lack a repair mechanism when damaged [15]. In some insects (e.g., beetles), the forewing is thickened and hardened and serves to protect the

hindwing [16]. In such cases, the hardened forewing is the elytron. The elytron does not have the vein/membrane structure; instead, the elytron appears as a hard shell. When ready for flight, the two elytra open to expose the membranous hindwings responsible for flight.

The wing is anchored to the body of the insect through a flexible, hinge-like joint, the axilla, next to the dorsal or back section of the thorax [17]. This joint must support the weight of the entire insect and allow enough flexibility for controlled flight [17]. Unlike bird or bat wings, insect wings contain no muscles to deform the wing and help control their flight [17,18]. This limits insects into relying upon the passive wing deformations afforded by their wings natural flexibility.

While the general macroscopic wing structures are similar, different insects may have novel wing morphologies to suit their specific needs. Those morphological differences are distinct from each other due to their adaptation to the lifestyle and living environment of the individual insect species. For example, dragonflies are aerial predators; they hunt for other insects in the air and need to fly faster than their prey. Their wings must be rigid and light enough to allow them to maneuver in flight with great swiftness in pursuit of their prey. Moreover, they must be able to fly efficiently so that they can maintain the energy needs of their bodies by consuming their prey and not incur a caloric deficit. The dragonfly's wings have a large surface area which allows the insect to passively glide for extended periods of time without having to flap their wings. Thus, dragonflies conserve energy in flight while maintaining their position on the lookout for prey. In addition to the energy savings that gliding during flight provides, dragonflies are also able to use periods of gliding to help regulate their body temperature [19]. This temperature regulation takes advantage of the large surface area and the dense vein structure of the dragonfly wings by allowing the hemolymph to flow through the

many small veins present in the wings. The air flowing over the wings during the glide can wick away the thermal energy in the hemolymph in the wing veins; the cooled hemolymph returns to the insect body to help maintain a suitable internal body temperature.

Ladybugs are terrestrial predators. Unlike dragonflies, ladybugs do not pursue prey during flight but use their wings to fly in search for food [20]. This doesn't require that they fly particularly fast or with great agility, they just need to be able to cover the distance. Ladybugs are beetles, and their forewings are elytra, which serve to protect the hindwings [16]. A special requirement of ladybug hindwings is the need to fold underneath the elytra when not in flight [21]. Before a flight, the ladybug must open its elytra to allow the hindwings stored underneath the elytra to take on their flight-ready configuration [21]. After the flight, the ladybug must close the elytra and fold its wings underneath the elytra for protection [21]. The ability of the hindwings to unfold and fold is due to the presence of resilin, an elastic protein, that is present along a crease in the wing.

Although the mechanical and morphological properties of insect wings have been well studied through experiments that probe the surface properties and surface chemistry of the insect wings, less is known about their chemical composition and macromolecular ordering [22-30]. The textbook model of the mature wing membrane is simply epicuticle on the dorsal and ventral sides of the wing and nothing in between, with the epicuticle consisting of lipids and protein, and free of chitin [11]. Mass-spectrometry experiments performed on the wing membrane of the desert locust (*Schistocerca gregaria*) found no evidence for chitin [23], which supports the textbook model, but birefringent studies reported the presence of chitin [17]. Recent SEM cross-sectional images of dragonfly (*Hemianax papuensis*) wings show a more complex picture of the wing membranes, consisting of thin epicuticle layers on the dorsal and ventral sides that

sandwich a thicker intercuticle layer [24, 31]. The average thickness of the dragonfly epicuticle was 513 nanometers for the dorsal epicuticle layer and 356 nanometers for the ventral epicuticle [31]. The intercuticle layer is approximately 2 micrometers thick and is proposed to be made of 2 chitin-containing exocuticle layers that sandwich a mesocuticle layer [18,31]. It is evident that the chemical and physical structure of insect wings may be more complex than originally assumed. Accordingly, the goal of this research is to determine the chemical composition of the wing membranes for a variety of insects. Specifically, does the insect wing membrane contain, in addition to protein, chitin and other chemical components? Do all insects share the same chemical composition or are there variations that serve the flight needs of specific insects?

To begin answering these questions, solid-state NMR is used to determine the chemical makeup of the wing membranes of cicada, ladybug, honeybee, and butterfly. Wing membranes are insoluble and composed of macromolecular components. High-resolution solid-state NMR is a good tool for such materials because it does not require crystalline materials, examines the materials in their natural state, and can provide ^{13}C resonances at high resolution. Solid-state NMR has a long, proven history of determining macromolecular compositions and chemical structures and is well-suited for the problem at hand [32-40].

It will be shown that chitin is present in the wing membranes for all these insects, but in differing amounts relative to protein. In addition, catechols are present in two of the insects and not detected in the other two. Catechols are important as cross-linking agents, and the presence or absence of catechols may determine the stiffness of the insect wing.

While investigating the insect-wing membranes, an unusual observation was made regarding pure chitin. The high-resolution, solid-state ^{13}C NMR spectrum of pure chitin obtained at room temperature is different than the spectrum obtained at 100 K. In contrast, structures of

pure chitin obtained by X-ray crystallography obtained at those two temperatures are identical. It is proposed that chitin undergoes an order-disorder phase transition involving hydroxy groups to account for the differences between the X-ray crystallography results and the solid-state NMR results.

References

1. Misof, B.; Liu, S.; Meusemann, K.; Peters, R. S.; Donath, A.; Mayer, C.; Frandsen, P. B.; Ware, J.; Flouri, T.; Beutel, R. G.; Niehuis, O.; Petersen, M.; Izquierdo-Carrasco, F.; Wappler, T.; Rust, J.; Aberer, A. J.; Aspöck, U.; Aspöck, H.; Bartel, D.; Blanke, A. Phylogenomics Resolves the Timing and Pattern of Insect Evolution. *Science* **2014**, *346* (6210), 763–767. <https://doi.org/10.1126/science.1257570>.
2. Novacek, M. J. Mammalian Evolution: An Early Record Bristling with Evidence. *Current Biology* **1997**, *7* (8), R489–R491. [https://doi.org/10.1016/s0960-9822\(06\)00245-4](https://doi.org/10.1016/s0960-9822(06)00245-4).
3. Chapman, R. F.; Simpson, S. J.; Douglas, A. E. *The Insects : Structure and Function*; Cambridge University Press: New York, 2013.
4. Hoffmann, M. P.; Frodsham, A. *Natural Enemies of Vegetable Insect Pests*; 1993.
5. Grimaldi, D. A.; Engel, M. S. *Evolution of the Insects*; Cambridge University Press: Cambridge U.K. ; New York, 2005.
6. Species 2000 & ITIS Catalogue of Life, 2016 Annual Checklist; Roskov, Y., Abucay, L., Orrell, T., Nicolson, D., Flann, C., Bailly, N., Kirk, P., Bourgoin, T., DeWalt, R. E., Decock, W., De Wever, A., Eds.; 2016. Digital resource at www.catalogueoflife.org/annual-checklist/2016. Species 2000: Naturalis: Leiden, the Netherlands.
7. Teets, N. M.; Kawarasaki, Y.; Potts, L. J.; Philip, B. N.; Gantz, J. D.; Denlinger, D. L.; Lee, R. E. Rapid Cold Hardening Protects against Sublethal Freezing Injury in an Antarctic Insect. *Journal of Experimental Biology* **2019**, *222* (15). <https://doi.org/10.1242/jeb.206011>.
8. *Frequently Asked Questions on Entomology | Entomological Society of America (ESA)*. web.archive.org. <https://web.archive.org/web/20150207042705/https://www.entsoc.org/resources/faq/#triv1>.
9. Neville, A. C. *Biology of the Arthropod Cuticle*; Springer Science & Business Media, 2012.
10. Filshie, B. K. In *Insect Ultrastructure*; King, R. C., Akai, H., Eds.; Plenum Press: New York, NY, 1982; pp 281-312

11. Klowden, M. J. *Physiological Systems in Insects*; Elsevier/Academic Press: Amsterdam ; Boston, 2007.
12. Andersen, S. O. In *Encyclopedia of Insects*; Resh, V. H., Carde, R. T., Eds.; Academic Press: New York, NY, 2009; pp 245-246.
13. Wootton, R. J. In *Encyclopedia of Insects*; Resh, V. H., Carde, R. T., Eds.; Academic Press: New York, NY, 2009; pp 1055-1061.
14. Starkweather, R. M.; Poroseva, S. V.; Hanson, D. T. On the Shape of Cicada's Wing Leading-Edge Cross Section. *Scientific Reports* **2021**, *11* (1), 7763. <https://doi.org/10.1038/s41598-021-87504-4>.
15. Rajabi, H.; Dirks, J.-H.; Gorb, S. N. Insect Wing Damage: Causes, Consequences and Compensatory Mechanisms. *The Journal of Experimental Biology* **2020**, *223* (9), jeb215194. <https://doi.org/10.1242/jeb.215194>.
16. Noh, M. Y.; Muthukrishnan, S.; Kramer, K. J.; Arakane, Y. Development and Ultrastructure of the Rigid Dorsal and Flexible Ventral Cuticles of the Elytron of the Red Flour Beetle, *Tribolium Castaneum*. *Insect Biochemistry and Molecular Biology* **2017**, *91*, 21–33. <https://doi.org/10.1016/j.ibmb.2017.11.003>.
17. Wootton, R. J. Functional Morphology of Insect Wings. *Annual Review of Entomology* **1992**, *37* (1), 113–140. <https://doi.org/10.1146/annurev.en.37.010192.000553>.
18. Pass, G. Beyond Aerodynamics: The Critical Roles of the Circulatory and Tracheal Systems in Maintaining Insect Wing Functionality. *Arthropod Structure & Development* **2018**, *47* (4), 391–407. <https://doi.org/10.1016/j.asd.2018.05.004>.
19. Wakeling, J.; Ellington, C. Dragonfly Flight. I. Gliding Flight and Steady-State Aerodynamic Forces. *Journal of Experimental Biology* **1997**, *200* (3), 543–556. <https://doi.org/10.1242/jeb.200.3.543>.
20. Jeffries, D. L.; Chapman, J.; Roy, H. E.; Humphries, S.; Harrington, R.; Brown, P. M. J.; Handley, Lori-J. L. Characteristics and Drivers of High-Altitude Ladybird Flight: Insights from Vertical-Looking Entomological Radar. *PLoS ONE* **2013**, *8* (12), e82278. <https://doi.org/10.1371/journal.pone.0082278>.
21. Saito, K.; Nomura, S.; Yamamoto, S.; Niiyama, R.; Okabe, Y. Investigation of Hindwing Folding in Ladybird Beetles by Artificial Elytron Transplantation and Microcomputed Tomography. *Proceedings of the National Academy of Sciences* **2017**, *114* (22), 5624–5628. <https://doi.org/10.1073/pnas.1620612114>.

22. Tobin, M. J.; Puskar, L.; Hasan, J.; Webb, H. K.; Hirschmugl, C. J.; Nasse, M. J.; Gervinskas, G.; Juodkazis, S.; Watson, G. S.; Watson, J. A.; Crawford, R. J.; Ivanova, E. P. High-Spatial-Resolution Mapping of Superhydrophobic Cicada Wing Surface Chemistry Using Infrared Microspectroscopy and Infrared Imaging at Two Synchrotron Beamlines. *Journal of Synchrotron Radiation* **2013**, *20* (3), 482–489. <https://doi.org/10.1107/s0909049513004056>.
23. Smith, C. W.; Herbert, R.; Wootton, R. J.; Evans, K. E. The Hind Wing of the Desert Locust (*Schistocerca Gregaria* Forskal). II. Mechanical Properties and Functioning of the Membrane. *Journal of Experimental Biology* **2000**, *203* (19), 2933–2943. <https://doi.org/10.1242/jeb.203.19.2933>.
24. Ivanova, E. P.; Nguyen, S. H.; Webb, H. K.; Hasan, J.; Truong, V. K.; Lamb, R. N.; Duan, X.; Tobin, M. J.; Mahon, P. J.; Crawford, R. J. Molecular Organization of the Nanoscale Surface Structures of the Dragonfly *Hemianax Papuensis* Wing Epicuticle. *PLoS ONE* **2013**, *8* (7), e67893. <https://doi.org/10.1371/journal.pone.0067893>.
25. Román- Kustas, J.; Hoffman, J. B.; Reed, J. H.; Gonsalves, A. E.; Oh, J.; Li, L.; Hong, S.; Jo, K. D.; Dana, C. E.; Miljkovic, N.; Cropek, D. M.; Alleyne, M. Molecular and Topographical Organization: Influence on Cicada Wing Wettability and Bactericidal Properties. *Advanced Materials Interfaces* **2020**, *7* (10), 2000112. <https://doi.org/10.1002/admi.202000112>.
26. Appel, E.; Heepe, L.; Lin, C.-P.; Gorb, S. N. Ultrastructure of Dragonfly Wing Veins: Composite Structure of Fibrous Material Supplemented by Resilin. *Journal of Anatomy* **2015**, *227* (4), 561–582. <https://doi.org/10.1111/joa.12362>.
27. Schroeder, T. B. H.; Houghtaling, J.; Wilts, B. D.; Mayer, M. It's Not a Bug, It's a Feature: Functional Materials in Insects. *Advanced Materials* **2018**, *30* (19), 1705322. <https://doi.org/10.1002/adma.201705322>.
28. Nguyen, S.; Webb, H.; Mahon, P.; Crawford, R.; Ivanova, E. Natural Insect and Plant Micro-/Nanostructured Surfaces: An Excellent Selection of Valuable Templates with Superhydrophobic and Self-Cleaning Properties. *Molecules* **2014**, *19* (9), 13614–13630. <https://doi.org/10.3390/molecules190913614>.
29. Román-Kustas, J.; Hoffman, J. B.; Alonso, D.; Reed, J. H.; Gonsalves, A. E.; Oh, J.; Hong, S.; Jo, K. D.; Dana, C. E.; Alleyne, M.; Miljkovic, N.; Cropek, D. M. Analysis of Cicada Wing Surface Constituents by Comprehensive Multidimensional Gas Chromatography for Species Differentiation. *Microchemical Journal* **2020**, *158*, 105089. <https://doi.org/10.1016/j.microc.2020.105089>.

30. Haas, F.; Gorb, S.; Blickhan, R. The Function of Resilin in Beetle Wings. *Proceedings of the Royal Society of London. Series B: Biological Sciences* **2000**, 267 (1451), 1375–1381. <https://doi.org/10.1098/rspb.2000.1153>.
31. Song, F.; Xiao, K. W.; Bai, K.; Bai, Y. L. Microstructure and Nanomechanical Properties of the Wing Membrane of Dragonfly. *Materials Science and Engineering: A* **2007**, 457 (1-2), 254–260. <https://doi.org/10.1016/j.msea.2007.01.136>.
32. Peter, M. G.; L Grün; Förster, H. CP/MAS-¹³C-NMR Spectra of Sclerotized Insect Cuticle and of Chitin. *Angewandte Chemie* **1984**, 23 (8), 638–639. <https://doi.org/10.1002/anie.198406381>.
33. Schaefer, J.; Kramer, K. J.; Garbow, J. R.; Jacob, G. S.; Stejskal, E. O.; Hopkins, T. L.; Speirs, R. D. Aromatic Cross-Links in Insect Cuticle: Detection by Solid-State ¹³C and ¹⁵N NMR. **1987**, 235 (4793), 1200–1204. <https://doi.org/10.1126/science.3823880>.
34. Williams, H. J.; Scott, A. I.; Woolfenden, W. R.; Grant, D. M.; S.B. Vinison; Elzen, G. W.; Baehrecke, E. H. In Vivo and Solid State ¹³C Nuclear Magnetic Resonance Studies of Tyrosine Metabolism during Insect Cuticle Formation. *Comparative biochemistry and physiology. B. Comparative biochemistry* **1988**, 89 (2), 317–321. [https://doi.org/10.1016/0305-0491\(88\)90229-5](https://doi.org/10.1016/0305-0491(88)90229-5).
35. Kramer, K. J.; Morgan, T. D.; Hopkins, T. L.; Christensen, A. M.; Schaefer, J. Solid-State ¹³C-NMR and Diphenol Analyses of Sclerotized Cuticles from Stored Product Coleoptera. *Insect Biochemistry* **1989**, 19 (8), 753–757. [https://doi.org/10.1016/0020-1790\(89\)90056-5](https://doi.org/10.1016/0020-1790(89)90056-5).
36. Kramer, K. J.; Christensen, A. M.; Morgan, T. D.; Schaefer, J.; Czaplá, T. H.; Hopkins, T. L. Analysis of Cockroach Oothecae and Exuviae by Solid-State ¹³C-NMR Spectroscopy. *Insect Biochemistry* **1991**, 21 (2), 149–156. [https://doi.org/10.1016/0020-1790\(91\)90045-g](https://doi.org/10.1016/0020-1790(91)90045-g).
37. Hopkins, T. L.; Kramer, K. J. Insect Cuticle Sclerotization. *Annual Review of Entomology* **1992**, 37 (1), 273–302. <https://doi.org/10.1146/annurev.en.37.010192.001421>.
38. Kramer, K. J.; Hopkins, T. L.; Schaefer, J. Applications of Solids NMR to the Analysis of Insect Sclerotized Structures. *Insect Biochemistry and Molecular Biology* **1995**, 25 (10), 1067–1080. [https://doi.org/10.1016/0965-1748\(95\)00053-4](https://doi.org/10.1016/0965-1748(95)00053-4).

39. Merritt, M. E.; Christensen, A. M.; Kramer, K. J.; Hopkins, T. L.; Schaefer, J. Detection of Intercatechol Cross-Links in Insect Cuticle by Solid-State Carbon-13 and Nitrogen-15 NMR. *Journal of the American Chemical Society* **1996**, *118* (45), 11278–11282. <https://doi.org/10.1021/ja961621o>.
40. Hopkins, T. L.; Starkey, S.; Xu, R.; Merritt, M. E.; Schaefer, J.; Kramer, K. J. Catechols Involved in Sclerotization of Cuticle and Egg Pods of the Grasshopper, *Melanoplus Sanguinipes*, and Their Interactions with Cuticular Proteins. *Archives of Insect Biochemistry and Physiology* **1999**, *40* (3), 119–128. [https://doi.org/10.1002/\(sici\)1520-6327\(1999\)40:3%3C119::aid-arch1%3E3.0.co;2-h](https://doi.org/10.1002/(sici)1520-6327(1999)40:3%3C119::aid-arch1%3E3.0.co;2-h).

Chapter 2 NMR Background

Solid State Nuclear Magnetic Resonance (Solid State NMR) is a powerful technique used to determine the chemical makeup and structure of many kinds of materials. Solid State NMR is however hampered by a low inherent sensitivity. Over the years many techniques such as Cross Polarization (CP) and Dynamic Nuclear Polarization (DNP) have been developed to mitigate the sensitivity challenges associated with Solid State NMR, greatly expanding the landscape of materials and samples that can be analyzed with the technique.

2.1 The Zeeman Energy

A nucleus has an intrinsic angular momentum, \vec{J} , and a magnetic moment, $\vec{\mu}$, and the two are related as

$$\vec{\mu} = \gamma \vec{J} \quad \text{Eq 2.1}$$

where γ is the gyromagnetic ratio [1-3]. \vec{J} and $\vec{\mu}$ are operators in the quantum picture, so \rightarrow will be used for vectors and $\hat{}$ will be used for operators. It is convenient to define the dimensionless operator, \hat{I} , through

$$\vec{J} = \hbar \hat{I} \quad \text{Eq 2.2}$$

where \hbar the reduced Plank constant which is Planck's constant divided by 2π . The eigenvalue of \hat{I}^2 is $I(I + 1)$, where I is an integer or half-integer, and the eigenvalues of the z-component of \hat{I} , \hat{I}_z , are $m = I, I - 1, \dots, -I$.

The classical energy of a magnetic moment in a magnetic field, \vec{B}_0 , is

$$E = -\vec{\mu} \cdot \vec{B}_0 \quad \text{Eq 2.3}$$

For $\vec{B}_0 = B_0 \hat{z}$, then $E = -\mu_z B_0$ [1-4]. This suggests the Hamiltonian of a magnetic moment in a magnetic field is [1,4]

$$\mathcal{H} = -\gamma \hbar B_0 \hat{I}_z \quad \text{Eq 2.4}$$

Since \hat{I}_z has eigenvalues $m = I, I - 1, \dots, -I$, then the time-independent quantum eigenvalue equation

$$\mathcal{H}\psi_m = E_m \psi_m \quad \text{Eq 2.5}$$

has energy eigenvalues [1-4]

$$E_m = -\gamma \hbar B_0 m \quad \text{Eq 2.6}$$

For a spin-1/2 system (e.g., ^1H and ^{13}C), the energy eigenvalues are $E_{+1/2} = -\frac{1}{2}\gamma \hbar B_0$ and $E_{-1/2} = \frac{1}{2}\gamma \hbar B_0$. For positive γ , the energy diagram of this two-level system is

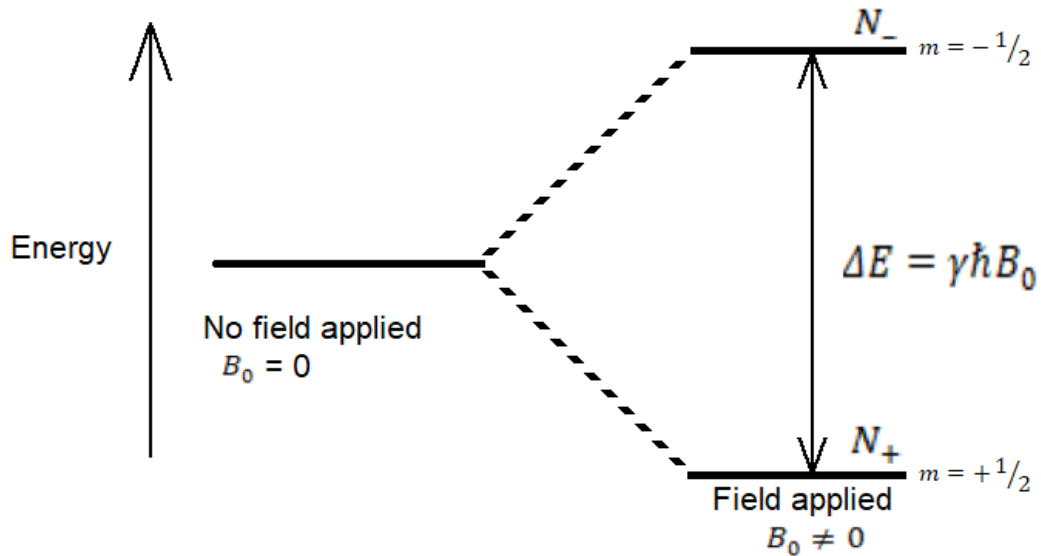


Figure 2.1 The Zeeman splitting for a spin $I = 1/2$ nucleus in an applied Zeeman field.

2.2 The Sensitivity Issue

NMR is a powerful tool, but it suffers from low sensitivity. In a direct-detection experiment, the NMR signal is proportional to the net nuclear magnetization. The net nuclear magnetization is the product of the z-component of the nuclear magnetic moment times the population difference, n , between the two energy states. With N_- and N_+ being the populations of the upper and lower energy levels, respectively, then the sum of nuclear spins, N , and n are [1-3].

$$N = N_- + N_+ \quad \text{Eq 2.7}$$

$$n = N_+ - N_- \quad \text{Eq 2.8}$$

The population of each energy level according to Boltzmann statistics is [1]

$$N_j = \frac{N}{Q} e^{-E_j/kT} \quad \text{Eq 2.9}$$

$$Q = \sum_{j=1}^M e^{-E_j/kT} = e^{\frac{\gamma\hbar B_0}{2kT}} + e^{-\frac{\gamma\hbar B_0}{2kT}} \quad \text{Eq 2.10}$$

Most of the experiments performed in this work were done at room temperature, so consider an experiment at room temperature and a magnetic field of 7 tesla. The energies are [1-3]

$$E_- = \frac{\gamma\hbar B_0}{2} = \frac{(2.675 \times 10^8)(1.054 \times 10^{-34})7}{2} = 9.87 \times 10^{-26} \text{ J} \quad \text{Eq 2.11}$$

$$E_+ = \frac{-\gamma\hbar B_0}{2} = \frac{-(2.675 \times 10^8)(1.054 \times 10^{-34})7}{2} = -9.87 \times 10^{-26} \text{ J} \quad \text{Eq 2.12}$$

At 300 K, the kT energy is

$$kT \cong 1.38 \times 10^{-23} \cdot 300k = 4.14 \times 10^{-21}J \quad \text{Eq 2.13}$$

and

$$\left| \frac{E_{+,-}}{kT} \right| = \frac{9.87 \times 10^{-26}}{4.14 \times 10^{-21}} = 2.38 \times 10^{-5} \ll 1 \quad \text{Eq 2.14}$$

Using the approximation

$$e^x \cong (1 + x) \quad \text{when } x \ll 1 \quad \text{Eq 2.15}$$

then

$$e^{-E_{+}/kT} = e^{\frac{\gamma \hbar B_0}{2kT}} \cong 1 + \frac{\gamma \hbar B_0}{2kT} \quad \text{Eq 2.16}$$

$$e^{-E_{-}/kT} = e^{\frac{-\gamma \hbar B_0}{2kT}} \cong 1 - \frac{\gamma \hbar B_0}{2kT} \quad \text{Eq 2.17}$$

and $Q = 2$. The ratio of spin populations, using these numbers, is

$$\frac{N_{-}}{N_{+}} = 0.99995240 \quad \text{Eq 2.18}$$

Hence, only approximately 24 nuclear spins out of one million spins contribute to the net nuclear magnetization, and this illustrates why NMR is an insensitive technique at room temperature and modest magnetic field strengths.

The population difference in the high-temperature limit is

$$n = \frac{N \gamma \hbar B_0}{Q kT} \quad \text{Eq 2.19}$$

Each individual spin has a magnetic moment proportional to the gyromagnetic ratio of the atom

$$|\mu| = \frac{1}{2} \gamma \hbar \quad \text{Eq 2.20}$$

The macroscopic nuclear magnetization at equilibrium is the sum of the Z-components of the nuclear magnetic moments of the spins along the Z axis.

$$\bar{M} = \sum \vec{\mu}_z \quad \text{Eq 2.21}$$

The net magnetization along the z axis is proportional to the spin population difference because spins aligned opposite to each other cancel out, and the net nuclear magnetization is

$$M_z = \frac{\gamma \hbar n}{2} = \frac{(\gamma \hbar)^2 B_0}{Qk T} \quad \text{Eq 2.22}$$

$$M_z = N \frac{(\gamma \hbar)^2 B_0}{16\pi^2 k T} \quad \text{Eq 2.23}$$

Equation 2.23 shows that under the same magnetic field and temperature conditions, the only non-constant terms that influence the magnitude of the magnetization are the number of spins N and the gyromagnetic ratio γ .

For the same number of spins of ^1H and ^{13}C , the ratio of their equilibrium magnetizations is proportional to the ratio of their gyromagnetic ratios squared. The gyromagnetic ratios are $\gamma_{^1\text{H}} = 267.5 \times 10^6 \frac{\text{rad}}{\text{s}\cdot\text{T}}$ and $\gamma_{^{13}\text{C}} = 67.3 \times 10^6 \frac{\text{rad}}{\text{s}\cdot\text{T}}$, so the ratio of nuclear magnetizations is

$$\frac{M_{^1\text{H}}}{M_{^{13}\text{C}}} = \frac{\gamma_{^1\text{H}}^2}{\gamma_{^{13}\text{C}}^2} \approx 4^2 = 16 \quad \text{Eq 2.24}$$

While the number of carbons and the number of hydrogens in an organic solid are not greatly different, their NMR active isotopes are. The natural abundance of ^1H is 99.98 %, and the natural abundance of the NMR-active isotope of carbon, ^{13}C , is 1.1 %. Hence, the nuclear magnetization of ^1H is further multiplied by approximately 100, and the ^1H nuclear magnetization is nearly 1600 times the ^{13}C nuclear magnetization as shown

$$\frac{M_{1H}}{M_{13C}} = \frac{N_{1H}}{N_{13C}} \frac{\gamma_{1H}^2}{\gamma_{13C}^2} \cong \frac{100}{1} 4^2 = 1,600 \quad \text{Eq 2.25}$$

Such a large difference in magnetization between ^1H and ^{13}C illustrates why ^1H NMR is popular in solution NMR. However, our goal is to observe ^{13}C in the solid state because a) ^1H NMR is surprisingly difficult in solid-state NMR and b) the ^{13}C chemical shift range is large.

Accordingly, it is necessary to find a way to enhance the ^{13}C nuclear magnetization for detection.

2.3 Spin Temperature

The primary variables available to control the strength of nuclear magnetization in a given spin system are the Zeeman field intensity, B_0 , and the absolute temperature of the sample, T . Increasing the ratio of magnetic field to temperature increases the magnetization.

As is illustrated in Figure 2.2, if the magnitude of the Zeeman field is kept constant and the temperature is increased, the resulting magnetization decreases with the increasing temperature.

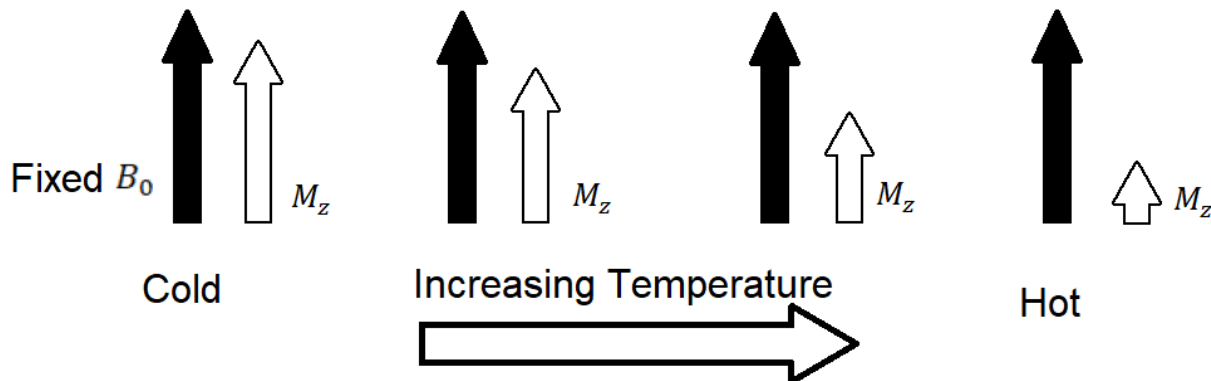


Figure 2.2 Static Magnetic field, increasing temperature yields a decrease in magnetization.

Now consider a system where the magnetization is kept fixed, but the magnetic field is lowered. What is the temperature of such a hypothetical situation? Letting the temperature be defined as $T \propto B_0/M$, this is Curie's law, then decrease in the magnitude of the magnetic field with fixed magnetization would appear to the observer as lowering the temperature of the sample.

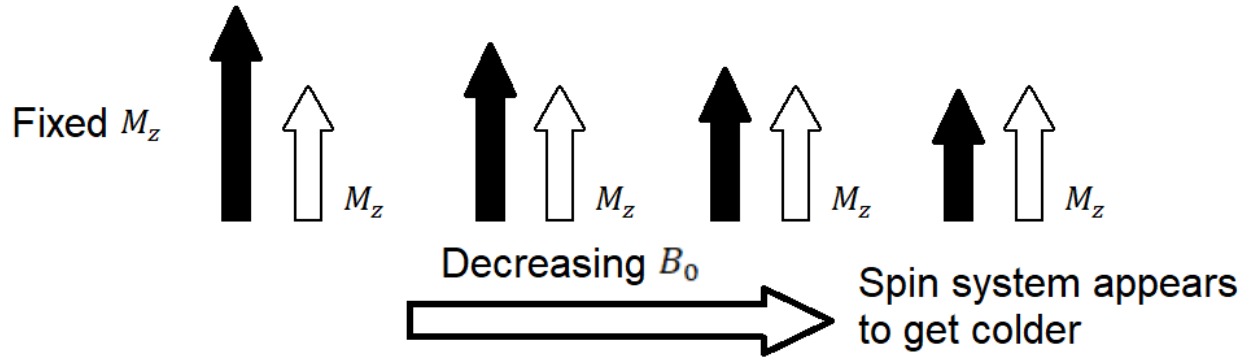


Figure 2.3 Fixed Magnetization with decreasing Zeeman field, the spin system appears to get colder.

Consider a spin system with a ratio of spins in the N^- and N^+ states such as the following.

$$\bar{B}_0 \uparrow \left. \begin{array}{l} m = -1/2 \quad \underbrace{\downarrow\downarrow\downarrow\downarrow}_{N^-} \\ m = +1/2 \quad \underbrace{\uparrow\uparrow\uparrow\uparrow\uparrow\uparrow}_{N^+} \end{array} \right\} \Delta E = \gamma \hbar B_0 \quad \text{Eq 2.26}$$

At equilibrium more spins are aligned parallel to the field orientation rather than anti-parallel. This results in a larger population of spins occupying the N^+ state than the N^- state. This ratio of spin populations is related to the absolute temperature through the Boltzmann distribution.

A sample initially outside the magnetic field will have no net magnetization. When the sample is initially placed in a magnetic field the two energy levels are equally populated, but a nuclear magnetization builds up over time until it reaches its equilibrium value. The process of magnetization requires a net transfer of the spins from the antiparallel orientation high energy state to the parallel orientation low energy state. The transition from the high energy state to the low energy state involves an energy transfer to the lattice. The size of the spin population difference, and consequently net magnetization generated must depend on the ability of that

lattice to accept heat energy. Because heat energy flows from higher temperature to lower temperature, once the lattice and the spin system have reached the same temperature there will be no more net heat transfer, and the nuclear magnetization of the sample will stop increasing.

The temperature of the spin system, or spin-temperature T_{spin} , can be defined through the population ratio [1-3]

$$\frac{N^-}{N^+} = \frac{e^{-E_-/kT}}{e^{-E_+/kT}} = \frac{e^{-\frac{\gamma\hbar B_0}{2kT}}}{e^{\frac{\gamma\hbar B_0}{2kT}}} = e^{-\frac{\gamma\hbar B_0}{kT}} \quad \text{Eq 2.27}$$

$$\Delta E = E_- - E_+ = \frac{1}{2}\gamma\hbar B_0 - \left(-\frac{1}{2}\gamma\hbar B_0\right) = \gamma\hbar B_0 \quad \text{Eq 2.28}$$

$$\frac{N^-}{N^+} = e^{-\Delta E/kT} \quad \text{Eq 2.29}$$

$$\frac{-\Delta E}{kT} = \ln \frac{N^-}{N^+} \quad \text{Eq 2.30}$$

$$T_{spin} = \left(\frac{\Delta E}{k}\right) / \left(\ln \frac{N^+}{N^-}\right) \quad \text{Eq 2.31}$$

Changing the ratio $\frac{N^+}{N^-}$ has a direct effect on the spin temperature T_{spin} . Moreover, the spin-temperature is no longer restricted to positive values.

Consider the following non-equilibrium spin population configurations with fixed magnetic field.

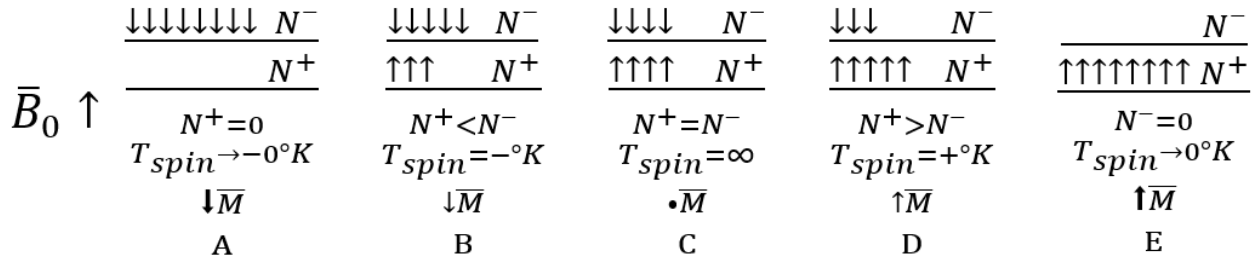


Figure 2.4 an arrangement of non-equilibrium spin populations in a fixed magnetic field at temperatures of $-0^\circ K$ (A), a finite negative temperature (B), infinite temperature (C), a positive temperature (D), and absolute zero (E).

Starting in the middle (Figure 2.4C), if the spin populations are equal, $N^+ = N^-$, then $T_{spin} = \infty$ and there is no net magnetization. Figure 2.4D shows $N_+ > N_-$, which corresponds to a finite, positive spin-temperature with a magnetization parallel to the magnetic field. Figure 2.4E shows all nuclear spins in the lower energy level, which corresponds to a spin-temperature of 0 K. Figure 2.4B shows $N_+ < N_-$, which gives a magnetization anti-parallel to the magnetic field and, according to Equation 2.31, a finite, negative spin-temperature ($T_{spin} < 0$). Finally, Figure 2.4A shows all spins in the upper energy level, and this configuration gives a large anti-parallel magnetization and a spin-temperature approaching zero from the negative side. Note that the spin-temperature moves from hot to cold going from left to right in Figure 2.4; stated differently, negative temperatures are hotter than positive temperatures.

2.4 Cross Polarization: A Thermodynamic View

It was shown that for an organic sample material containing both ^1H and ^{13}C nuclei that the ^1H magnetization is much greater than the ^{13}C magnetization. Techniques to transfer some of the magnetization from the ^1H spin system to the ^{13}C spin system would allow for a greater signal to be built up in the ^{13}C system and make ^{13}C -observe NMR more practical. Cross polarization is a method to transfer magnetization from the ^1H spin system to the ^{13}C spin system [5,6].

To begin the process of cross polarization, the ^1H and ^{13}C spin systems come to thermal equilibrium in the presence of the Zeeman field, \vec{B}_0 , and with the lattice at temperature $T_{Lattice}$ (in actuality, it is not necessary for the ^{13}C spin system to come to equilibrium). The lattice temperature is typically room temperature for our applications. At time $t=0$, the magnetizations are

$$M_0^H = \frac{C_H B_0}{T_{Lattice}} \quad \text{Eq 2.32}$$

$$M_0^C = \frac{C_C B_0}{T_{Lattice}} \quad \text{Eq 2.33}$$

$$C_j = N_j \frac{(\gamma_j h)^2}{16\pi^2 k} \quad \text{Eq 2.34}$$

where $N_c \ll N_h$. Now apply a new magnetic field along the x direction for each of the two spin systems, $\vec{B}_{1,H}$ for ^1H and $\vec{B}_{1,C}$ for ^{13}C , and let the ^1H magnetization that had built up parallel to the Zeeman field now be aligned along its B_1 magnetic field. The ^{13}C magnetization is not aligned along its B_1 magnetic field. The B_1 magnetic fields are much weaker than the Zeeman magnetic field strength. Furthermore, the condition on the relative field strengths is set to

$\frac{B_{1,C}}{B_{1,H}} = \frac{\gamma_H}{\gamma_C}$. The details of how all this is done will be described later. Immediately after the spin

alignments along the respective B_1 magnetic fields, the magnetizations aligned along the respective B_1 fields are

$$M^H = M_o^H = \frac{C_H B_{1,H}}{T'} \quad \text{Eq 2.35}$$

and

$$M^C = \frac{C_C B_{1,C}}{T''} \quad \text{with } T'' \rightarrow \infty \quad \text{Eq 2.36}$$

At this point, the proton spin-temperature T' , appears to be very cold as is indicated in equation 2.37 and the ^{13}C spin temperature T'' is infinite. Using typical experimental parameters, the proton spin temperature is approximately

$$T' = \frac{C_H B_{1,H}}{M_o^H} = \frac{B_{1,H}}{B_o} T_{Lattice} \approx \frac{50 \text{ Gauss}}{300000 \text{ Gauss}} (300 \text{ K}) = 0.05 \text{ K} \quad \text{Eq 2.37}$$

By bringing the very cold ^1H spin system into thermal contact with the very hot ^{13}C spin system, a heat exchange can occur between the two resulting in cooling of the hot ^{13}C spin system. The ^{13}C spin temperature begins to cool and approaches T' , which changes little because the ^1H spin system is very large relative to the ^{13}C spin system. Waiting for a new equilibrium for the ^{13}C magnetization results in

$$M^C = \frac{C_C B_{1,C}}{T'} \quad \text{Eq 2.38}$$

and substituting for T' results in from equations 2.37 and 2.33 leads to

$$M^C = \frac{\gamma_H}{\gamma_C} M_o^C \quad \text{Eq 2.39}$$

Cross polarization, the exchange of energy between the ^1H and ^{13}C spin systems because of the extreme differences between their respective spin temperatures, leads to an approximately four-fold enhancement of the ^{13}C magnetization over what could be obtained by simple magnetization in the Zeeman field.

2.5 Spin Dynamics in the Rotating Frame

The nuclear magnetic moment $\vec{\mu}$ and intrinsic angular momentum \vec{J} are related via [1-3]

$$\vec{\mu} = \gamma \vec{J} \quad \text{Eq 2.40}$$

A magnetic moment placed in a magnetic field \vec{B} experiences a torque, $\vec{\tau}$, equal to

$$\vec{\tau} = \vec{\mu} \times \vec{B} \quad \text{Eq 2.41}$$

and the relationship between angular momentum and torque is

$$\vec{\tau} = \frac{d\vec{J}}{dt} \quad \text{Eq 2.42}$$

Taking the derivative of equation 2.40 gives

$$\frac{d\vec{\mu}}{dt} = \vec{\mu} \times (\gamma \vec{B}) \quad \text{Eq 2.43}$$

The product $\gamma \vec{B}$ has units of angular frequency. The motion of $\vec{\mu}$ is a precession about \vec{B} . It is worthwhile to examine the motion of $\vec{\mu}$ in a rotating coordinate system.

Consider a coordinate system defined by the orthogonal unit vectors \hat{x} , \hat{y} , and \hat{z} and a function $\vec{F}(t) = F_x(t)\hat{x} + F_y(t)\hat{y} + F_z(t)\hat{z}$. At best, the unit vectors can rotate (their length is fixed). Let the coordinate system rotate with angular velocity $\vec{\Omega}$, then the time derivative of \vec{F} is

$$\frac{d\vec{F}}{dt} = \frac{\delta \vec{F}}{\delta t} + \vec{\Omega} \times \vec{F} \quad \text{Eq 2.44}$$

The $\frac{\delta \vec{F}}{\delta t}$ term represents the time rate of change in the \hat{x} , \hat{y} , \hat{z} coordinate system; that is,

$$\frac{\delta \vec{F}}{\delta t} = \hat{x} \frac{dF_x}{dt} + \hat{y} \frac{dF_y}{dt} + \hat{z} \frac{dF_z}{dt} \quad \text{Eq 2.45}$$

Combining equation 2.44 for $\vec{\mu}$ and 2.43 gives

$$\frac{d\vec{\mu}}{dt} = \frac{\delta\vec{\mu}}{\delta t} + \vec{\Omega} \times \vec{\mu} = \vec{\mu} \times (\gamma\vec{B}) \quad \text{Eq 2.46}$$

Hence, the equation of motion of the magnetic moment in the rotating coordinate system is

$$\frac{\delta\vec{\mu}}{\delta t} = \vec{\mu} \times (\gamma\vec{B} + \vec{\Omega}) \quad \text{Eq 2.47}$$

The equation of motion of the magnetic moment in the rotating coordinate system is the same as before provided the magnetic field is replaced by an effective magnetic field $\vec{B}_{eff} = \vec{B} + \frac{1}{\gamma}\vec{\Omega}$.

Returning to the specific case of $\vec{B} = B_o\hat{z}$ and choosing $\vec{\Omega} = -\gamma\vec{B}_o$, then $\frac{\delta\vec{\mu}}{\delta t} = 0$. Hence, the magnetic moment appears static in the rotating frame. But the rotating frame is rotating about the z axis. Hence, the magnetic moment is precessing about the Zeeman field \vec{B}_o .

Equation 2.46 is general and can be used to show how to place the net nuclear magnetization, \vec{M} , which is initially aligned along \vec{B}_o , in different orientations. For example, suppose it is desirable to place $\vec{M} = M_o\hat{z}$ along the y-axis in the rotating frame. This can be done by adding an additional time-dependent magnetic field, $\vec{B}_{1,x}$ that rotates with frequency ω_1 . In the rotating frame, the B_1 magnetic field appears to be static. Equation 2.47 gives

$$\frac{\delta\vec{M}}{\delta t} = \vec{M} \times (\gamma B_o\hat{z} + \gamma B_{1,x}\hat{x} + \vec{\Omega}) \quad \text{Eq 2.48}$$

Choosing $\vec{\Omega} = -\gamma\vec{B}_o$, then

$$\frac{\delta\vec{M}}{\delta t} = \vec{M} \times (\gamma B_{1,x}\hat{x}) \quad \text{Eq 2.49}$$

which describes a rotation about the x axis. If the B_1 field is applied for a time $t_{90} = \frac{(\pi/2)}{\gamma B_{1,x}}$ and then turned off, the magnetization will be aligned along the y axis in the rotating coordinate system and will precess about the Zeeman field.

2.6 The Cross Polarization Experiment

Spin, or magnetization, manipulation in the rotating frame can be used to describe the cross-polarization experiment. Figure 2.5 is the ^1H and ^{13}C cross polarization experiment as described below.

During time period A the proton and carbon spins relax to thermal equilibrium with the Zeeman field B_0 at room temperature. During time period B a $90^\circ \pi/2$ pulse is used to rotate the proton magnetization M_0^H about the X axis to align with the Y axis. In time period C the spin lock of the proton magnetization M_0^H along $B_{1,y}^H$ is applied to the proton magnetization, which causes the apparent temperature of the protons to drop significantly. Also during this time the ^{13}C magnetization $B_{1,y}^C$ is turned on; initially the temperature of the ^{13}C spins appear to be infinite. In order to make thermal contact between the very cold ^1H spins and the very hot ^{13}C spins the Hartmann-Hahn condition must be satisfied, wherein the energy gap in the rotating frame must be frequency matched such that $\gamma_H B_1^H = \gamma_C B_1^C$. This causes the energy splitting of the ^1H spins and the ^{13}C spins to be matched as well. Upon achieving thermal contact the cold proton reservoir begins to cool the hot carbon reservoir, and as the carbon reservoir drops in apparent temperature it implies a building of magnetization aligned with $B_{1,y}^C$.

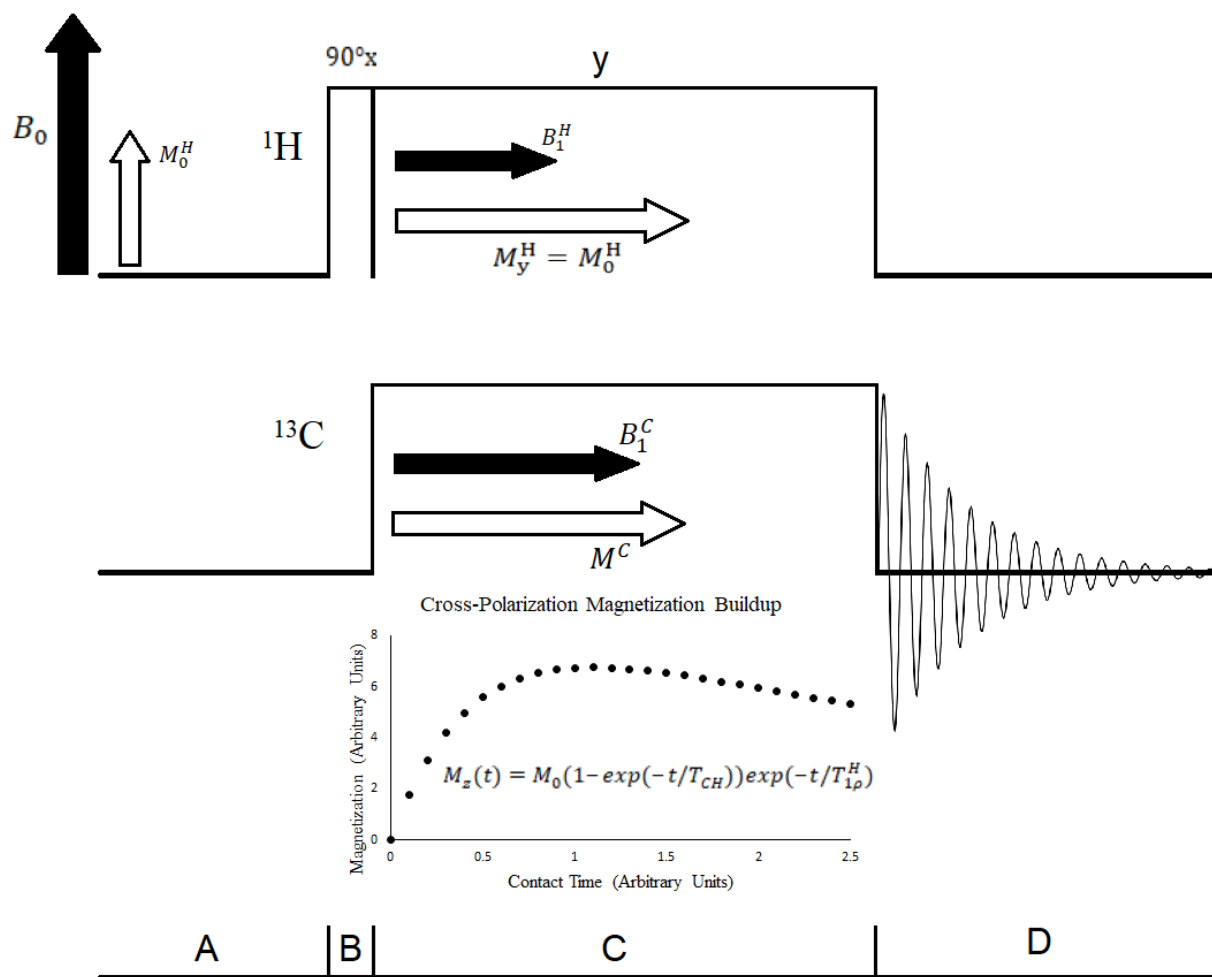


Figure 2.5 CP pulse sequence with an inset graph of cross polarization ^{13}C magnetization buildup

T_{CH} represents the time constant for the building up of ^{13}C magnetization. The value of T_{CH} varies with the strength of the dipolar coupling between ^1H and ^{13}C . This is specific to the environment conditions of a given ^{13}C atom. For example, the T_{CH} value will be different for a carbon in a methyl group than a tertiary carbon with only one bound hydrogen. The $T_{1\rho}^H$ term represents the time constant of the spin lattice relaxation rate of ^1H . Because ^1H are the source of the spin magnetization, the rate at which that magnetization decays will put an upper bound on how long cross polarization contact time may occur before the signal disappears. Typically, the

values of T_{CH} and $T_{1\rho}^H$ are such that $T_{1\rho}^H$ is significantly greater than T_{CH} and the loss of signal due to spin lattice relaxation before sufficient cross polarization magnetization transfer has occurred is not an issue. In the graph in figure 2.5 the effect was exaggerated for illustrative purposes.

Cross polarization requires a mechanism to bring the two spin systems into contact. That mechanism is the heteronuclear dipolar interaction. Consider a system of I spins and S spins with on-resonance B_1 fields for the two systems applied along their respective x axis. The rotating-frame Hamiltonian (in frequency units) is

$$\mathcal{H} = 2D\hat{I}_z\hat{S}_z + \omega_{1,I}\hat{I}_x + \omega_{1,S}\hat{S}_x \quad \text{Eq 2.50}$$

where D is the heteronuclear dipole-dipole coupling and $\omega_{1,I} = \gamma_I B_{1,I}$ and $\omega_{1,S} = \gamma_S B_{1,S}$. The eigenstates and energy eigenvalues are not obvious in this frame of reference since the terms do not commute. However, a transformation of axes obtained by a 90° rotation about the respective y axes and invoking the Hartmann-Hahn condition, $\omega_{1,I} = \omega_{1,S} \equiv \omega_{HH}$ with the condition $\omega_{HH} \gg D$ gives the transformed Hamiltonian

$$\mathcal{H}' = 2D\hat{I}_x\hat{S}_x + \omega_{1,I}\hat{I}_z + \omega_{1,S}\hat{S}_z \quad \text{Eq 2.51}$$

The first term can be rewritten using raising and lowering operators ($\hat{I}_\pm = \hat{I}_x \pm i\hat{I}_y$) to give

$$\mathcal{H}' = \omega_{HH}(\hat{I}_z + \hat{S}_z) + 2D(\hat{I}_+\hat{S}_- + \hat{I}_-\hat{S}_+) \quad \text{Eq 2.52}$$

This transformation shows why cross polarization works. The second term is made of flip-flop terms that have the effect of interchanging states $|\alpha\beta\rangle$ and $|\beta\alpha\rangle$. In other words, the flip-flop term allows energy transfers to occur between the two spin systems and interconverting I and S magnetization while the B_1 fields are applied with the Hartmann-Hahn condition.

2.7 Dynamic Nuclear Polarization, the Overhauser Effect

Another way to enhance NMR signals is through dynamic nuclear polarization (DNP) of ^1H nuclei by a system of unpaired electrons. The magnetogyric ratio of the electron, γ_e , is 658 times greater than the magnetogyric ratio of the proton. Here is described the Overhauser effect which can provide an enormous enhancement of NMR signals. Consider a system consisting of spin-1/2 nuclear spins and unpaired electrons, and for simplicity let the electrons and the nuclei interact through the scalar coupling. Keeping only diagonal terms, the Hamiltonian is

$$\mathcal{H} = \gamma_e \hbar B_o \hat{S}_z + A \hat{I}_z \hat{S}_z - \gamma_n \hbar B_o \hat{I}_z \quad \text{Eq 2.53}$$

The eigenstates are represented as $|++\rangle, | - +\rangle, | + -\rangle$, and $| - -\rangle$, where the first element (+ or -) represents the electron spin state and the second element represents the nuclear spin state.

Figure 2.5 shows the energy diagram for the electron-nuclear spin system having energies E_1, E_2, E_3 , and E_4 for the respectively labeled spin states. Each state has $N_i = N_{i,\epsilon} + N_{i,\eta}$ spins, where ϵ and η represent the electron and nuclear spins. Accordingly, the probability of occupation of state $|\epsilon\eta\rangle$ is

$$p_j = \frac{N_j}{N_1 + N_2 + N_3 + N_4} \quad \text{Eq 2.54}$$

and

$$\sum_{j=1}^4 p_j = 1 \quad \text{Eq 2.55}$$

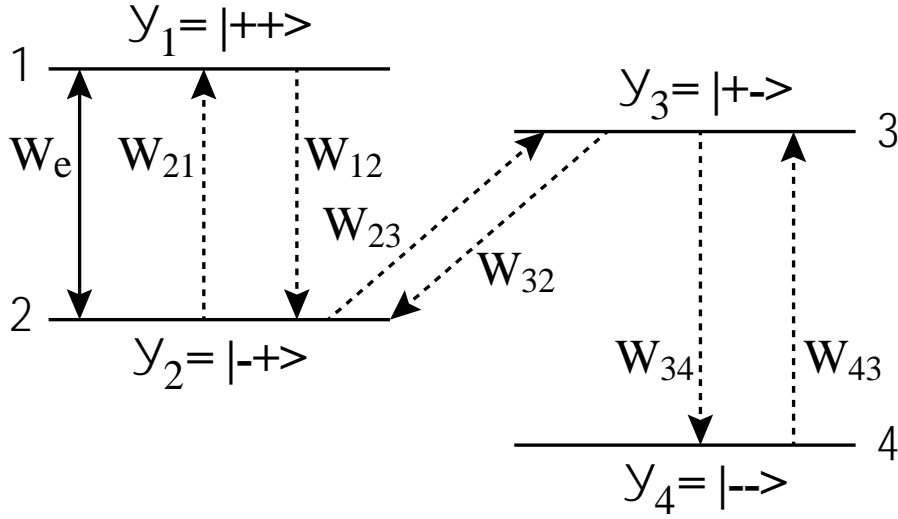


Figure 2.6 Energy diagram for an electron-nuclear spin system.

Now consider an experiment where an applied B_1 field is applied to the electrons with energy that matches the energy spacing between states 1 and 2. The applied B_1 field will cause transitions between states 1 and 2 at a rate W_e . The rates W_{12} , W_{21} , W_{34} , and W_{43} are rates describing electron spin relaxation. The rates W_{23} and W_{32} are rates describing electron-nuclear spin flips, which come about from the scalar interaction in this model.

The rates of change of the probabilities of occupation are

$$\frac{dp_1}{dt} = W_{21}p_2 - W_{12}p_1 + W_e(p_2 - p_1) \quad \text{Eq 2.56}$$

$$\frac{dp_2}{dt} = W_{12}p_1 - W_{21}p_2 + W_e(p_1 - p_2) + W_{32}p_3 - W_{23}p_2 \quad \text{Eq 2.57}$$

$$\frac{dp_3}{dt} = W_{23}p_2 + W_{43}p_4 - W_{32}p_3 - W_{34}p_3 \quad \text{Eq 2.58}$$

$$\frac{dp_4}{dt} = W_{34}p_3 - W_{43}p_4 \quad \text{Eq 2.59}$$

Applying strong irradiation of the electron transition ($W_e \rightarrow \infty$) and waiting for steady-state conditions ($\frac{dp_j}{dt} = 0$) gives the following results. Equation 2.56 gives

$$p_1 = p_2 \quad \text{Eq 2.60}$$

Equation 2.59 gives

$$p_3 = \frac{W_{43}}{W_{34}} p_4 \quad \text{Eq 2.61}$$

Equation 2.58 gives

$$p_3 = \frac{W_{23}}{W_{32}} p_2 \quad \text{Eq 2.62}$$

Equations 2.61 and 2.62 represent normal thermal equilibrium population ratios between states 3 and 4 and between 3 and 2, respectively. Since states 3 and 4 and states 3 and 2 are in thermal equilibrium, states 2 and 4 are also populated according to thermal equilibrium conditions. Only states 1 and 2 are not in thermal equilibrium because of the strong B_1 field applied to the electrons; in fact, states 1 and 2 are saturated.

For a pair of states in thermal equilibrium, Boltzmann statistics places the condition of populations

$$p_j = p_i e^{(E_i - E_j)/kT} \equiv B_{ij} p_i \quad \text{Eq 2.63}$$

With this notation, the previous equations become

$$p_2 = p_1 \quad \text{Eq 2.64}$$

$$p_3 = B_{43} p_4 \quad \text{Eq 2.65}$$

$$p_3 = B_{23} p_2 \quad \text{Eq 2.66}$$

$$p_4 = B_{24} p_2 \quad \text{Eq 2.67}$$

Using the condition $\sum_{j=1}^4 p_j = 1$, then

$$p_1 = p_2 = \frac{1}{2+B_{23}+B_{24}} \quad \text{Eq 2.68}$$

$$p_3 = \frac{B_{23}}{2+B_{23}+B_{24}} \quad \text{Eq 2.69}$$

$$p_4 = \frac{B_{24}}{2+B_{23}+B_{24}} \quad \text{Eq 2.70}$$

We are ready to calculate the enhancement factor of the nuclear magnetization that is caused by simply irradiating the electrons while experimentally doing nothing to the nuclei.

Calculate the expectation value of $\langle \hat{I}_z \rangle$

$$\langle \hat{I}_z \rangle = \sum p_i \langle i | \hat{I}_z | i \rangle \quad \text{Eq 2.71}$$

which gives

$$\langle \hat{I}_z \rangle = \frac{1}{2} (p_1 + p_2 - p_3 - p_4) \quad \text{Eq 2.72}$$

This leads to

$$\langle \hat{I}_z \rangle = \frac{1}{2} \left(\frac{2 - B_{23} - B_{24}}{2 + B_{23} + B_{24}} \right) \quad \text{Eq 2.73}$$

Invoking the high-temperature approximation and simplifying yields from the definitions of the respective B_{ij} quantities

$$\langle \hat{I}_z \rangle = \frac{1}{2} \left(\frac{(E_3 - E_2) + (E_4 - E_2)}{4kT} \right) \quad \text{Eq 2.74}$$

The energy eigenvalues are obtained from the Hamiltonian acting on states 2, 3, and 4 and give

$$(E_3 - E_2) = \gamma_n \hbar B_o + \gamma_e \hbar B_o \quad \text{Eq 2.75}$$

and

$$(E_4 - E_2) = \gamma_n \hbar B_0 + A/2 \quad \text{Eq 2.76}$$

Hence, with the microwave power applied to the electrons

$$\langle \hat{I}_z \rangle_{on} = \frac{1}{2} \left(\frac{\gamma_e \hbar B_0}{4kT} \right) \quad \text{Eq 2.77}$$

Now compare $\langle \hat{I}_z \rangle_{on}$ with $\langle \hat{I}_z \rangle_{thermal}$, where $\langle \hat{I}_z \rangle_{thermal}$ represents the expectation value with no microwave power applied to the electrons and the system comes to thermal equilibrium ($p_1 \neq p_2$). $\langle \hat{I}_z \rangle_{thermal}$ is

$$\langle \hat{I}_z \rangle_{thermal} = \frac{1}{2} (p_1 + p_2 - p_3 - p_4) \quad \text{Eq 2.78}$$

where

$$p_j = \frac{e^{E_j/kT}}{\sum_{i=1}^4 e^{E_i/kT}} \quad \text{Eq 2.79}$$

Using the high-temperature approximation

$$\langle \hat{I}_z \rangle_{thermal} = \frac{\gamma_n \hbar B_0}{4kT} \quad \text{Eq 2.80}$$

The enhancement of nuclear spin signal is given by $\langle \hat{I}_z \rangle_{on} / \langle \hat{I}_z \rangle_{thermal}$ which is at this point

$$\langle \hat{I}_z \rangle_{on} / \langle \hat{I}_z \rangle_{thermal} = \frac{1}{2} \frac{\gamma_e}{\gamma_n} \quad \text{Eq 2.81}$$

This enhancement was obtained by applying microwave power connecting only the 1 and 2 states. If we simultaneously apply microwave power to the 3 and 4 states, then the nuclear signal enhancement is

$$\langle \hat{I}_z \rangle_{on} / \langle \hat{I}_z \rangle_{thermal} = \frac{\gamma_e}{\gamma_n} \quad \text{Eq 2.82}$$

which is a theoretical enhancement factor of 658.

This model, based on the Overhauser effect, demonstrates how it is possible to achieve a very high polarization, or magnetization, of the ^1H spin system over its normal equilibrium value that occurs just from the Zeeman interaction. Once the ^1H spin system polarization is enhanced by irradiating the electrons, ^1H - ^{13}C cross polarization can be performed to enhance the ^{13}C spin system far greater than possible by cross polarization alone.

2.8 Signal Averaging

While the gain factor of 4 in signal enhancement via cross-polarization in the ^{13}C magnetization is useful, a greater benefit is to take advantage of typically short ^1H spin-lattice relaxation times T_1 compared to typically long spin-lattice relaxation times for ^{13}C . The ^1H T_1 is typically less than a second for macromolecular systems, whereas the ^{13}C T_1 is on the order of tens to hundreds of seconds. This means that many more scans can be taken in the same time using cross polarization to take advantage of the speedy recovery of the ^1H spins. This is advantageous because the signal-to-noise ratio in an NMR experiment is proportional to the square root of the number of acquisitions, n . NMR detects the voltage that the precessing nuclear magnetization induces in an inductor. In addition to the voltage induced by the precessing nuclei, there is also random electrical noise that is detected. The goal is to raise the NMR signal above the noise.

$$\text{signal} \propto n \quad \text{Eq 2.83}$$

$$V_{rms} = \sqrt{\frac{V_1^2 + V_2^2 + V_3^2 + \dots + V_n^2}{n}} \propto \frac{1}{\sqrt{n}} \quad \text{Eq 2.84}$$

$$\frac{\text{Signal}}{\text{noise}} \propto \frac{n}{\sqrt{n}} = \sqrt{n} \quad \text{Eq 2.85}$$

The signal-to-noise ratio improves with taking more scans and averaging them together. However as is shown in equation 2.85 it takes 4 times the number of scans to get an improvement in signal-to-noise ratio of a factor of two. Average improvement in signal-to-noise for ^{13}C from cross polarization helps by a factor of 4, and the greater number of scans that can be taken due to the fast ^1H recycle delay improves the signal-to-noise by a factor of \sqrt{n} .

2.9 Chemical Shift Anisotropy and Magic-Angle Spinning NMR

The ^{13}C NMR spectrum of a solid is typically dominated by the chemical shift anisotropy interaction, which arises from local diamagnetic and paramagnetic electron currents induced in the sample by the applied Zeeman magnetic field. The induced electron currents produce a local magnetic field, ΔB_{CS} , at the site of the nuclear spin. Hence, the total magnetic field at the site of the nuclear spin is

$$B = B_o + \Delta B_{CS} \quad \text{Eq 2.86}$$

and the resonance frequency of the nuclear spin becomes

$$\omega = \gamma(B_o + \Delta B_{CS}) \quad \text{Eq 2.87}$$

The resonance frequency is now shifted by an amount $\gamma\Delta B_{CS}$. Experimentally it is observed that $\Delta B_{CS} \propto B_o$ and that $\Delta B_{CS} \ll B_o$, so the quantity σ is defined such that

$$\Delta B_{CS} = -\sigma B_o \quad \text{Eq 2.88}$$

The quantity σ is the chemical shift, and in solution NMR the resonance frequency is

$$\omega = \gamma B_o (1 - \sigma_{iso}) \quad \text{Eq 2.89}$$

where σ_{iso} is the isotropic chemical shift. A reason why NMR spectroscopy is so powerful is that the isotropic chemical shift depends on the local electronic structure near the nucleus, which differs between chemical groups. For example, the ^{13}C chemical shift of a methyl carbon differs from that of an aliphatic carbon which differs from that a carbonyl carbon and so on. Hence, a ^{13}C NMR solution spectrum of a complex molecule has a multitude of well-resolved resonances, and each resonance can be assigned to a specific carbon species.

Since the electron currents about a nucleus are expected to depend on the orientation of the molecule with respect to the Zeeman field, the full tensorial nature of the chemical shift must be considered for solid-state NMR.

Figure 2.7 depicts two ^{13}C NMR spectra of the carboxylate carbon in a single crystal of L-alanine. The spectra were taken consecutively, the only experimental difference is the crystal orientation relative to the Zeeman field B_0 was changed manually between experiments. The four carboxylate orientations in the crystal unit cell are resolved clearly. In Figure 2.8 the unit cell crystal structure of L-alanine is depicted with the carboxylate carbons labelled as C1 in each molecule. The four distinct orientations of the carboxylate carbon with respect to the unit cell correlate with the four peaks shown in Figure 2.7. As the orientation of the crystal was changed the chemical shift each molecule experienced changed as the orientation of the molecules were altered with respect to the Zeeman field.

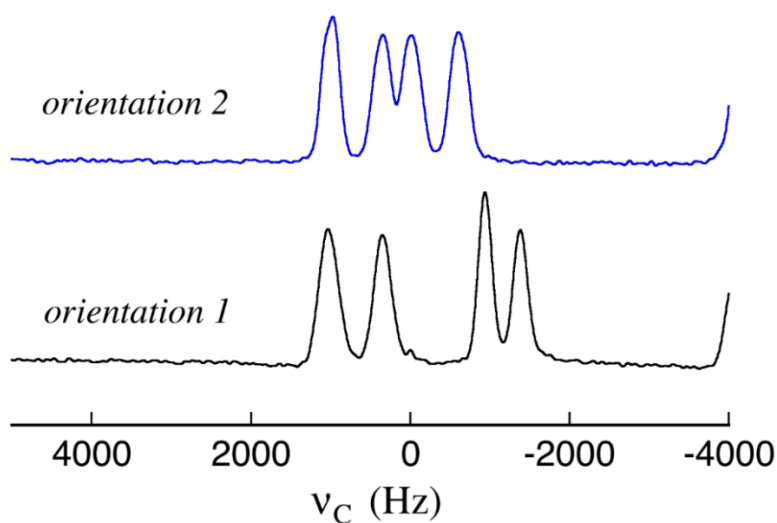


Figure 2.7 Single crystal ^{13}C Solid state NMR spectrum of the carboxylate carbon in alanine. The crystal was scanned in one orientation and then manually rotated by some amount and scanned again. The four alanine orientations in the crystal unit cell can be observed, and their shift upon crystal rotation is apparent.

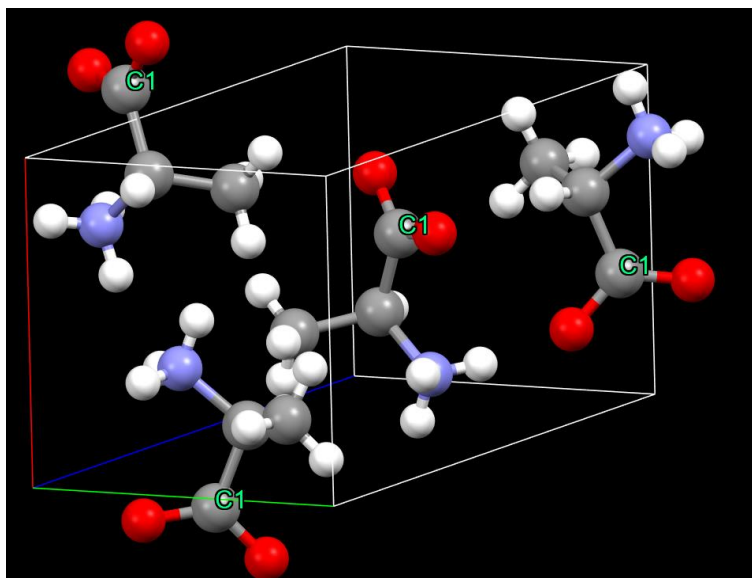


Figure 2.8 The crystal unit cell of L-Alanine. The carboxylate carbons are identified as C1 in each molecule. The four different orientations with respect to the unit cell orientation are apparent.

The chemical shift anisotropy contribution to the shift in resonance frequency is orientation dependent and described by a 3×3 matrix. The contribution to the resonance frequency for a particular isochromat from the chemical shift anisotropy for a static sample is

$$\omega_{cs} = -\gamma B_o (\sigma_{xx} \cos^2 \alpha \sin^2 \beta + \sigma_{yy} \sin^2 \alpha \sin^2 \beta + \sigma_{zz} \cos^2 \beta) \quad \text{Eq 2.90}$$

where σ_{xx} , σ_{yy} , and σ_{zz} are the principal-axis values of the chemical shift tensor. The angles α and β are rotation angles that relate the principal-axis coordinate system of the chemical shift anisotropy tensor to the laboratory frame, where the Zeeman field defines the laboratory frame z-axis. For a powder sample, all angles of α and β must be summed over to determine the overall static-sample powder pattern.

Figure 2.9 is a static sample ^{13}C NMR spectrum of the carboxylate carbon of L-alanine. The powder pattern generated from the experiment is the result of the distribution of molecular

orientations with respect to the Zeeman field. The left side of the spectrum at about 2500 Hz is produced by molecular orientations where the C-C bond is parallel to the Zeeman field. The tall middle portion of the spectrum at 0 Hz comes from molecular orientations where the C-C bond is approximately perpendicular to the Zeeman field, but the C-O bonds are still roughly in the same plane as the Zeeman field. The right side of the spectrum at about 3500 Hz arises from the molecular orientations where the C-C bond is perpendicular to the Zeeman field and the C-O bonds lie in the plane approximately perpendicular to the Zeeman field.

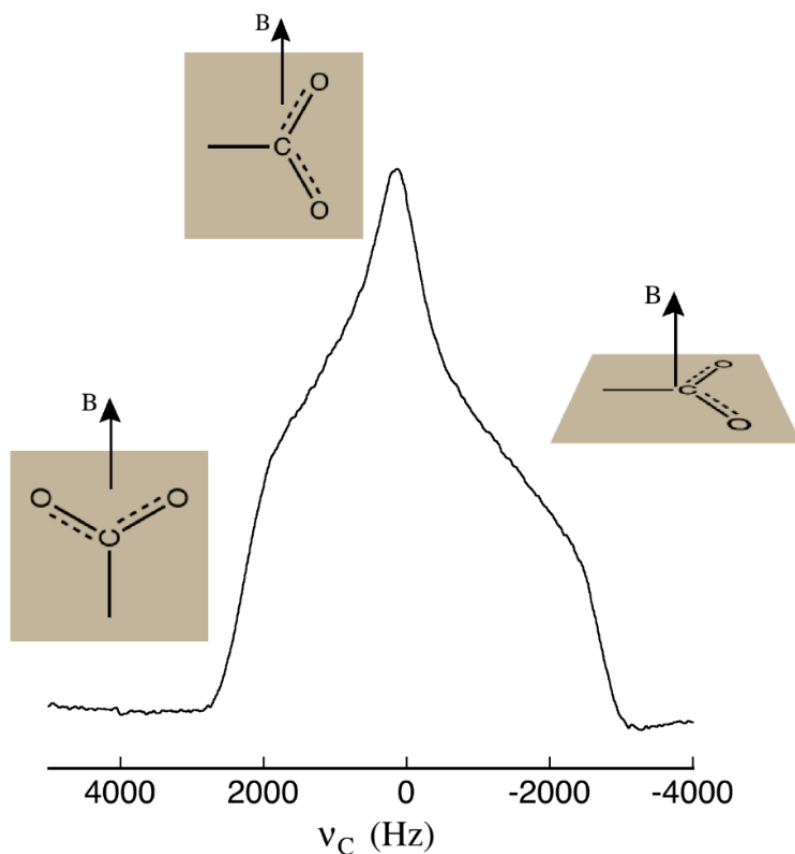


Figure 2.9 The static powder pattern ^{13}C NMR spectra of the carboxylate carbon of L-alanine

As Figure 2.9 shows, the static-sample ^{13}C spectrum of the carboxylate carbon of alanine is broad, approximately 6 kHz on a 151 MHz spectrometer. Hence, a macromolecular system would consist of many overlapping broad powder patterns and would be difficult to analyze. Fortunately, spectral resolution can be achieved by magic-angle sample spinning (MAS). MAS is the physical rotation of the sample at a rate ω_r about an axis that makes an angle $\vartheta = \cos^{-1}(1/\sqrt{3})$ to the Zeeman field (the bore axis of a superconducting magnet). This sample rotation is shown in Figure 2.10. As the sample rotates, the orientation of any given molecule changes continually as the sample rotates with respect to the external Zeeman field and its resonance frequency becomes time dependent. For example, the instantaneous time dependence of the resonance frequency for an axially symmetric chemical shift ($\sigma_{\parallel} = \sigma_{zz}$ and $\sigma_{xx} = \sigma_{yy}$) is

$$\omega_{cs}(t) = \frac{\sigma_{\parallel}}{2} [\sin^2\beta \cos 2(\alpha + \omega_r t) - \sqrt{2} \sin 2\beta \cos(\alpha + \omega_r t)] \quad \text{Eq 2.91}$$

The spinning rate dependence of the instantaneous resonance frequency leads to a spectrum consisting of a centerband and a series of spinning sideband. The centerband occurs at the same isotropic chemical shift that is found for a sample in solution. The spacing between adjacent spinning sidebands are separated by $\omega_r/2\pi$.

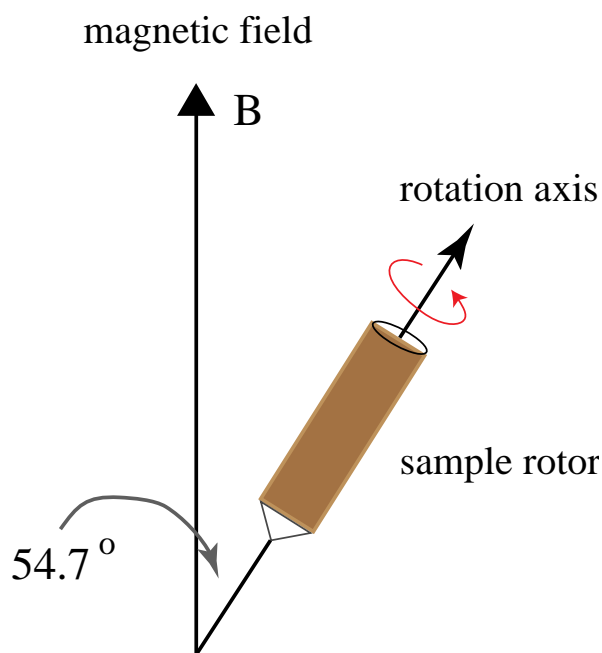


Figure 2.10 A depiction of the sample rotation axis set at the magic angle relative to the Zeeman field.

The rate at which the sample is spun about the magic angle is important. To achieve high resolution in ^{13}C solid state NMR, the spinning speed must be much greater than the frequency of that interaction. This is illustrated in figure 2.11 for a static sample. The top spectrum shows the powder pattern for a static sample. (Take note of the scaling factor placed on the right-hand side.) At a 500 Hz spinning speed the powder pattern becomes a series of peaks in the rough outline of the powder pattern. It is important to point out that the peaks are all spaced 500 Hz apart, which is the rotation rate. These are spinning side bands and appear at integer multiples of the rotation rate. The height above the baseline is also increased as the area is consolidated from the whole broad powder pattern to just the centerband and the spinning sidebands. As the rotation rate increases the number of spinning sidebands decreases, the spacing between the sidebands increases and the peak height of the centerband increases. At 3000 Hz the two remaining spinning sidebands are low intensity and 3000 Hz away from the intense centerband.

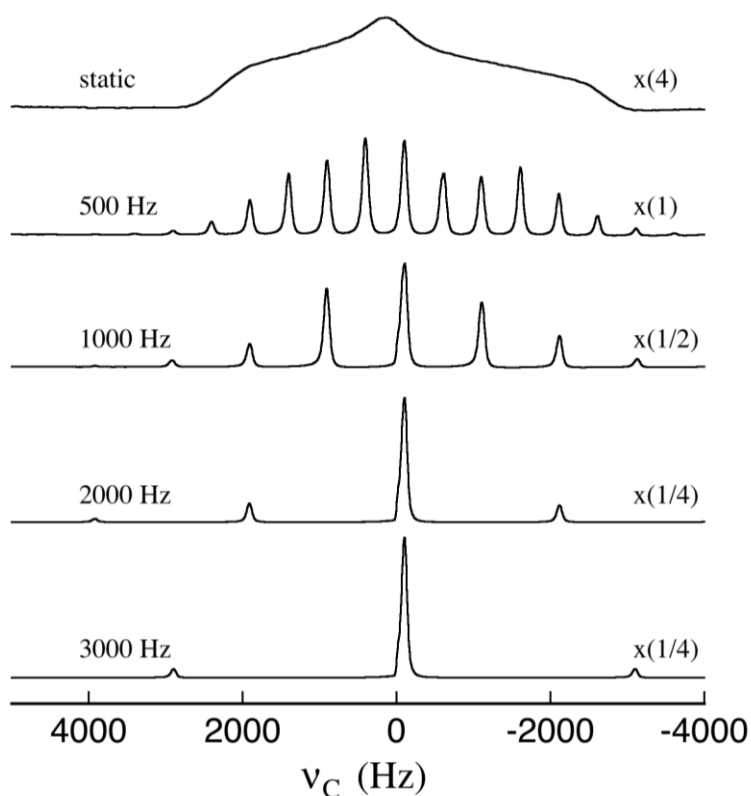


Figure 2.11. ^{13}C spectra of the carboxylate carbon of L-Alanine spun at different spinning rates from static 0 Hz to 3000 Hz.

Figure 2.12 depicts a series of ^{13}C NMR spectra of the carboxylate carbon of L-alanine. The spectra of the sample spun at 3000 Hz is very similar to the spectra of the solution sample. The peak positions of the solution and spinning graph are identical, but the peak width in the solid spin sample is wider than the peak in the solution sample. When compared to the powder pattern of the static sample, it is obvious how invaluable a tool magic angle spinning is in generating solution-like spectra.

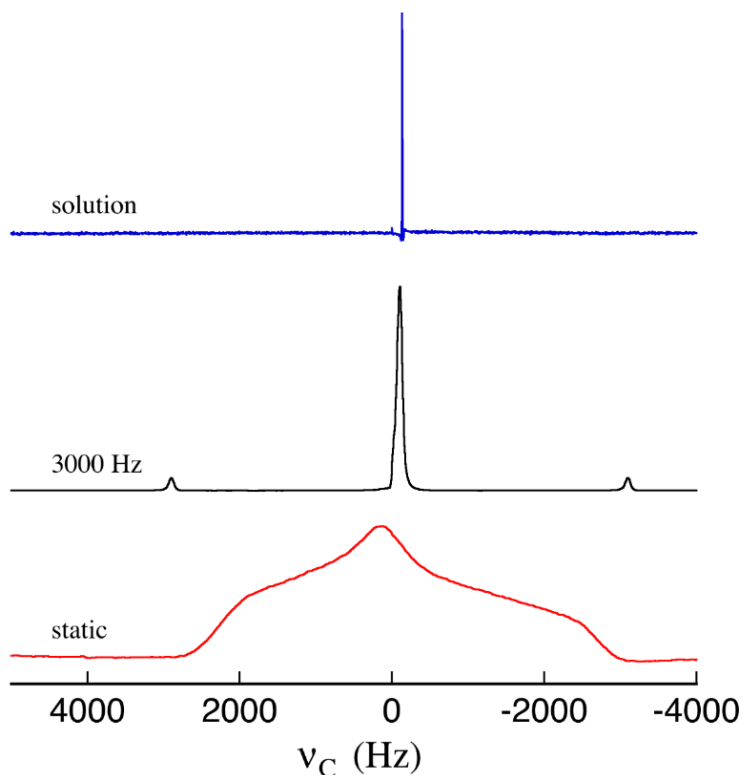


Figure 2.12 ^{13}C NMR spectra of the carboxylate carbon of L-alanine in solution, solid with a spinning rate of 3000 Hz, and a static sample.

Figure 2.13 illustrates the resolution achieved by MAS NMR. The ^{13}C MAS NMR spectrum of $[\text{Cs}(\text{p-tert-butylcalix}[4]\text{arene-H})(\text{MeCN})]$ is shown. This is a complex molecular system with nine distinct carbon sites. All the ^{13}C resonances associated with each carbon site are resolved and assigned, and the spinning rate is sufficient to dramatically reduce the spinning sidebands. This is an example of how MAS can be used to produce high quality liquid-like spectrum in complex molecular systems like those that are found in biological samples.

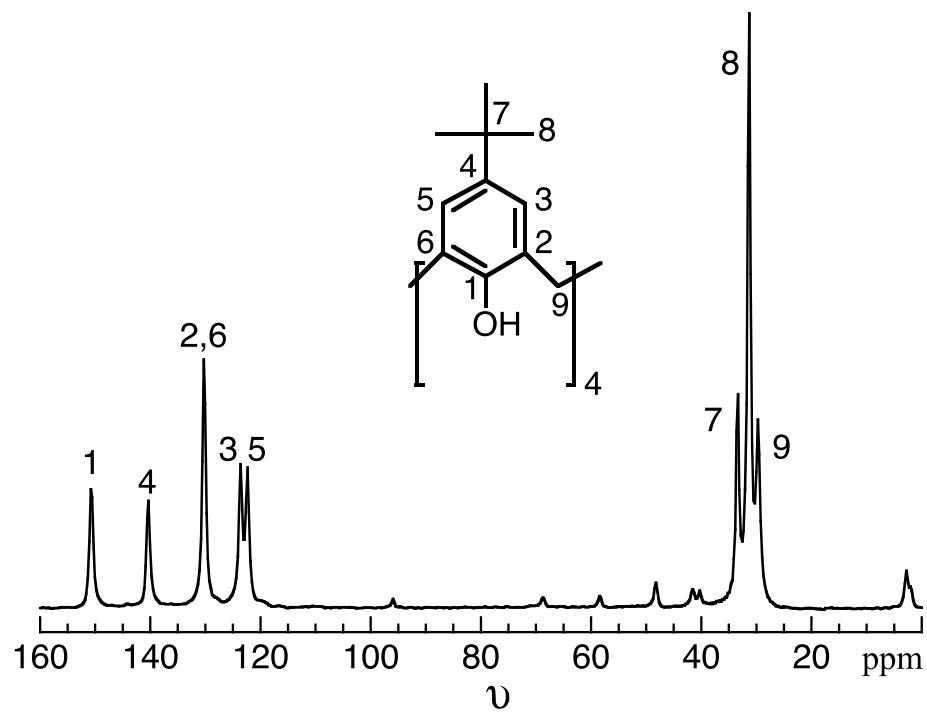


Figure 2.13 ^{13}C MAS NMR spectrum of $[\text{Cs}(p\text{-tert-butylcalix[4]arene-H})(\text{MeCN})]$. Unlabeled resonances are spinning sidebands.

References

1. Slichter, C. P. *Principles of Magnetic Resonance*; Springer: Berlin ; New York, 1996.
2. Schumacher, R. T. *Introduction to Magnetic Resonance*; New York Benjamin, 1970.
3. Kittel, C. *Introduction to Solid State Physics*; Wiley: Hoboken, Nj, 2005.
4. Niinikoski, T. O. *The Physics of Polarized Targets*; Cambridge University Press, 2020.
5. Schaefer, J.; Stejskal, E. O.; Buchdahl, R. High-Resolution Carbon-13 Nuclear Magnetic Resonance Study of Some Solid, Glassy Polymers. *Macromolecules* **1975**, 8 (3), 291–296. <https://doi.org/10.1021/ma60045a010>.
6. Schaefer, J.; Stejskal, E. O. Carbon-13 Nuclear Magnetic Resonance of Polymers Spinning at the Magic Angle. **1976**, 98 (4), 1031–1032. <https://doi.org/10.1021/ja00420a036>.

Chapter 3 Harvesting Insect Wing Membranes

3.1 Cicada

500 specimens of Cicada *Magicicada Cassini* were caught live by hand in Berlin Township, Ohio within the polygon defined by GPS coordinates (40.231714, -82.982771), (40.231861, -82.98285), (40.231669, -82.983785), (40.231546, -82.983694) on June 6-9th 2017.

The forewings of deceased cicadas were separated from their bodies by hand using a rolling pinching motion to tear the wing from the body at the base of the wing and ensuring that the wing structure and membrane remained intact. Figure 3.1 shows the typical cicada forewing. The cicada forewing is composed of a network of veins spread out over the wing area which provide the structural support to the wing. Spanning the gap between the veins are the thin translucent wing membranes which compose the majority of the wings surface area, and are necessary to allow flight.

The forewings were dissected in two steps. First, the leading edge vein (called forevein hereafter) was separated from the rest of the wing. The membrane was removed from the remaining portion of the wing cutting the membrane sections away from the veins with a scalpel. The veins were stored separately. After the membrane sections were cut free of the vein, the center section of the membrane was cut out and separated from the perimeter portion as is shown in Figure 3.2. The center wing membrane and outer wing membrane portions were separated during collection and stored separately as the center wing membrane and the outer wing membrane.

When cutting the wing membranes of each insect, special care was taken to ensure that no vein content remained. As the veins are considerably darker and opaque compared to the nearly transparent membrane, it was a relatively simple, albeit tedious, task to cut away any dark portions and maintain a vein free membrane sample.

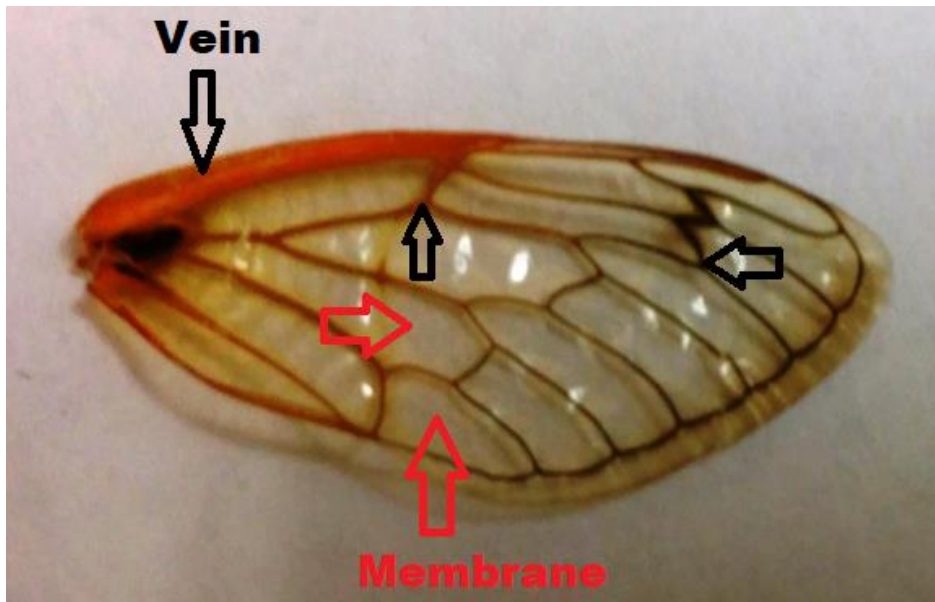


Figure 3.1 An image of a cicada wing, veins are indicated with black arrows and membrane sections are indicated with red arrows.

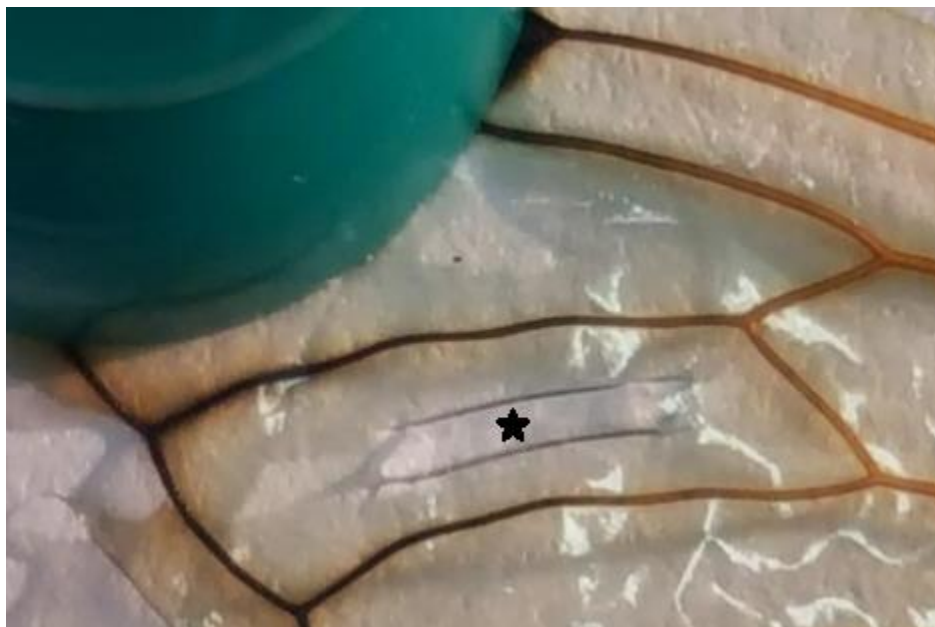


Figure 3.2 A close-up image of a cicada wing held in place for dissection by a thumbtack (top left corner). The center region that was separated is marked with a star.

3.2 Honeybee

Honeybees, *Apis mellifera ligustica*, were purchased from Mountain Sweet Honey (Toccoa, Georgia). The bees were euthanized by freezing. Figure 3.3 shows the forewing of a honeybee.

The forewings were removed and washed vigorously with water for several minutes. The wings were dried under a vacuum. Once dried, the wings were dissected to extract the membrane sections of the wing under magnification. The larger sections of the membrane near the end of the honeybee's forewing were selected for collection since they are easiest to obtain.



Figure 3.3 A honeybee forewing shown with a millimeter scale ruler and scalpel blade for scale.

3.3 Ladybug

Ladybugs, *Hippodamia convergens*, were purchased from Hirt's Garden (Granger Township, Ohio). The insects were euthanized by freezing with liquid nitrogen and the hindwing was carefully unfolded and removed for dissection. Figure 3.4 shows the ladybug hindwing. The membrane samples were cut from the three major sections of the ladybug wing indicated with arrows. Care was taken to ensure that no vein content was collected with the wing membrane samples.



Figure 3.4 A ladybug wing shown with a millimeter scale ruler and scalpel blade for scale.

3.4 Amber Phantom Butterfly

Deceased amber phantom butterflies, *Haetera piera Peru*, were purchased from The Butterfly Company (Chicago, Illinois). A butterfly is shown in Figure 3.5. The forewing of the butterflies was selected for harvesting membrane samples because the forewing lacks chitin plates. The wing membrane sections are large on the amber phantom butterfly, and membrane samples were collected in large strips that were easy to handle.



Figure 3.5 An amber phantom butterfly shown with a millimeter scale ruler for scale.

3.5 Measuring the Thickness of Insect Wing Membranes

A Nikon Eclipse ME600 compound microscope with 10x, 20x, and 50x objective lenses was used to characterize physical aspects of the insect wings. A Pixellink PL-B742U camera was attached to the microscope and connected to a windows computer. All images were taken using PixelINK Capture version 2.0.3.5.

A glass slide with 100-micrometer and 10-micrometer divisions was used to determine the scale at the focal plane to determine the size of objects. Images of the scale through the microscope using the camera gave the pixel-to-micrometer conversion as shown in Figure 3.6. The pixel to micrometer conversions are tabulated in Table 3.1.

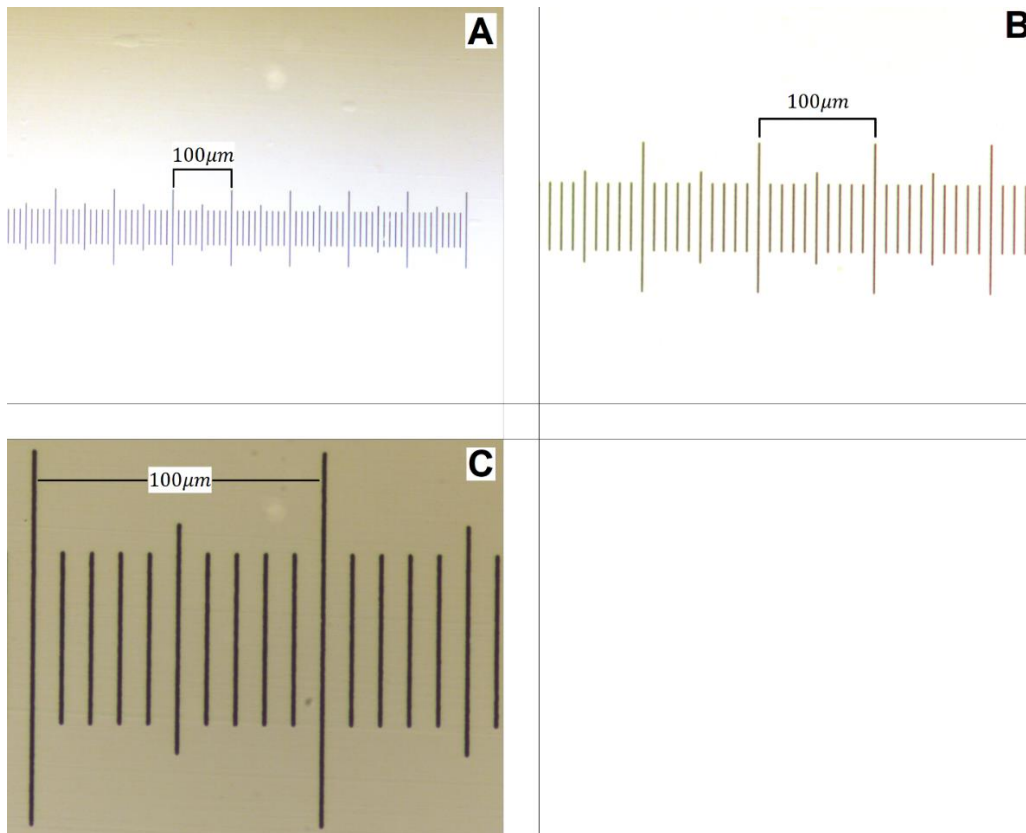


Figure 3.6 The 100-micrometer scale at A) 10x, B) 20x, and C) 50x magnification. These images are all scaled to the same factor so that if you were to observe directly through the microscope, they would appear to be this scale relative to each other.

This scale was tested by comparing wires measured with precision Mitutoyo digital calipers. The diameter of two wires measured with calipers were 110 micrometers and 30 micrometers, respectively. The two wires were examined under the microscope and images are shown in Figure 3.7.

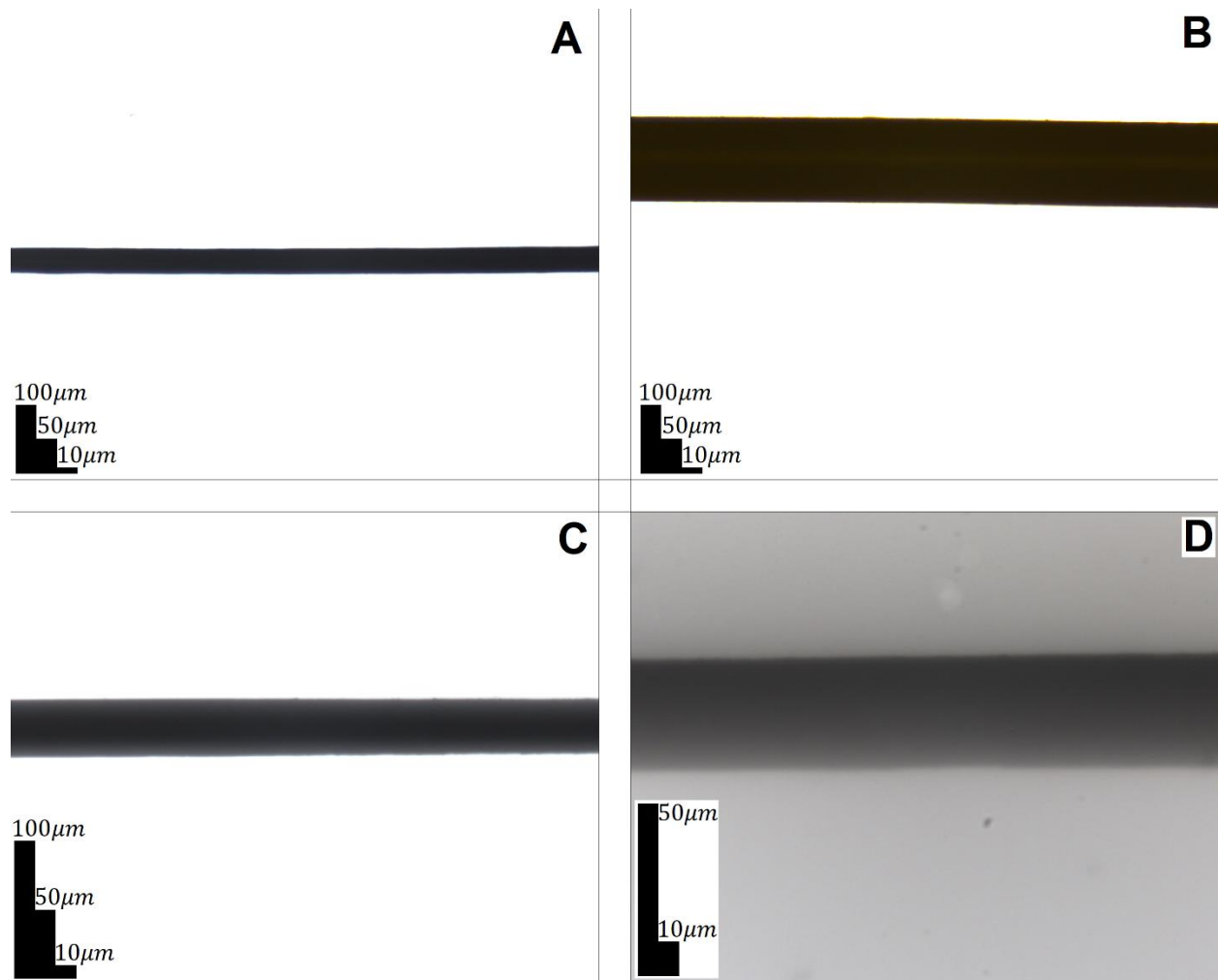


Figure 3.14 Wire viewed under the microscope as scale reference. (A) The 30-micrometer wire imaged using the 10x objective lens. (B) The 110-micrometer wire imaged using the 10x objective lens, (C) the 30-micrometer wire imaged using the 20x objective lens. (D) The 30-micrometer wire imaged using the 50x objective lens. These images are all scaled to the same factor so that if you were to observe directly through the microscope, they would appear to be this scale relative to each other.

The results were consistent with the inspection of the 100-micrometer glass slide.

Magnification level	10 micron distance represented by	1 micron distance represented by
10x	15 pixels	1.5 pixels
20x	30 pixels	3 pixels
50x	75 pixels	7.5 pixels

Table 3.1 Pixel to micron measurements at 10x, 20x, and 50x magnification

Samples of the insect wings were taken and cut into small strips to fit edgewise underneath the microscope 50x objective lens. Ten samples were taken of each insect wing type and the thicknesses were averaged across 10 of each insect and the results are presented in section 4.2.

3.6 Purifying Chitin from Cicada Slough

Cicada sloughs were collected in Knoxville, Tennessee during the seventeen-year 2021 emergence of Brood X. Figure 3.8 shows examples of the slough. The sloughs were stored in the freezer. The procedure for processing the sloughs was based on procedures for extracting natural chitin sources from cicada sloughs and beetle larvae [1-3]. The concentrations and the treatment durations were increased to ensure that the final product was extremely pure chitin, without any remaining lipid, protein, or catechol content remaining. The heads and legs of the cicada sloughs were separated from the bodies of the sloughs and discarded. Only the body (thorax and abdomen) sections were used to obtain chitin. This was done because it is known that several varieties of insects have deposits of minerals, such as zinc or calcium to harden their mandibles and legs to harden them preventing wear [4-8]. We thought that it is entirely reasonable and expected that cicadas, who spend the vast majority of their 13-year lifespan underground tunneling through the soil and piercing the roots of plants to source food, would have such mineralizations in their exoskeletons during that stage of their development. This supposition is shared by Lehnert *et al.* [9] who say “The ovipositor is not the only structure of the cicada that bores into wood; therefore, other structures might be augmented with inorganic elements. The nymphal and adult stages of the cicada feed on xylem, which would involve the mouthparts penetrating into wood. In addition, given the amount of force necessary for the mouthparts and the ovipositor to push through wood, it could be hypothesized that the tarsi, which grip the wood, also are augmented with inorganic elements.” We wanted to avoid the minerals as we were unsure how effective the procedures for isolating pure chitin would be at removing concentrated deposits of minerals should there be any.



Figure 3.8 Image of the cicada sloughs prior to processing.

Approximately 6 grams of the cicada slough bodies were used during each batch of chitin extraction. The cicada slough bodies were thoroughly ground in a Hamilton Beach model 80335R coffee grinder, producing a powder. Grinding was done to increase the surface area of the cicada sloughs and to reduce the spatial volume of the 6 grams of cicada sloughs by eliminating the largely hollow body cavity. The ground powder easily fit inside a standard Buchner funnel for the filtration and washing steps. Working with powder eliminated the possibility of any air pockets persisting inside the body cavities of the cicada sloughs during the treatment and washing steps, increasing the consistency and repeatability of the procedure.

The cicada slough powder was placed into a 1-liter beaker and the beaker was then placed on a hot plate in a fume hood. A thermometer was suspended about an inch from the bottom of the beaker, and a stir bar was added. The beaker was filled with approximately 750ml of 2N HCl and a watch glass was placed on top of the beaker to condense the vapors. The stirred solution was heated for 40 minutes at 100 degrees Celsius. After 40 minutes, the beaker was removed from the hot plate to cool. Once cooled, the solution and powder were transferred into a Buchner funnel for vacuum filtration. Any powder that remained in the beaker was rinsed with

ultrapure water into the filter funnel as well. The powder was rinsed in the Buchner funnel with ultrapure water until a neutral pH was achieved.

The filtered powder was placed in a 500mL three-neck round bottom flask. The round bottom flask was filled halfway with 2N NaOH solution. The flask was placed in a dish of sand on a hot plate in a fume hood, and a stir bar was added to the flask. A condenser was connected to one of the three necks of the flask, a thermometer was inserted in another neck and the third neck was capped off. Aluminum foil was loosely wrapped around the flask and sand dish to help preserve the heat. The hot plate setting was adjusted until the thermometer in the flask read a steady 80°C. The solution was left at 80°C for 72 hours.

After 72 hours of heating the flask was allowed to slowly cool to room temperature by removing the flask from the sand. The solution was filtered again using vacuum filtration in a Buchner funnel. The recovered powder was rinsed with ultrapure water until a neutral pH was achieved and then placed back in the flask with the stir bar. The flask was filled halfway with 0.8% weight per volume (w/v) sodium carbonate solution and placed back in the sand dish with the condenser, thermometer, and plug reattached. The aluminum foil was wrapped loosely around the flask again. The hot plate stirring and heating were turned on and the heat was set high enough so that the solution refluxed. The solution was left to reflux for 24 hours. After 24 hours of heating the flask was allowed to slowly cool by removing the flask from the sand. The solution was vacuum filtered in a Buchner funnel again and rinsed with ultra-pure water until a neutral pH was achieved. The powder was collected and transferred to a watch glass and covered with aluminum foil. Several small holes were poked in the foil with a syringe needle. The foil-covered watch glass was placed in a vacuum oven and left to dry at 60°C under vacuum for 24

hours. After 24 hours, the powder was allowed to cool, and it was scraped into a scintillation vial for storage.

A sign that the process was working to remove all non-chitin material is that the sample would lose color and the solution would take on color during each step. During the HCl step the solution became a light color similar to green tea and the sample lost a little color. However, during the NaOH and sodium bicarbonate steps the solutions became a dark brown like black coffee and the sample turned gray. Figure 3.9 shows a picture of the final chitin product after drying.

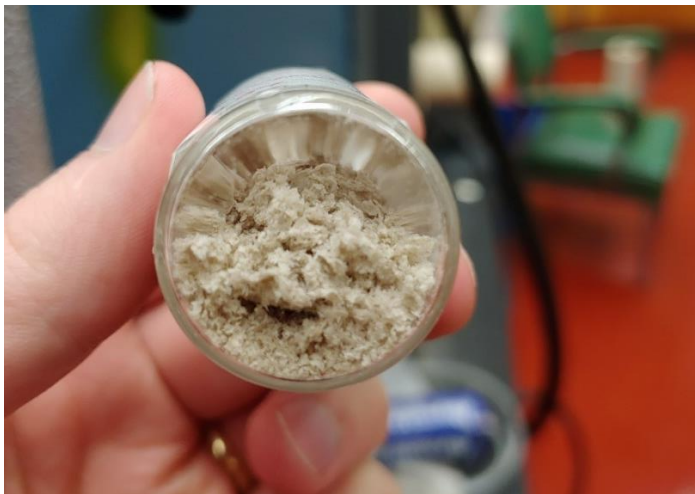


Figure 3.9 Image of the final chitin product after drying.

3.7 NMR Experiment Parameters

Cross-polarization magic-angle spinning (CPMAS) NMR spectra were obtained on a custom-built spectrometer using a Tecmag Redstone console and a 3.55 T magnet (proton frequency of 151.395 MHz). The NMR probe is a transmission-line design. It incorporates a Chemagnetics 7.5 mm pencil rotor spinning assembly with a 14-mm long, 8.65-mm inner diameter, 6-turn coil made of 14-gauge copper wire. Radio-frequency (rf) field strengths were 50 kHz for the ^{13}C channel. The ^1H rf field strength was 50 kHz for ^1H - ^{13}C cross polarization (CP) and 115 kHz for continuous-wave proton decoupling. The rf field strengths for the ^1H and ^{13}C channels were determined by measuring the time for a 2π rotation. The ^1H and ^{13}C power amplifiers were under active control using a custom-built rf controller. Sample spinning speeds were set to 3600 Hz, and the spinning speeds were actively controlled to within 0.2 Hz of the set point. All NMR spectra were obtained using a spin-echo pulse sequence, with the time between the end of the CP pulse and the refocusing π pulse equal to one rotor cycle. Preliminary results showed no difference between spectra obtained on cicada with 1 s and 5 s recycle delays. Approximately 50 mg of each membrane sample was used to obtain the spectra. The cicada, ladybug, and honeybee spectra shown in Figures 4.10 and 4.11 were obtained in 167 h, 140 h, and 140 h, respectively.

MAS-DNP spectra were obtained on approximately 10 mg of cicada wing membrane on a system built with a 14.1 T magnet at the National High Magnetic Field Laboratory in Tallahassee, Florida. The cicada wing membrane sample was impregnated with a 30 mM solution of cAsymPol-POK in 10% DMSO- d_6 /H $_2$ O (1/9 vol %) [10]. The sample was progressively packed into a 3.2 mm sapphire rotor, and the biradical containing solution was

added on top at each step of packing. The radical concentration was chosen to reach optimal enhancements in fully protonated media, based on previous work [10]. Each of the MAS-DNP spectra shown in Figure 4.12 were acquired in 128 s, and the MAS-DNP DQ/SQ spectrum shown in Figure 4.13 was acquired in 72 h. The sample was first spun at room temperature in a home build benchtop spinner and then an EPR spectrum at room temperature was collected on an EMX Nano benchtop EPR spectrometer to check the biradical's mobility. Then the sample was inserted in the MAS-DNP probe cold (~100 K) and spun at 10.5 kHz. The microwave beam was controlled by a quasi-optic setup and the beam polarization was optimized using a Martin-Puplett interferometer [11, 12]. The sample was irradiated with ~12 W of (μ w) power measured at the probe base, which was determined to be optimal. For $^1\text{H} \rightarrow ^{13}\text{C}$ CP, a 20% ramp CP pulse of duration 600 μ s and centered at 50 kHz nutation was applied on the ^1H channel and a 39.5 kHz pulse was applied on the ^{13}C channel. All other pulses on the ^1H channel were 100 kHz and decoupling was carried out using SPINAL64 [13]. For SPC-5 [14], identical conditions were used except that a CW decoupling of 105 kHz was applied during the recoupling. The excitation duration of the DQ recoupling was set to 570 μ s to favor the detection of directly bonded ^{13}C – ^{13}C spin pairs.

References

1. Gonil, P.; Sajomsang, W. Applications of Magnetic Resonance Spectroscopy to Chitin from Insect Cuticles. *International Journal of Biological Macromolecules* 2012, 51 (4), 514–522. <https://doi.org/10.1016/j.ijbiomac.2012.06.025>.
2. Sajomsang, W.; Gonil, P. Preparation and Characterization of α -Chitin from Cicada Sloughs. *Materials Science and Engineering: C* 2010, 30 (3), 357–363. <https://doi.org/10.1016/j.msec.2009.11.014>.
3. Zhang, M.; Haga, A.; Sekiguchi, H.; Hirano, S. Structure of Insect Chitin Isolated from Beetle Larva Cuticle and Silkworm (*Bombyx Mori*) Pupa Exuvia. *International Journal of Biological Macromolecules* 2000, 27 (1), 99–105. [https://doi.org/10.1016/s0141-8130\(99\)00123-3](https://doi.org/10.1016/s0141-8130(99)00123-3).
4. Roberts, G. A. F. Chitin Chemistry Chitin chemistry. Palgrave, London. <https://doi.org/10.1007/978-1-349-11545-7>
5. Broomell, C. C.; Khan, R. K.; Moses, D. N.; Miserez, A.; Pontin, M. G.; Stucky, G. D.; Zok, F. W.; Waite, J. H. Mineral Minimization in Nature's Alternative Teeth. *Journal of The Royal Society Interface* 2006, 4 (12), 19–31. <https://doi.org/10.1098/rsif.2006.0153>.
6. Broomell, C. C.; Mattoni, M. A.; Zok, F. W.; Waite, J. H. Critical Role of Zinc in Hardening of *Nereis* Jaws. *Journal of Experimental Biology* 2006, 209 (16), 3219–3225. <https://doi.org/10.1242/jeb.02373>.
7. HILLERTON, J. E.; VINCENT, J. F. V. The Specific Location of Zinc in Insect Mandibles. *Journal of Experimental Biology* 1982, 101 (1), 333–336. <https://doi.org/10.1242/jeb.101.1.333>.
8. Basic Bug Design - Exoskeletons - Field Station. *Field Station*. April 8, 2014. <https://uwm.edu/field-station/basic-bug-design-exoskeletons/>.
9. Lehnert, M. S.; Reiter, K. E.; Smith, G. A.; Kritsky, G. An Augmented Wood-Penetrating Structure: Cicada Ovipositors Enhanced with Metals and Other Inorganic Elements. *Scientific Reports* 2019, 9 (1). <https://doi.org/10.1038/s41598-019-56203-6>.

10. R. Harrabi, T. Halbritter, F. Aussenac, O. Dakhlaoui, J. Tol, K. K. Damodaran, D. Lee, S. Paul, S. Hediger, F. Mentink-Vigier, S. T. Sigurdsson, G. De Paepe, Highly efficient polarizing agents for MAS- DNP of proton- dense molecular solids. *Angew. Chem. Intern. Ed.* 61 (2022) e202114103.
11. T. Dubroca, A. N. A. N. Smith, K. J. K. J. Pike, S. Froud, R. Wylde, B. Trociewitz, J. E. McKay, F. Mentink-Vigier, J. van Tol, S. Wi, W. W. Brey, J. R. Long, L. Frydman, S. Hill, A quasi-optical and corrugated waveguide microwave transmission system for simultaneous dynamic nuclear polarization NMR on two separate 14.1 T spectrometers. *J. Magn. Reson.* 289 (2018) 35–44.
12. K. R. Thurber, R. Tycko, Low-temperature dynamic nuclear polarization with helium-cooled samples and nitrogen-driven magic-angle spinning. *J. Magn. Reson.* 264 (2016) 99–106.
13. B. M. Fung, A. K. Khitrin, K. Ermolaev, An improved broadband decoupling sequence for liquid crystals and solids. *J. Magn. Reson.* 142(1) (2000) 97–101.
14. M. Hohwy, C. M. Rienstra, C. P. Jaroniec, R. G. Griffin, Fivefold symmetric homonuclear recoupling in rotating solids: Application to double quantum spectroscopy, *J. Chem. Phys.* 110 (1999) 7983-7992.

Chapter 4 Results and Discussion

4.1 Introduction

The insect wing is considered an extension of the exoskeleton. The goal of this research is to determine the chemical composition of insect wing membranes and provide insight into the architecture of the wing membrane. Is the wing membrane similar to the exoskeleton or does it conform to the textbook model of back-to-back layers of epicuticle? Membrane samples from cicada, honeybee, ladybug, and butterfly were analyzed. The chemical composition of the membrane will be obtained with solid state NMR.

It is commonly observed that many insects have hairs on the membranes of their wings. These hairs may comprise a noticeable amount of the total mass of the wing. Honeybee, ladybug, and butterfly all have hairs on their wing membranes whereas cicada do not. The hair contribution to the sample mass was determined using optical microscopy.

4.2 Membrane Thickness of Insect Wings

Images of the insect wing membranes were obtained using a Nikon ME600 microscope and a PixeLINK PL-B742U camera. Edge-on views of the insect wing membranes of the cicada, honeybee, ladybug, and butterfly are shown in Figure 4.1. The membrane thickness of each insect was determined by analyzing ten samples and taking the average. The average thickness of the wing membrane was $4.70 \mu m$, $1.63 \mu m$, $1.43 \mu m$ and $1.16 \mu m$ for the cicada, honeybee, ladybug, and butterfly, respectively. The cicada membrane is about 3 to 4 times thicker than the membranes of the other three insects. All of the images were taken with the cut edges held perpendicular to the stage of the microscope so that the edge could be accurately measured. The images in Figure 4.1 of the honeybee (B), ladybug (C), and butterfly (D) wing membranes have shading above or below the edge of the wing. This is due to portions of the sample that are not in focus casting a shadow on the image. This phenomenon is not present to the same degree in the images of the edges of cicada (A) wing membranes because the cicada samples were more rigid and maintained a flat shape without curling or bending.

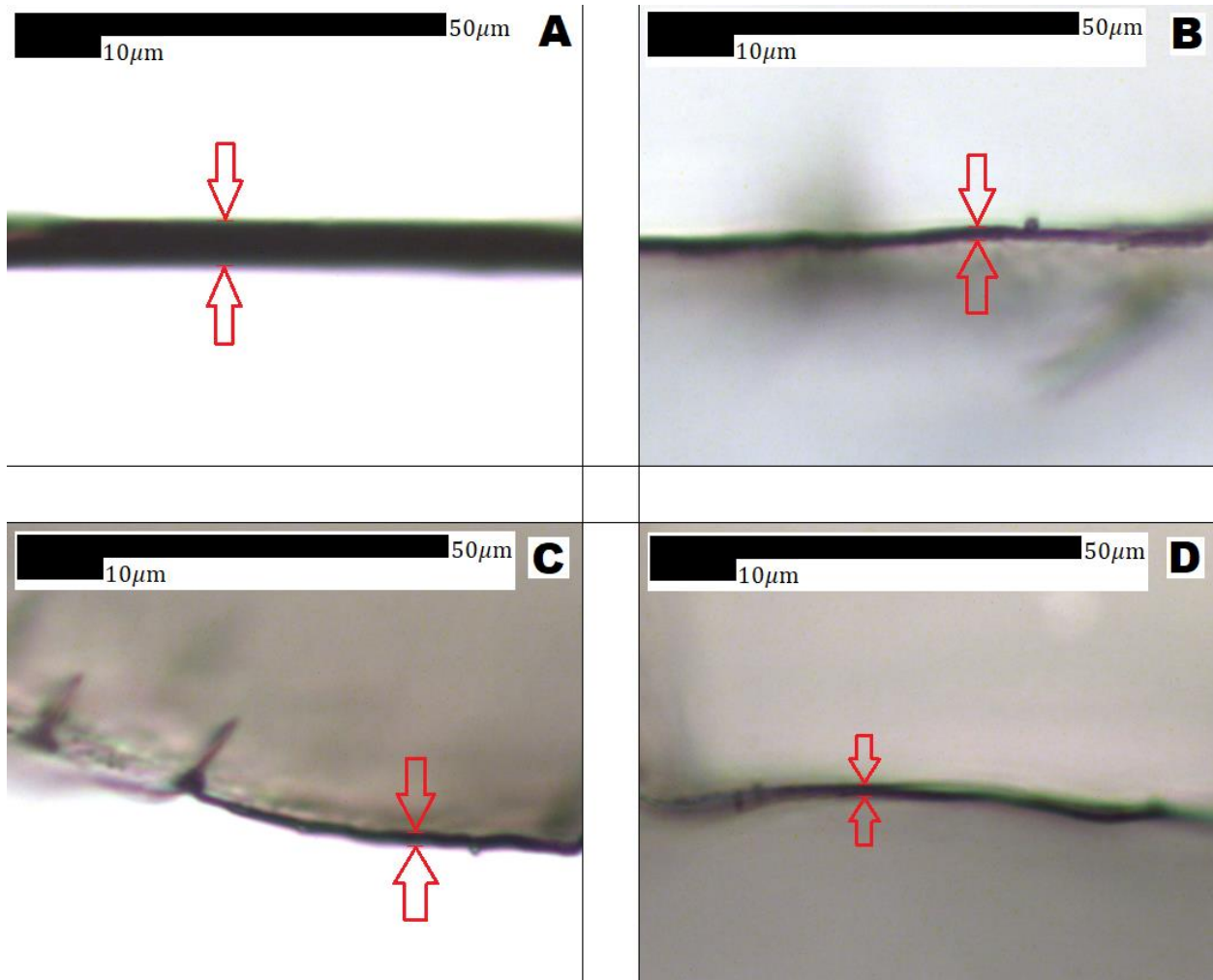


Figure 4.1 Edges of wing membranes. A) Cicada wing membrane under 50x magnification. B) Honeybee wing membrane under 50x magnification. C) Ladybug wing membrane under 50x magnification. D) Butterfly wing membrane under 50x magnification. The arrows indicate the thickness of the wing membrane at the point of measurement.

Epicuticle contains only protein and is between 0.5 and 2 μm in thickness [1]. Procuticle is much thicker, ranging from 10 to over 200 μm and contains both protein and chitin [1]. The thickness of the ladybug, butterfly, and honeybee would appear to support the epicuticle-only model. The larger thickness of the cicada may support a more complex morphological structure of the wing membrane. However, thickness measurements alone cannot determine if epicuticle or procuticle models are correct.

4.3 Surface Hairs

Figure 4.2 shows images of the surface of each insect wing membrane. It is clear that ladybug, honeybee, and butterfly have hairs on their wing membrane surfaces and that cicada do not. The cicada, honeybee, and butterfly images were taken at 10x magnification. Due to the small size of the ladybug hairs, the magnification was increased to 20x for the ladybug sample. In the ladybug, honeybee and butterfly samples the hairs, are present over the entire membrane and are distributed evenly. Hairs occur on both surfaces of the wing membrane. Since, the membranes were stored loosely in scintillation vials, the information as to which side of the membrane corresponds to the dorsal or ventral side of the insect was not preserved. When counting the hairs under the microscope the hairs were counted regardless of whether they were on the top surface or bottom surface of the membrane.

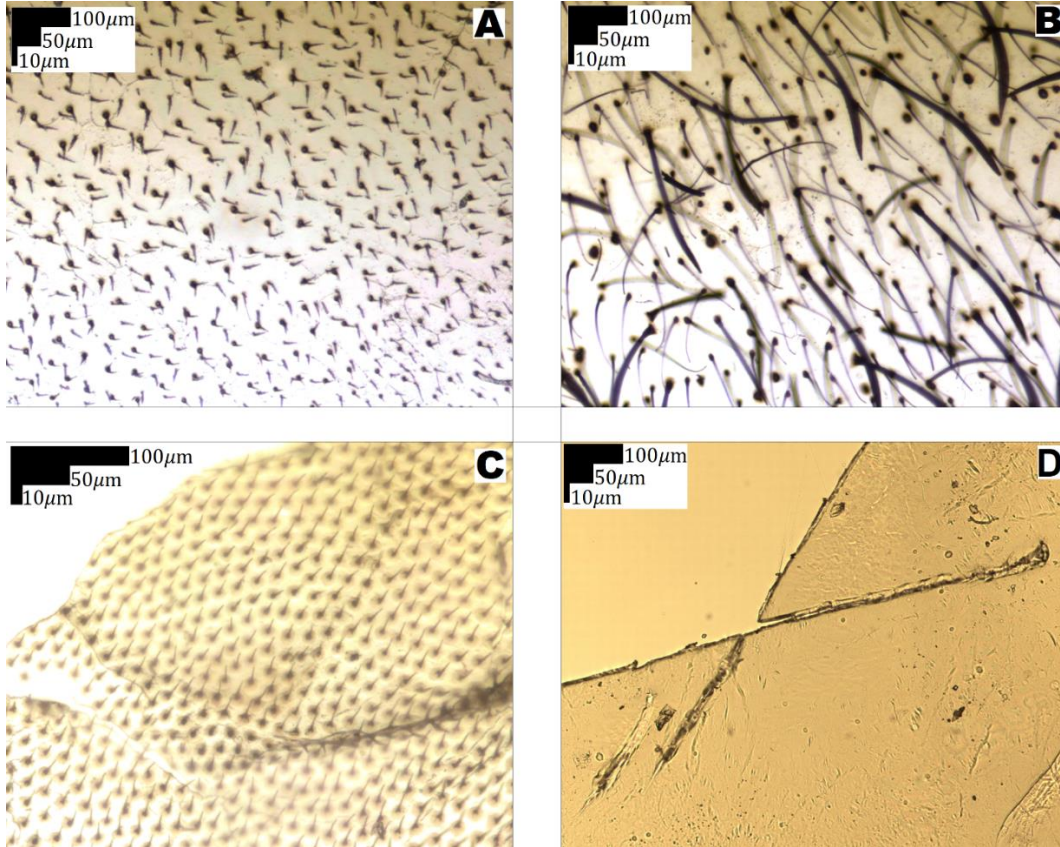


Figure 4.2 Wing membrane hair images. A) Honeybee wing membrane under 10x magnification. B) Butterfly wing membrane under 10x magnification. C) Ladybug wing membrane under 20x magnification. D) Cicada wing membrane under 10x magnification.

The volume, (V_h) of a hair was calculated by treating each hair as a right circular cone as an approximation according to Equation 4.1

$$V_h = \frac{\pi hr^2}{3} \quad \text{Eq 4.1}$$

The volume of the cone requires the measurement of the radius, r , of the cone base and the height, h , of the cone. First, images of the hairs under magnification were examined to find hairs that could be easily distinguished from the background color. An example of selecting a hair on the surface of a honeybee wing membrane is shown in Figure 4.3 A. The pixel coordinates that mark the width of the base of the hair approximately and perpendicular to the shaft were

recorded along with the pixel coordinate of the tip of the hair. In Figure 4.3 C the process of selecting the pixels for measuring a hair on the surface of a honeybee wing membrane is shown.

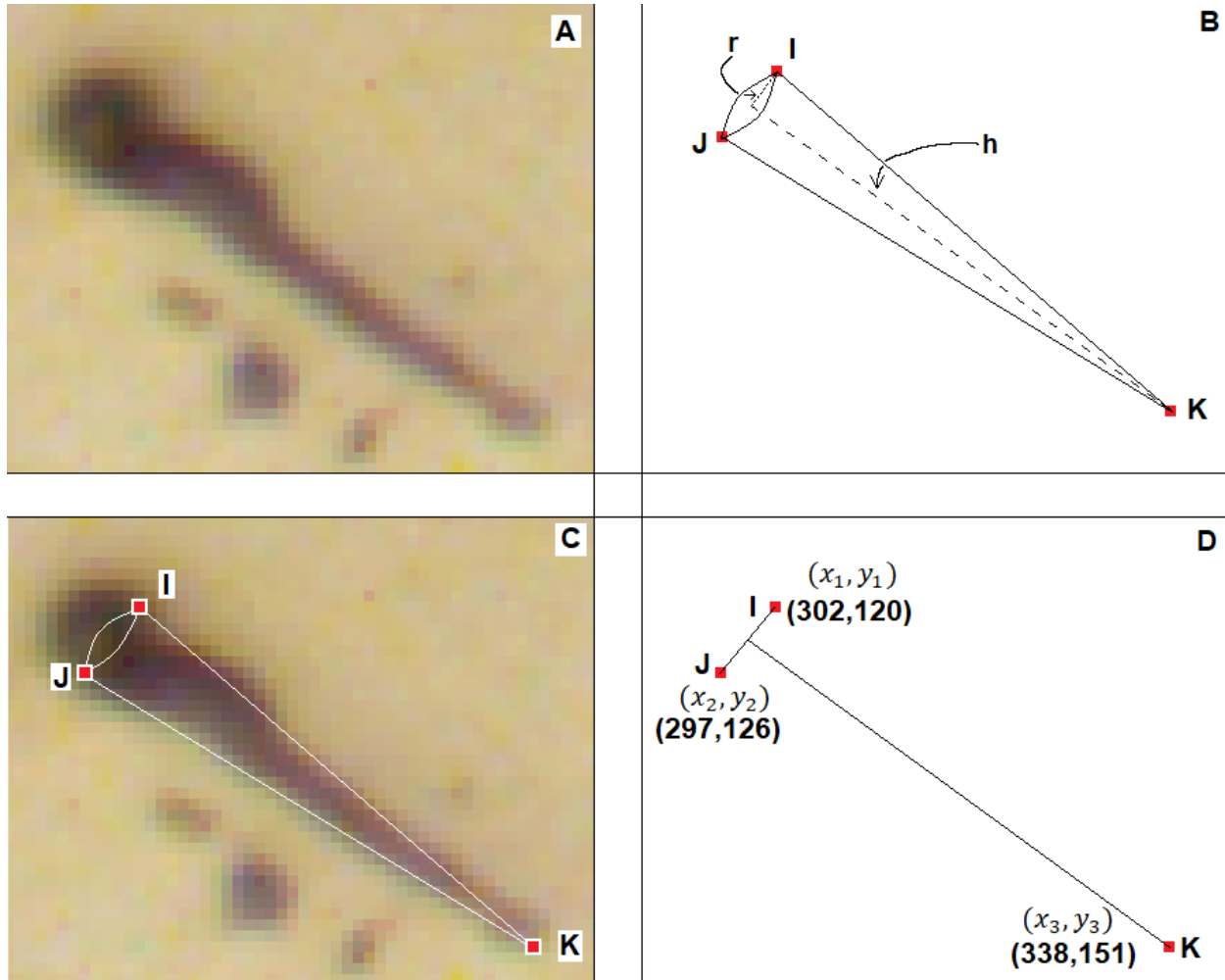


Figure 4.3 Visualization of how the volume of a honeybee wing membrane hair was calculated. A) Image of the hair to be measured. B) An image of a cone bound by points I, J, and K with the radius and height of the cone identified. C) The hair is treated as a cone with points I, J, and K superimposed upon it. D) The (x,y) coordinates of each pixel are used to measure the hair base width and the hair height, and sample coordinates are provided for one particular hair.

The radius of the base of the hair was calculated using the coordinates of the pixels defining the diameter selected from the image using Equation 4.2.

$$r = \frac{1}{2} \sqrt{(x_2 - x_1)^2 + (y_2 - y_1)^2} \quad \text{Eq 4.2}$$

The (x,y) pixel coordinates of the hair in Figure 4.3 for points determining the diameter of the base of the cone are (302,120) and (297,126) and were used to determine r

$$r = \frac{1}{2} \sqrt{(297 - 302)^2 + (126 - 120)^2} = \frac{7.81}{2} \text{ pixels} = \frac{5.2}{2} \mu\text{m} \quad \text{Eq 4.3}$$

The height of the cone is calculated by finding the distance between the tip of the hair and the center of the base of the hair. The center of the base of the hair is found by taking the average x position and the average y position of the two points determining the diameter of the base of the cone.

$$h = \sqrt{\left(\frac{x_2+x_1}{2} - x_3\right)^2 + \left(\frac{y_2+y_1}{2} - y_3\right)^2} \quad \text{Eq 4.4}$$

For example, the height of the hair in Figure 4.3 was calculated using the same (x,y) pixel coordinates for the base of the hair, (302,120) and (297,126), and the coordinates for the point at the tip of the hair, (338,151), as shown in Equation 4.5.

$$h = \sqrt{\left(\frac{297+302}{2} - 338\right)^2 + \left(\frac{126+120}{2} - 151\right)^2} = 47.61 \text{ pixels} = 31.7 \mu\text{m} \quad \text{Eq 4.5}$$

Fifteen hairs were measured to get the average base diameter of 0.0051 mm and average height of 0.0303 mm. The average volume, \overline{V}_h , of the honeybee hair is,

$$\overline{V}_h = \frac{\pi h r^2}{3} = \frac{0.0303 \text{ mm} \left(\frac{0.0051 \text{ mm}}{2}\right)^2}{3} \pi = 2.038 \times 10^{-7} \text{ mm}^3 \quad \text{Eq 4.6}$$

Because butterfly hairs are approximately 100 μm long and curved, a spline was generated from points along the shaft of the hair to represent the length of the hair more accurately than just the end point in the cone model. This is illustrated in Figure 4.4 where points are generated for the curved tip of a butterfly hair. A series of points along the hair shaft were

selected. The lengths of \overline{KL} , \overline{JK} and \overline{IJ} , etc were calculated and summed to get the length of the hair.

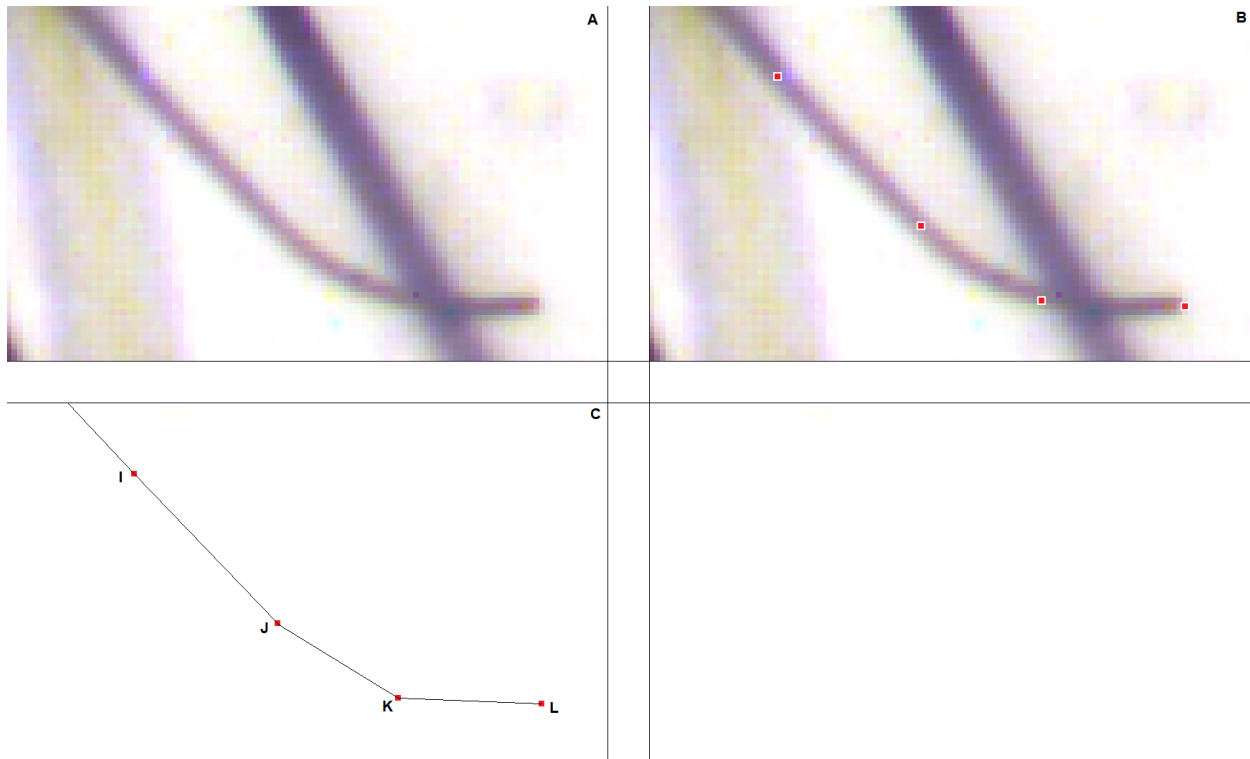


Figure 4.4 The process of generating splines to determine the length of the butterfly hairs. A) Image of the hair to be measured. B) The measurement points are determined, and the pixels are colored red. C) The spline is generated from the points selected.

The hairs on the surface of the insect wing membrane cannot be completely separated from the membrane, whether mechanically or chemically, while maintaining workable sample sizes. The hairs and membrane are assumed to have the same density in order to determine their percentage mass contributions. This is a reasonable assumption because the density of protein is approximately 1.4 g/cm^3 [2] and the density of chitin is also approximately 1.4 g/cm^3 [3]. Given that the densities of bulk chitin and protein are similar, the percent contribution of mass from the membrane and hairs are independent of their respective chitin-protein compositions.

The NMR signal will come from membrane and hair. In case resonances from hair and membrane overlap, it is necessary to know the mass ratio of hair and membrane to determine the contribution of hair and membrane to overlapping resonances.

To determine the number of hairs per unit area on the surface of the insect wing membranes, ten samples of each insect wing membrane were used. An image of each sample was taken at 10x magnification for butterfly and honeybee and 20x for ladybug. For honeybee and butterfly samples a region 600 pixels by 600 pixels was used to count hairs, which corresponds to a 400 μm by 400 μm area. For the ladybug images, a region 300 pixels by 300 pixels (which corresponds to 100 μm by 100 μm) within each image was used to count the hairs. The butterfly wing membranes have large hairs and small hairs, and the dimensions of both were measured separately. For the final hair volume calculation, the volume of both hair sizes were combined to determine the total hair volume for the butterfly samples.

Table 4.1 summarizes the physical measurements made by optical microscopy. Assuming that the hairs and the membranes have similar densities, the mass ratio of hair to membranes can be determined. In the case of cicada, there are no hairs so 100% of the sample is the membrane. Hair composes 17% of the mass of the ladybug sample and 8% of the mass of the honeybee sample. However, in the case of the butterfly the hairs make up 33% of the total volume of the sample, and consequently about one third of the butterfly sample mass can be attributed to the hairs. Consequently, the NMR signal in the cicada, honeybee, and ladybug samples will be largely determined by the membrane; however, the butterfly will have substantial contribution to the NMR signal from the hairs.

Insect	Membrane Thickness mm	Membrane Area mm ²	Avg Hairs per 0.16 mm ²	Membrane Volume mm ³ per 0.16 mm ²	Total Hair Volume mm ³ per 0.16 mm ²	Total volume mm ³ per 0.16 mm ²	Membrane volume %	Hair volume %
Cicada	0.00470	0.16	0	7.530x10 ⁻⁴	N/A	7.530x10 ⁻⁴	100.00	N/A
Bee	0.00162	0.16	117.5	2.602x10 ⁻⁴	2.394x10 ⁻⁵	2.842x10 ⁻⁴	91.57	8.43
Butterfly	0.00142	0.16	3.6 Large 35.5 Small	2.282x10 ⁻⁴	1.135x10 ⁻⁴	3.417x10 ⁻⁴	66.78	33.22
Ladybug	0.00116	0.01	956.8	2.245x10 ⁻⁴	9.731x10 ⁻⁶	1.953x10 ⁻⁴	82.66	17.33

Table 4.1 Summary of the physical characteristics of the insect wing membranes. Calculated membrane thickness, average hairs per 0.16 mm², membrane volume per 0.16 mm², total hair volume per 0.16 mm², total volume per 0.16 mm², membrane and hair percentages of cicada, honeybee, butterfly, and ladybug wing membranes.

4.4 ^1H - ^{13}C CPMAS NMR of Ladybug Elytra

Solid State NMR had previously been used to determine the chemical composition of insect exoskeletons, an example of which is the rice weevil *Sitophilus Oryzae*. Figure 4.6 shows the ^1H - ^{13}C CPMAS spectra of the rice weevil beetle cuticle. The spectra shows the presence of chitin, protein, and catechol content. The chemical origin of each resonance in the spectra is listed in Table 4.2 [4], the structure of the chitin repeat unit (N-acetylglucosamine) is displayed in Figure 4.5 for reference.

^{13}C resonance position (ppm)	Assignment
172	carbonyl carbons of chitin, protein, lipid, and catechol acyl groups
170	carbonyl carbons of oxalate
155	phenoxy carbon of tyrosine, guanidino carbons in arginine
144	phenoxy carbons of catechols
129	aromatic carbons
116	tyrosine carbons 3 and 5, imidazole carbon 4, catechol carbons 2 and 5
104	GlcNAc carbon 1
82	GlcNAc carbon 4
75	GlcNAc carbon 5
72	GlcNAc carbon 3
60	GlcNAc carbon 6, amino acid α -carbons
55	GlcNAc carbon 2, amino acid α -carbons
44	aliphatic carbons of amino acids, catechols, and lipids
33	aliphatic carbons of amino acids, catechols, and lipids
23	methyl carbons of chitin, protein, lipid, and catechol acyl groups; amino acid methyne carbons
19	methyl carbons of amino acids and lipids

Table 4.2 ^{13}C isotropic chemical shifts for components common to insect cuticle. The original values for cuticle components from the Schaefer et al. [4] paper appear in the table. A similar table was published by Peter et al [5]. The repeat unit for chitin, along with carbon position labels, is shown for reference in Figure 4.7.

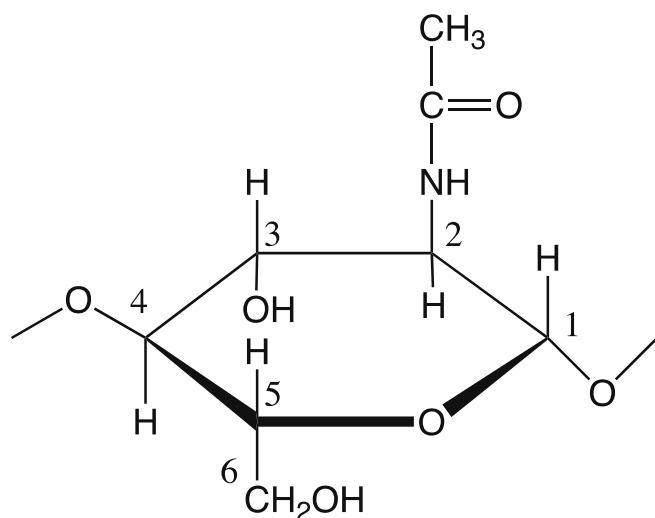


Figure 4.5 N-acetylglucosamine, the chitin repeat unit with the carbons numbered 1 through 6.

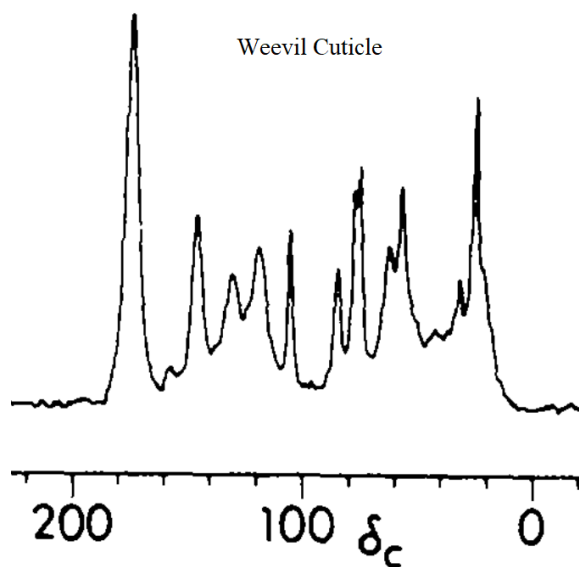


Figure 4.6 ^{13}C CPMAS spectra of the wild type rice weevil (*Sitophilus Oryzae*) cuticle [6]

Ladybugs have a modified forewing in the form of an elytra which is a defining characteristic of the order *Coleoptera* (beetle) to which they belong. The elytra is a rigid shell approximately 40 μm thick that protects the hindwing and the body of the ladybug. When the ladybug is not flying the membrane containing hindwings are folded between the elytra and the

abdomen of the ladybug. Before the ladybug can begin to fly the elytra open and swing forward so the hindwings can spring out and have a free range of motion to allow the ladybug to take flight. The elytra play no active role in flight as they remain stationary. Unlike the hindwing of the ladybug, the elytra lacks both veins and membrane and is opaque.

The distinct physical characteristics and functions of the elytra and hindwings of the ladybug suggest that their underlying chemical structures may be different. The ^1H - ^{13}C CPMAS spectra of ladybug elytra prior to and after treatment with acetone are shown in Figure 4.7. The indicated resonances are tabulated in Table 4.2. The most notable difference between the two spectra is the resonance at 29 ppm. The 29 ppm resonance is significantly weaker in the acetone washed sample and is associated with the long chains of aliphatic carbons found in lipids. The reduction in signal strength at 29 ppm is the result of the removal of lipids by acetone.

Figure 4.7 shows a clear indication of chitin content present in the ladybug elytra, indicated by the resonances at 73, 74, 83, and 103 ppm which correspond to the chitin repeat unit N-acetylglucosamine (GlcNAc) GlcNAc carbon 3, GlcNAc carbon 5, GlcNAc carbon 4, and GlcNAc carbon 1 of the chitin repeat unit as indicated by Table 2 [5]. The resonances in the region of 40-48 ppm and the resonances at 129 ppm and 155 ppm correspond to the protein content. The resonance at 129 ppm corresponds to aromatic carbons and the resonance at 155 ppm corresponds to phenoxy carbons of tyrosine and guanidino carbons in arginine. The peaks at 54 and 59 ppm are composed of contributions from both chitin and protein, with the 54 ppm resonance corresponding to GlcNAc carbon 2 and amino acid alpha carbons and the resonance at 59 ppm corresponding to GlcNAc carbon 6 of the chitin repeat unit and amino acid alpha carbons. The peak at 172 ppm corresponds to contributions from carbonyl carbons of chitin, protein, lipids, and the acyl groups of catechols. The peak at 143 ppm corresponds to the

phenoxy carbons from catechols. The peak at 143 ppm is important because it comes only from catechol. It is isolated and doesn't have any resonance overlap with either chitin or protein content. The peak at 116 ppm is composed of contributions of tyrosine carbons 3 and 5, imidazole carbon 4 and catechol carbons 2 and 5. The peak at 22 ppm corresponds to methyl carbons of chitin, protein, lipid, catechol acyl groups and amino acid methyne carbons. The peak at 19 ppm corresponds to the methyl carbons of amino acids and lipids. It is apparent when comparing the spectra of Beetle exoskeleton Figure 4.6 and ladybug elytra in Figure 4.7 that the elytra have a chemical composition that is very similar to that of insect exoskeleton.

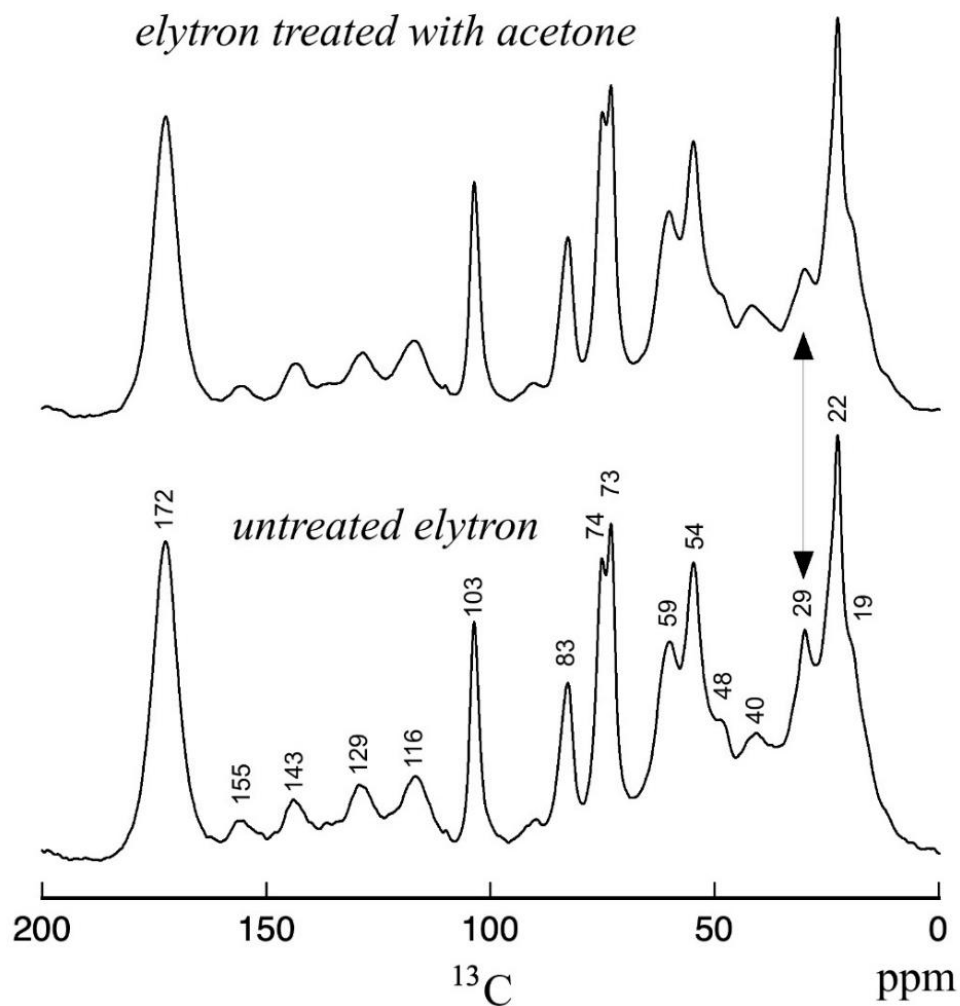


Figure 4.7 The comparison of the ^1H - ^{13}C CPMAS spectra of ladybug elytra. The top spectra was acquired after first washing the harvested ladybug elytra with acetone. The bottom spectra is of the untreated elytra. The spectra were obtained at room temperature on the 151 MHz (proton) spectrometer. This spectra shows that the elytra of the ladybug are coated with a layer of lipid as indicated by the resonance at 29 ppm, which dramatically changes intensity after the treatment with acetone.

Catechols serve as crosslinkers that may bind chitin and protein together. This provides strength and durability to the cuticle. The crosslinking occurs through a process known as sclerotization or tanning. In addition to providing structural benefits to the cuticle, sclerotization is responsible for the color change in the cuticle, causing it to turn brown or tan. Schaefer *et al.* [4] used solid state NMR to analyze the chemical composition and sclerotization process of the cuticle of the tobacco hornworm *Manduca Sexta*. In this work Schaefer *et al.* isotopically labelled the larval stage specimens by injecting them with ^{15}N labelled histidine, ring- $^{13}\text{C}_6$ labelled dopamine, and feeding them a diet spiked with $^{13}\text{C}(\text{U})$ labelled glucose. Through this investigation Schaefer *et al.* developed a model of the crosslinking in the insect cuticle between chitin and a histidine residue of protein via a catechol which is illustrated in Figure 4.8.

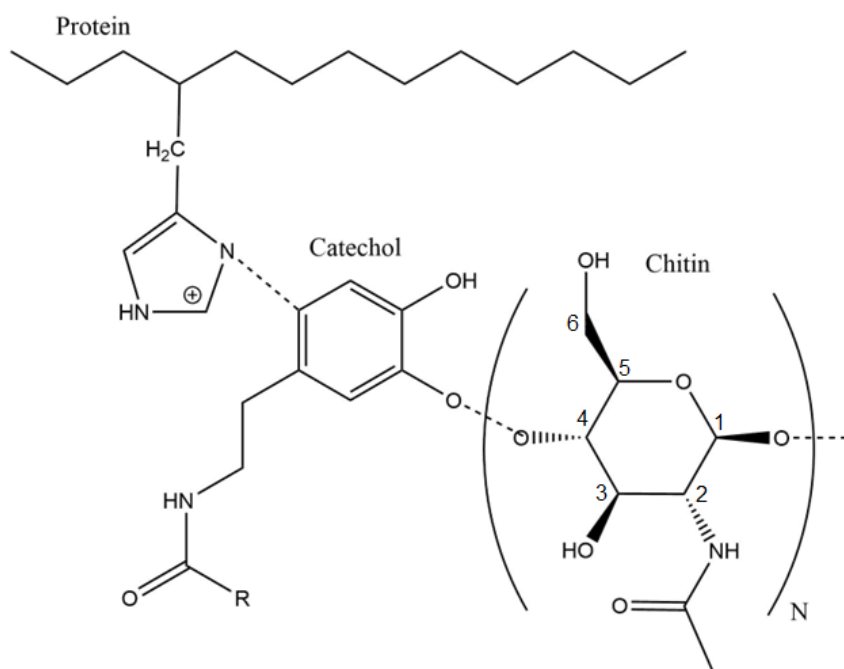


Figure 4.8 A diagram of how catechols facilitate sclerotization crosslinking between protein and chitin via a histidine residue. Sourced from [4]

Figure 4.9 compares the ^1H - ^{13}C CPMAS spectra of the elytra and membrane of the hindwing of the ladybug. The spectra shows a clear indication of chitin content present in both

the ladybug membrane and the elytra as indicated by chitin-associated resonances at 73, 74, 83, and 103 ppm. The resonances in the region between approximately 40-48 ppm and the resonances at 129 ppm and 155 ppm show the protein content of the sample. The spectra for the wing membranes shows that there is a much greater contribution from protein than what is found in the elytra as indicated by the peak intensity at 129 ppm and in the region around 40 ppm.

The spectra of elytra treated with acetone indicates that the elytra is largely composed of chitin. This is corroborated by the stiff and inflexible nature of the elytra. There is some protein contribution to the elytra spectra, but to a lesser degree. The resonance at 143 ppm in the elytron spectra indicates the presence of catechols. However, it is worth noting that the membrane contains chitin and protein but is apparently devoid of catechol content.

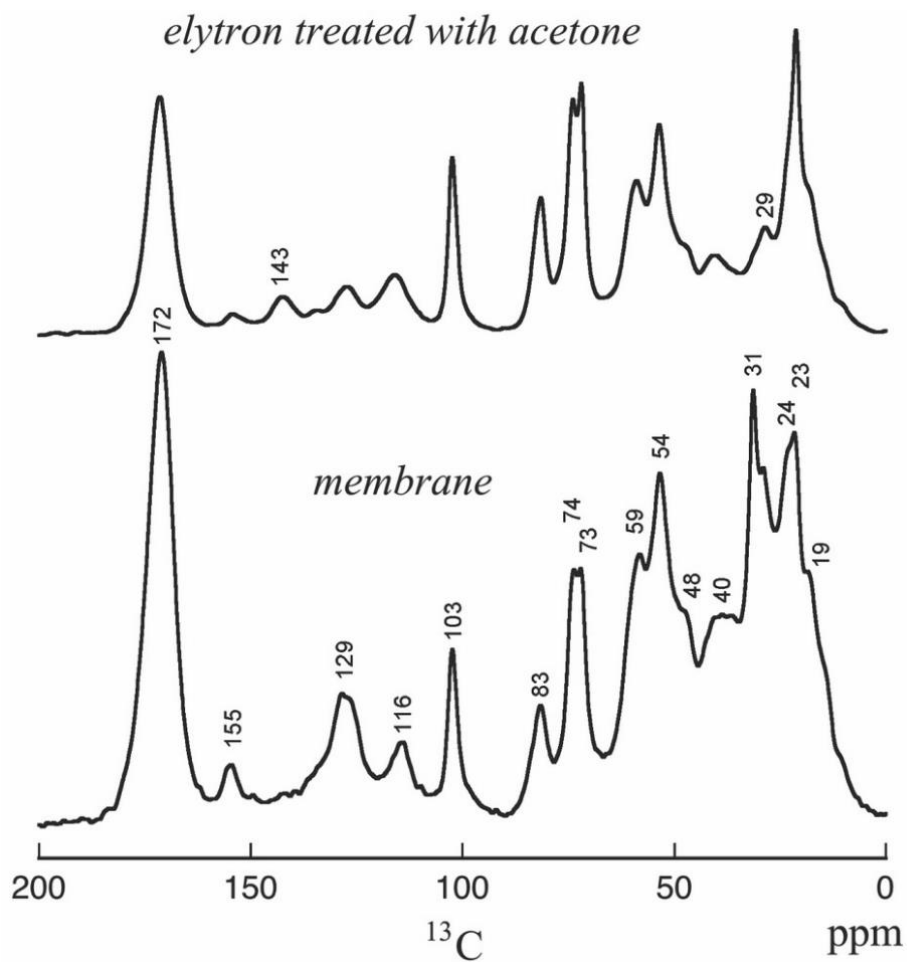


Figure 4.9 The ^{13}C CPMAS spectra of the ladybug elytron after acetone washing compared to the spectra of the ladybug membrane. The spectra were obtained at room temperature on the 151 MHz (proton) spectrometer.

4.5 ^1H - ^{13}C CPMAS NMR of Cicada, Ladybug, Honeybee and Butterfly Wing Membranes

Figure 4.10 compares ^{13}C spectra of ladybug, honeybee, and butterfly scaled such that the magnitude of the resonance at 103 ppm from the GlcNAc carbon 1 in chitin is the same in all three spectra. Figure 4.11 shows an expanded view of the cicada, honeybee and ladybug spectra. The resonance at 103 ppm (in reference to Figure 4.10) is only from chitin, meaning that across the three spectra the contribution from chitin content is standardized, so differences between the spectra must come from differing protein content. The cicada spectra in Figure 4.11 has a significantly weaker chitin contribution than the other spectra and is consequently scaled such that the resonance at 172 ppm, which corresponds to carbonyl carbons, is of commensurate intensity to the other spectra.

The cicada spectra shows the presence of chitin, protein, and lipid. Contributions from protein dominate the cicada spectrum. These contributions can be seen by comparing the relatively low-intensity peaks from chitin near 72, 75, 82, and 104 ppm with the greater intensity resonances in the 40 -50 ppm region corresponding to protein content. Of importance is the lack of a well-defined resonance at 143 ppm associated catechols. This is also true of the ladybug spectra. This is important because catechols are responsible for facilitating sclerotization via crosslinking. A lack of catechol content implies that sclerotization either does not occur to the same degree as in the other insects spectra or that it occurs by a different mechanism.

The chitin resonances near 72, 75, 82, and 104 are much more intense in the spectra of the ladybug, honeybee, and butterfly samples. This increased chitin contribution cannot be explained solely by the presence of hairs on the wing membranes of the ladybug, honeybee, and

butterfly samples because the low mass contributions of the hair cannot account for the signal intensity observed. Consequently, the membranes of these species must contain most of the chitin content observed.

The butterfly and honeybee spectra present clearly defined resonances at 143 ppm, indicating the presence of catechols. The presence of catechol content implies that sclerotization crosslinking takes place. The most intense resonance of the butterfly spectra is the resonance at 31 ppm coming from lipid. This was verified by washing the sample in chloroform and observing a much less intense resonance at 31 ppm. The lipid resonances found at 31 ppm were present in the other spectra, but to a much lesser extent than found in the butterfly sample.

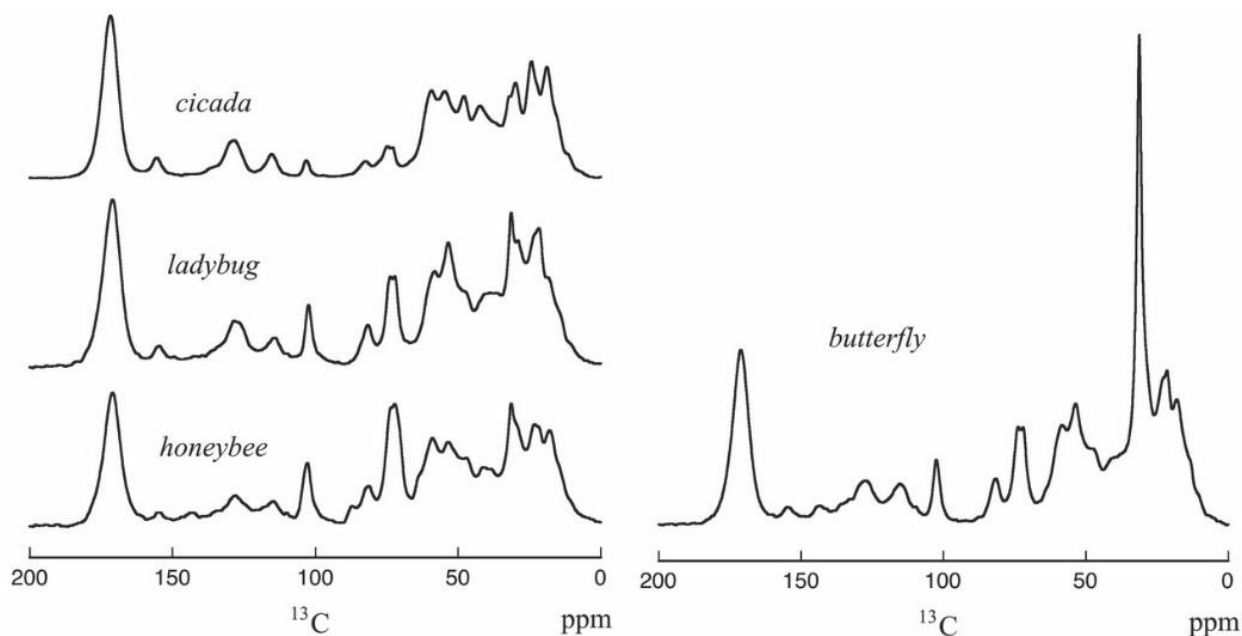


Figure 4.10 Comparison of the ^{13}C CPMAS spectra of the membranes harvested from the butterfly, cicada, ladybug, and honeybee. No chemical treatments were done to these samples. The spectra were obtained at room temperature on the 151 MHz (proton) spectrometer.

The cicada membrane spectra (Figure 4.11) show the expected resonances from protein, but it also shows resonances uniquely identifiable to chitin. The presence of chitin content in the membrane of the cicada wing is in conflict with the traditional textbook model of the structure of

insect wing membranes being composed of ventral and dorsal layers of epicuticle without the presence of chitin. This discrepancy prompted us to investigate the chemistry of the wing membranes of other insect species. We obtained ^{13}C NMR spectra of the wing membranes of cicada (*Magicicada cassini*), honeybee (*Apis mellifera ligustica*), ladybug (*Hippodamia convergens*), and amber phantom butterfly (*Haetera piera*; Peru). Chitin content was detected in the wing membranes of all four species, however the relative contribution of the chitin content to protein and lipid content varies from species to species. It appears that the textbook model needs to be abandoned or modified. The mechanism of catechol crosslinking may be different between the insect species.

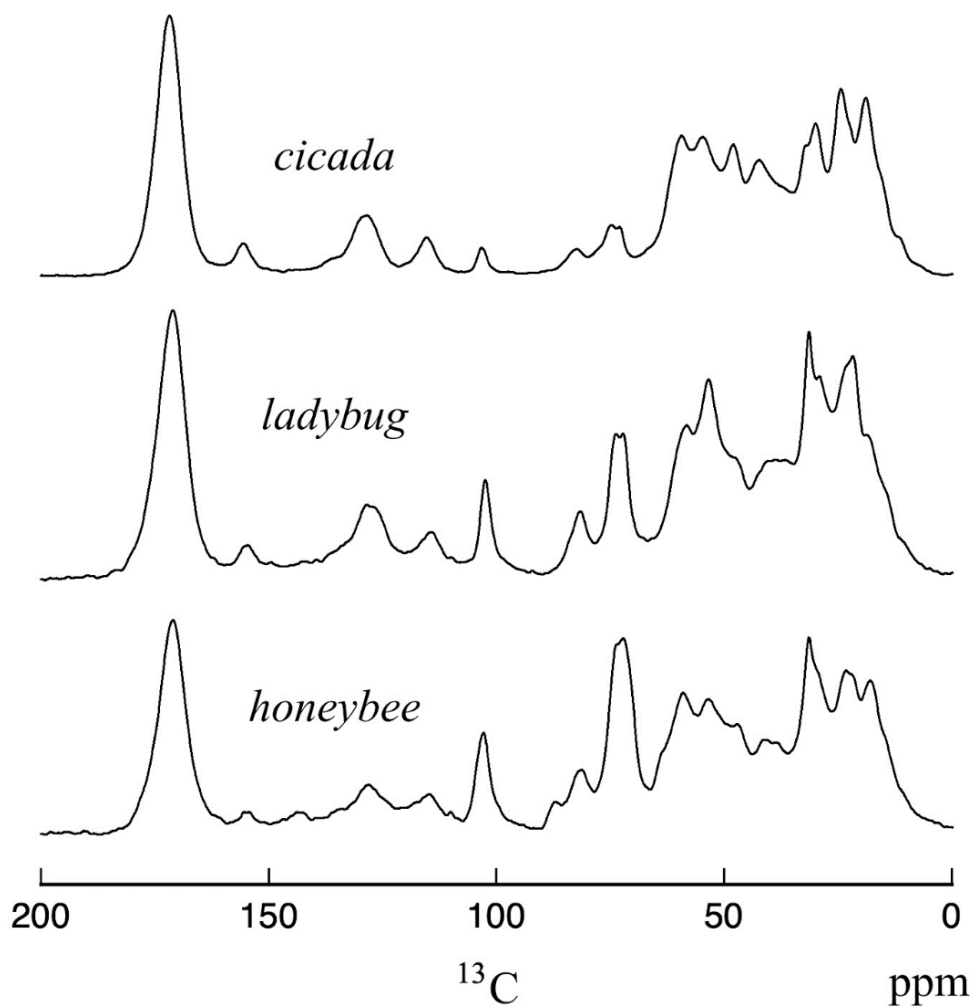


Figure 4.11 The ^{13}C CPMAS spectra of the wing membranes of the Cicada, Ladybug and Honeybee. The spectra were obtained at room temperature on the 151 MHz (proton) spectrometer.

4.6 MAS-DNP NMR

Performing low field ^1H - ^{13}C CPMAS NMR on natural abundance biological samples is incredibly challenging and time consuming. The two greatest challenges are acquiring sufficient sample mass and the significant number of scans that are needed. As noted in the experimental section only approximately 30 mg of sample were obtained for each sample and days were required to obtain spectra with good signal-to-noise ratio.

Magic angle spinning dynamic nuclear polarization (MAS-DNP) experiments provide significant NMR signal enhancement without the need for isotopic enrichment [7-20]. Both the requisite sample quantity and the number of scans can be significantly reduced when taking advantage of the significant signal enhancement MAS-DNP provides. Furthermore, the signal enhancement can be further leveraged to provide ^{13}C - ^{13}C multidimensional experiments from natural abundance samples, something that has not been done to date.

Figure 4.12 shows a ^1H - ^{13}C CPMAS-DNP spectra of the cicada wing membrane acquired on a spectrometer equipped with DNP at the National High Magnetic Field Laboratory in Tallahassee, Florida. The bottom spectra was obtained with microwave power on and the top spectra was obtained without any microwave power. Both spectra were acquired with 128 scans on approximately 5 mg of sample. The spectra without DNP enhancement is scaled by a factor of 5 for clarity. The enhancement provided by DNP in this case is approximately $\varepsilon = \text{on}/\text{off} \approx 22$. Cicada wing membranes are approximately 4.7 micrometers thick, and the similarities between the DNP enhanced spectra and the previously acquired low-field spectra indicate that either that the MAS-DNP enhancement process correctly assess the bulk sample and/or the membrane surface chemistry is substantially similar to the bulk membrane chemistry.

However, the MAS-DNP saturation-recovery curves could be fitted by a mono-exponential curve with a buildup time of 1.5 seconds, indicating that the sample is homogeneously polarized. Originally there was concern with the low-field ^{13}C CPMAS cicada wing membrane results as there is an absence of a resonance near 144 ppm, which would be indicative of catechol crosslinkers. There is a possibility that the resonance was simply weak and buried under the noise. The superb signal-to-noise ratio afforded by MAS-DNP with ^1H - ^{13}C CP shows no sign of catechols present in the membranes of cicada. The 144 ppm resonance associated with the phenoxy carbons of catechols did not appear when the CP contact time was varied from 100 to 1500 μs , and it did not appear during a multi-CP experiment using seven 100 μs CP pulses with delays of 2s [21]. The MAS-DNP spectra in Figure 4.12 yielded an excellent signal-to-noise ratio, suggesting that ^{13}C - ^{13}C multidimensional NMR experiments are possible.

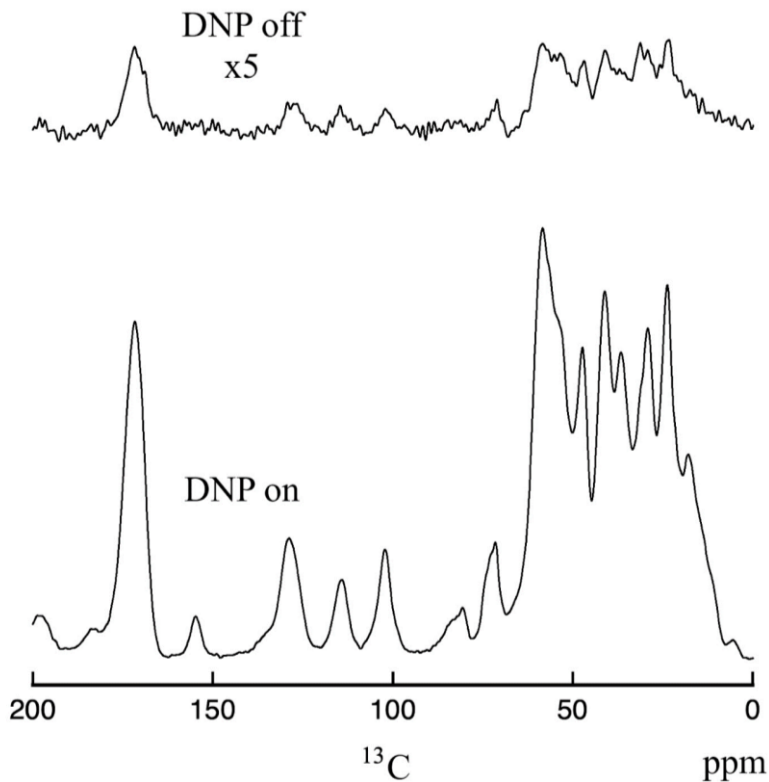


Figure 4.12 The ^1H - ^{13}C CPMAS spectra of cicada wing membrane, showing results with DNP off (top scaled by 5x) and DNP on (bottom). The spectra were acquired on the 600 MHz (proton) MAS-DNP spectrometer at the national high magnetic field laboratory in Tallahassee, Florida collected at a sample spinning rate of 10.5 kHz. Both spectra were obtained with 128 scans.

Figure 4.13 shows a two-dimensional, natural-abundance ^{13}C - ^{13}C double-quantum, single-quantum MAS-DNP NMR spectra acquired using 10 milligrams of cicada membrane sample. There is a good signal-to-noise ratio. The readily assignable cross peaks are indicated with horizontal red lines and the ^{13}C resonances from chitin that overlap with some protein resonances are labelled according to Table 4.2. The advantage of multidimensional NMR is that resonances from disparate sources that overlap one another in one dimensional spectra can now be resolved. In the center of the ^{13}C - ^{13}C spectra the main carbons of the chitin repeat unit, and their cross peaks show the contribution from chitin. The C6 and C2 resonances of chitin at 60 and 55 ppm, which in the one-dimensional spectra overlap with contributions from protein, can

be seen separated from the non-chitin contributions. The nature of the cross peaks and how they arise is discussed later.

It is important to point out the Glycine (Gly) resonances associated with the alpha and carboxyl carbons of Glycine at the bottom of the spectra have three distinct cross peaks marked in red. These three separate crosspeaks suggest that there are three possible dihedral angles between the carboxyl carbon carbon-oxygen bond and the alpha carbon carbon-nitrogen bond, of that there could be three different glycine environments present in the sample.

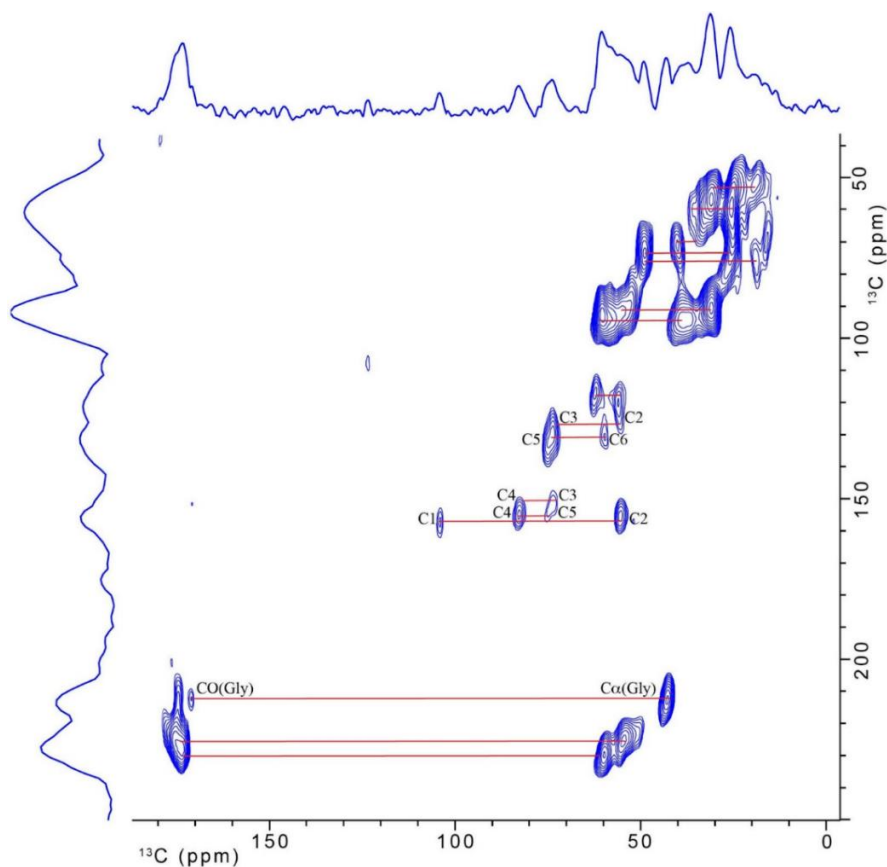


Figure 4.13 The natural abundance ^{13}C - ^{13}C double-quantum/single-quantum spectra of the cicada wing membrane collected on the 600mhz (proton) MAS-DNP spectrometer.

Figure 4.14 shows a zoomed in view of the center of the two-dimensional ^{13}C - ^{13}C spectra, focusing on the region with the chitin resonances. The horizontal axis is the single-

quantum axis and shows the resonances at the same chemical shift value that they would appear in a one-dimensional spectra. The vertical axis is the double-quantum axis. In a one-dimensional NMR spectra the single-quantum transition of an isolated spin is a transition between just two energy states, so the state has two possible values. A double-quantum transition requires the spins of two adjacent nuclei to flip simultaneously. The energy required to cause both nuclei to transition is approximately the sum of the energy required for each individual nuclei to transition. That energy corresponds to the sum of the chemical shifts of the resonances for those nuclei. For example the C1 carbon and C2 carbon are adjacent and have a chemical shift of 104 and 55 ppm, respectively. The double-quantum transition of both nuclei occurs at a chemical shift of approximately 159 ppm. In the case of the C3 carbon at 72 ppm, it could be paired with its adjacent neighbors of either C2 at 55 ppm or C4 at 82 ppm. In the double quantum domain two signals are observed for the C3 carbon corresponding to the two pair options. The two sums of these pairs are 127 ppm for C2 and C3 and 154 ppm for C3 and C4. These can be seen in the double quantum domain as two distinct resonances at approximately 127 and 154 ppm that correspond to and overlap at the same single resonance at approximately 72 ppm in the single quantum domain.

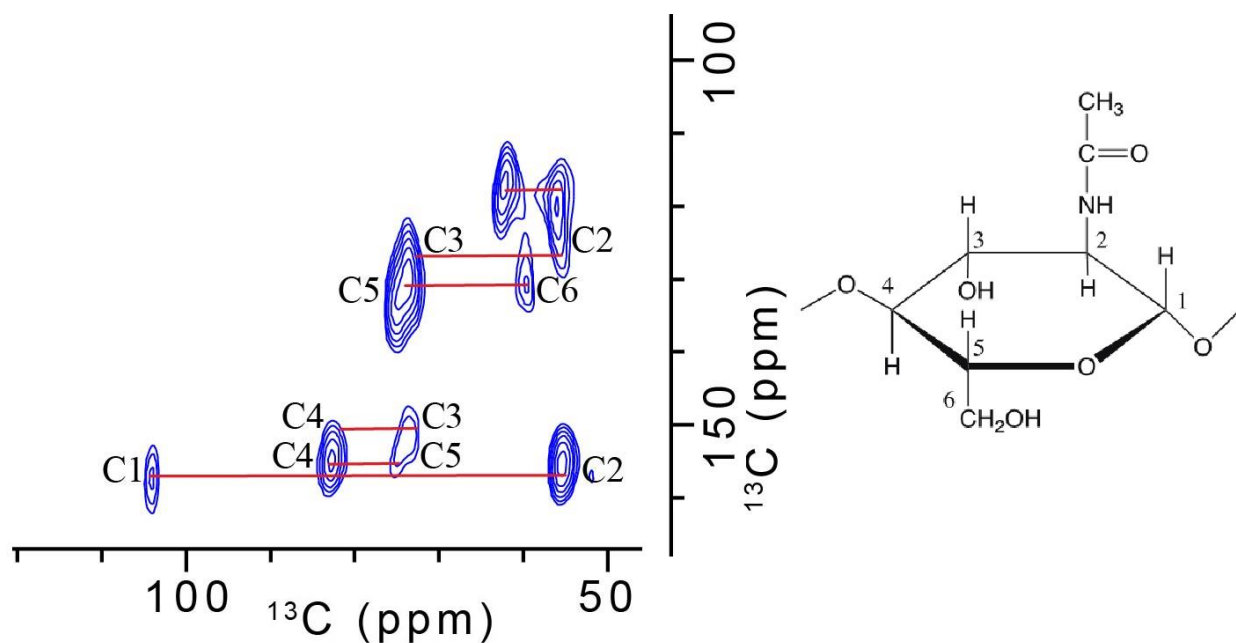


Figure 4.14 (Left) The center section of the 2d spectra in Figure 4.13 focusing on the chitin resonances that are labelled C1 through C6 according to the scheme in table 4.2. The cross peaks are shown by horizontal red lines. (Right) an image of the chitin repeat unit with the carbons labelled using the scheme from table 4.2.

^{13}C has a natural abundance of approximately 1.1% or put in decimal form 0.011 or 1 out of approximately 91 carbon atoms will be ^{13}C . In order to observe a correlation between two atoms in a multidimensional NMR experiment both atoms must be NMR active. The probabilities of each carbon being a ^{13}C are independent of each other, which means that the odds that two adjacent carbons are both ^{13}C is the square of the probability that an individual carbon is ^{13}C . The odds that two adjacent carbons are both ^{13}C is 0.000121 or 1 out of approximately every 8,264 pairs of carbon atoms will both be ^{13}C and be observable in multidimensional NMR experiments. It is for this reason that natural abundance multidimensional ^{13}C - ^{13}C NMR experiments are difficult. Typically, samples are ^{13}C enriched to mitigate this issue. However, ^{13}C enrichment of biological samples is an incredibly laborious and time-consuming process. In the case of insects, the insects would have to be bred in captivity and the isotopes would have to be introduced throughout their development through

either their food, or through direct injection. Isotopic enrichment is not a viable option for all insect species for a number of reasons. Periodical cicadas have extended 13 or 17 year lifecycles that make the time investment of breeding prohibitive, ladybugs have been observed to have cannibalistic tendencies [22], and honeybee colonies require large outdoor spaces. These results indicate that MAS-DNP can be used to make ^{13}C - ^{13}C multidimensional NMR experiments on natural abundance biological samples of insects possible with relatively low time investment.

References

1. Klowden, M. J. *Physiological Systems in Insects*; Elsevier/Academic Press: Amsterdam ; Boston, 2007.
2. Carlström D. THE CRYSTAL STRUCTURE of α -CHITIN (POLY-N-ACETYL-D-GLUCOSAMINE). *The Journal of Biophysical and Biochemical Cytology* 1957, 3 (5), 669–683. <https://doi.org/10.1083/jcb.3.5.669>.
3. Fischer, H.; Polikarpov, I.; Craievich, A. F. Average Protein Density Is a Molecular-Weight-Dependent Function. *Protein Science : A Publication of the Protein Society* 2004, 13 (10), 2825–2828. <https://doi.org/10.1110/ps.04688204>.
4. Schaefer, J.; Kramer, K. J.; Garbow, J. R.; Jacob, G. S.; Stejskal, E. O.; Hopkins, T. L.; Speirs, R. D. Aromatic Cross-Links in Insect Cuticle: Detection by Solid-State ^{13}C and ^{15}N NMR. **1987**, 235 (4793), 1200–1204. <https://doi.org/10.1126/science.3823880>.
5. Peter, M. G.; L Grün; Förster, H. CP/MAS- ^{13}C -NMR Spectra of Sclerotized Insect Cuticle and of Chitin. *Angewandte Chemie* **1984**, 23 (8), 638–639. <https://doi.org/10.1002/anie.198406381>.
6. Kramer, K. J.; Morgan, T. D.; Hopkins, T. L.; Christensen, A. M.; Schaefer, J. Solid-State ^{13}C -NMR and Diphenol Analyses of Sclerotized Cuticles from Stored Product Coleoptera. *Insect Biochemistry* **1989**, 19 (8), 753–757. [https://doi.org/10.1016/0020-1790\(89\)90056-5](https://doi.org/10.1016/0020-1790(89)90056-5).
7. Maly, T.; Debelouchina, G. T.; Bajaj, V. S.; Hu, K.-N.; Joo, C.-G.; Mak–Jurkauskas, M. L.; Sirigiri, J. R.; van der Wel, P. C. A.; Herzfeld, J.; Temkin, R. J.; Griffin, R. G. Dynamic Nuclear Polarization at High Magnetic Fields. *The Journal of Chemical Physics* **2008**, 128 (5), 052211. <https://doi.org/10.1063/1.2833582>.
8. Rossini, A. J.; Alexandre Zagdoun; Lelli, M.; Lesage, A.; Christophe Copéret; Emsley, L. Dynamic Nuclear Polarization Surface Enhanced NMR Spectroscopy. *Accounts of Chemical Research* **2013**, 46 (9), 1942–1951. <https://doi.org/10.1021/ar300322x>.
9. Qing Zhe Ni; Daviso, E.; Can, T. V.; Evgeny Markhasin; Sudheer Jawla; Swager, T. M.; Temkin, R. J.; Herzfeld, J.; Griffin, R. J. High Frequency Dynamic Nuclear Polarization. *Accounts of Chemical Research* **2013**, 46 (9), 1933–1941. <https://doi.org/10.1021/ar300348n>.
10. Lee, D.; Hediger, S.; Gaël De Paëpe. Is Solid-State NMR Enhanced by Dynamic Nuclear Polarization? *Solid State Nuclear Magnetic Resonance* **2015**, 66-67, 6–20. <https://doi.org/10.1016/j.ssnmr.2015.01.003>.

11. Rankin, A. G. M.; Trébosc, J.; Pourpoint, F.; Amoureux, J.-P.; Lafon, O. Recent Developments in MAS DNP-NMR of Materials. *Solid State Nuclear Magnetic Resonance* **2019**, *101*, 116–143. <https://doi.org/10.1016/j.ssnmr.2019.05.009>.
12. Lilly Thankamony, A. S.; Wittmann, J. J.; Kaushik, M.; Corzilius, B. Dynamic Nuclear Polarization for Sensitivity Enhancement in Modern Solid-State NMR. *Progress in Nuclear Magnetic Resonance Spectroscopy* **2017**, *102-103*, 120–195. <https://doi.org/10.1016/j.pnmrs.2017.06.002>.
13. Takahashi, H.; Lee, D.; Dubois, L.; Bardet, M.; Hediger, S.; Gaël De Paëpe. Rapid Natural-Abundance 2D¹³C-¹³c Correlation Spectroscopy Using Dynamic Nuclear Polarization Enhanced Solid-State NMR and Matrix-Free Sample Preparation. *Angewandte Chemie International Edition* **2012**, *51* (47), 11766–11769. <https://doi.org/10.1002/anie.201206102>.
14. Rossini, A. J.; Alexandre Zagdoun; Franziska Simone Hegner; Schwarzwälder, M.; Gajan, D.; Christophe Copéret; Lesage, A.; Emsley, L. Dynamic Nuclear Polarization NMR Spectroscopy of Microcrystalline Solids. **2012**, *134* (40), 16899–16908. <https://doi.org/10.1021/ja308135r>.
15. Takahashi, H.; Hediger, S.; De Paëpe, G. Matrix-Free Dynamic Nuclear Polarization Enables Solid-State NMR 13C–13C Correlation Spectroscopy of Proteins at Natural Isotopic Abundance. *Chemical Communications* **2013**, *49* (82), 9479. <https://doi.org/10.1039/c3cc45195j>.
16. Smith, A. N.; Märker, K.; Hediger, S.; Gaël De Paëpe. Natural Isotopic Abundance ¹³C and ¹⁵N Multidimensional Solid-State NMR Enabled by Dynamic Nuclear Polarization. *Journal of Physical Chemistry Letters* **2019**, *10* (16), 4652–4662. <https://doi.org/10.1021/acs.jpcclett.8b03874>.
17. Craig, H. C.; Blamires, S. J.; Sani, M.; Kasumovic, M. M.; Rawal, A.; Hook, J. M. DNP NMR Spectroscopy Reveals New Structures, Residues and Interactions in Wild Spider Silks. *Chemical Communications* **2019**, *55* (32), 4687–4690. <https://doi.org/10.1039/c9cc01045a>.
18. Zhao, W.; Kirui, A.; Fabien Deligey; Mentink-Vigier, F.; Zhou, Y.; Zhang, B.; Wang, T. Solid-State NMR of Unlabeled Plant Cell Walls: High-Resolution Structural Analysis without Isotopic Enrichment. *Biotechnology for Biofuels* **2021**, *14* (1). <https://doi.org/10.1186/s13068-020-01858-x>.
19. Perras, F. A.; Luo, H.; Zhang, X.; Mosier, N. S.; Pruski, M.; Abu- Omar, M. M. Atomic-Level Structure Characterization of Biomass Pre- and Post-Lignin Treatment by Dynamic Nuclear Polarization-Enhanced Solid-State NMR. *Journal of Physical Chemistry A* **2017**, *121* (3), 623–630. <https://doi.org/10.1021/acs.jpca.6b11121>.

20. Geiger, Y.; Gottlieb, H. E.; Ümit Akbey; Hartmut Oschkinat; Goobes, G. Studying the Conformation of a Silaffin-Derived Pentalysine Peptide Embedded in Bioinspired Silica Using Solution and Dynamic Nuclear Polarization Magic-Angle Spinning NMR. *Journal of the American Chemical Society* **2016**, *138* (17), 5561–5567. <https://doi.org/10.1021/jacs.5b07809>.
21. Johnson, R. L.; Schmidt-Rohr, K. Quantitative Solid-State ¹³C NMR with Signal Enhancement by Multiple Cross Polarization. *Journal of Magnetic Resonance* **2014**, *239*, 44–49. <https://doi.org/10.1016/j.jmr.2013.11.009>.
22. Tayeh, A.; Estoup, A.; Lombaert, E.; Guillemaud, T.; Kirichenko, N.; Lawson-Handley, L.; De Clercq, P.; Facon, B. Cannibalism in Invasive, Native and Biocontrol Populations of the Harlequin Ladybird. *BMC Evolutionary Biology* 2014, *14* (1), 15. <https://doi.org/10.1186/1471-2148-14-15>.

Chapter 5 NMR of Chitin

We decided to extract and purify chitin from cicada exuvia to use as a reference of pure chitin, for comparison with other spectra. However, spectra of purified chitin taken utilizing DNP at 100°K was markedly different than spectra of purified chitin taken at room temperature approximately 300°K as shown in Figure 5.1. Some of these differences could be explained by the higher quality of spectra generated at 100°K with DNP, however some of the differences cannot.

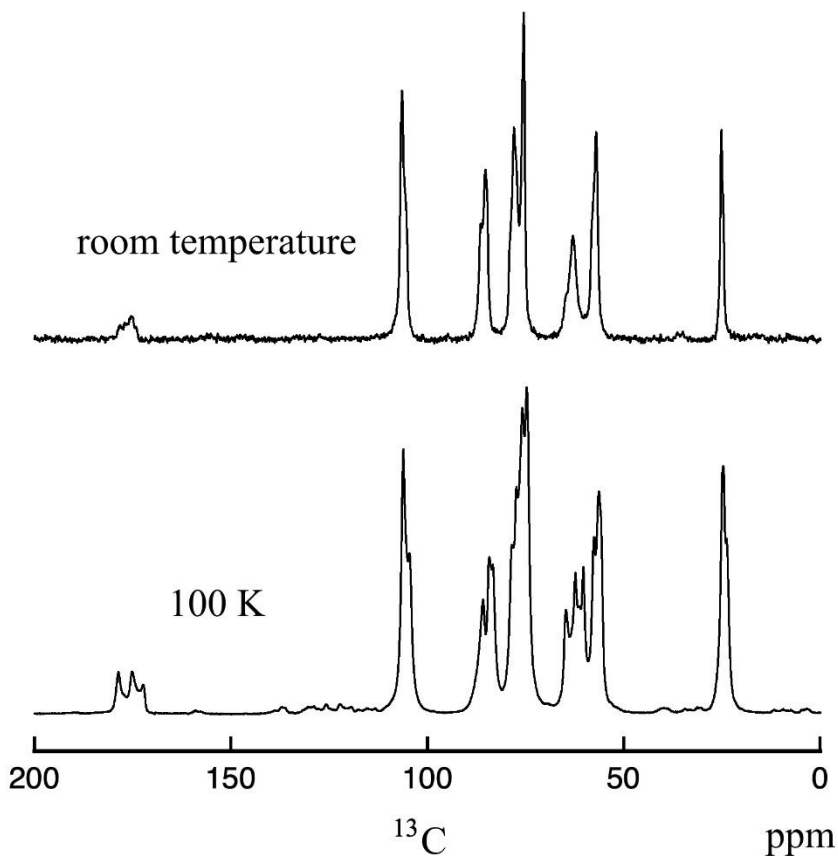


Figure 5.1 NMR spectra of purified chitin at room temperature approximately 300°K and at 100°K

There are clearly some low energy conformations that can take place. Of particular note, are the additional resonances for the C6 carbon and the carbonyl carbon at approximately 63 ppm and 175 ppm respectively. At both resonance locations a new peak has emerged where in previous spectra at 100k there was none as shown in Figure 5.2. Importantly the peak generated in both locations is at a lower ppm value upfield to the right of the main reference peaks. Peaks that are upfield correspond to a higher degree of electronic shielding, which means that the atoms that correspond to the newly generated peaks have a higher average electron density around them than the ones corresponding to the peaks to their left. For example, the chemical shift of a carbonyl carbon decreases as the length of the hydrogen bond to that carbon's oxygen increases [1]. At the cold temperature of 100°K the average energy of the chitin is much lower which allows it to occupy low configurations for substantial lengths of time and lower strength longer hydrogen bonds can be formed. At higher temperatures, there is too much thermal energy for hydrogen bonds to stay trapped in a local energy minimum.

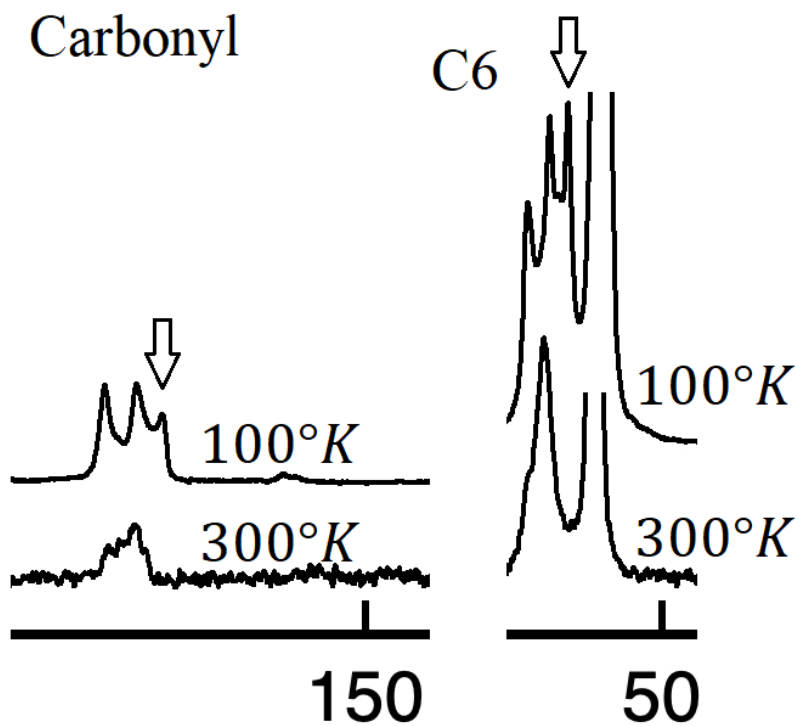


Figure 5.2 Two zoomed in and cutout portions of the spectra from both the 100°K and 300°K spectra in Figure 5.1 highlighting the Carbonyl and C6 resonances at approximately 172 ppm and 60 ppm respectively. The new peaks that appear upfield in the 100°K spectrum are identified with arrows.

Chitin occurs naturally in three different polymorph configurations α , β , and γ . α -Chitin is by far the most common polymorph of chitin found in numerous forms of plant and animal life including crustaceans and in the cuticle of insects [2,3].

Previously published X-ray diffraction studies [4] of α -Chitin show that crystal structure of α -Chitin at 100°K when compared to 300°K appear to be the same. Table 5.1 and Figure 5.3 summarize the dimensions of the chitin unit cell at 100°K and 300°K .

Unit cell parameter	100°K (nm)	300°K (nm)
a	0.4715 ± 0.008	0.4749 ± 0.007
b	1.878 ± 0.017	1.889 ± 0.014
c	1.030 ± 0.010	1.033 ± 0.010

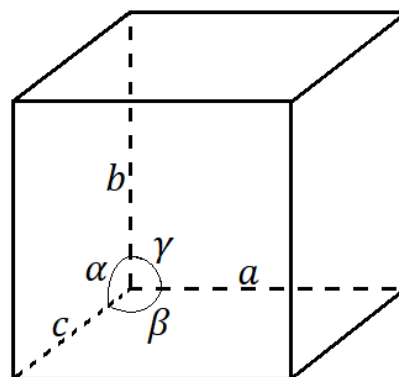


Figure 5.3 Diagram of a crystal unit cell with the dimensions a, b, c and the angles α, γ, β denoted.

Table 5.1 α -Chitin unit cell parameters at 100°K and 300°K . For both temperature conditions $\alpha = \gamma = \beta = 90^\circ$ from [4].

Figure 5.4 shows the four different crystal structures of α -Chitin at both 100°K and 300°K and with the C6-O bond in the A and B configuration. Aside from the C6-O bond orientation the structures are all practically identical. However it is important to point out that X-ray diffraction experiments cannot easily determine the position of hydrogen atoms, so parameters such as hydroxyl bond orientations cannot be known for certain.

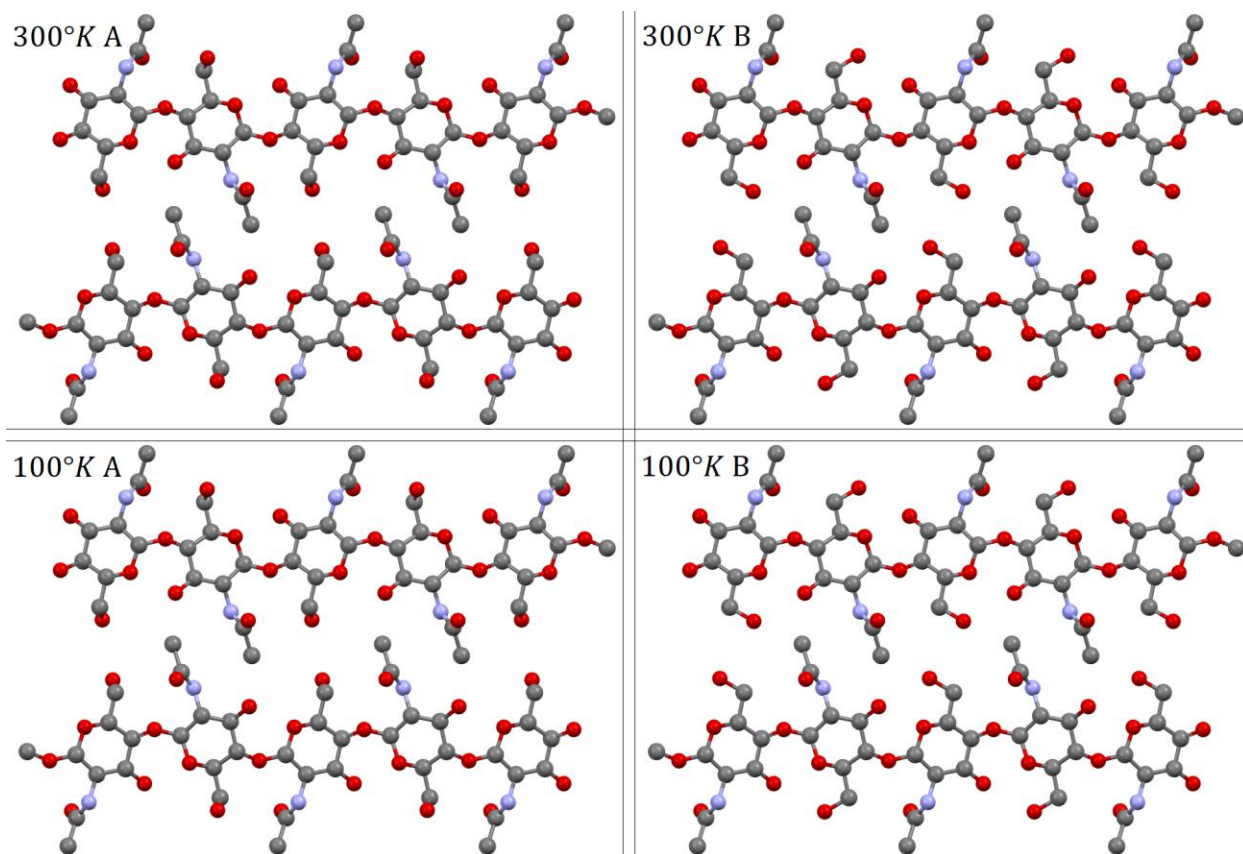


Figure 5.4 Structure of α -Chitin at 100°K and 300°K with both conformations (A and B) of the C6-O bond orientation at both temperatures from [4].

In that same work [4] Sikorski *et al.* determined that C6-O bond orientation has two preferred configurations at both 100°K and 300°K. Those two configurations A and B facilitate different hydrogen bond configurations that have an occupancy of approximately 60:40 A:B. This binary distribution is supported by the 300°K ^{13}C CPMAS NMR spectrum as the C6 resonance at approximately 60 ppm has an identifiable shoulder that could indicate two populations are present.

While there may be evidence supporting the two-population model of the C6-O bond orientation and the corresponding hydrogen bonds at 300°K, neither the 300°K or the 100°K

crystal structure and their calculated hydrogen bonds can explain the third peak that appears upfield at either the carbonyl or C6 site.

References

1. Asakawa, N.; Kuroki, S.; Kurosu, H.; Ando, I.; Shoji, A.; Ozaki, T. Hydrogen-Bonding Effect on Carbon-13 NMR Chemical Shifts of L-Alanine Residue Carbonyl Carbons of Peptides in the Solid State. **1992**, *114* (9), 3261–3265.
<https://doi.org/10.1021/ja00035a016>.
2. Rinaudo, M. Chitin and Chitosan: Properties and Applications. *Progress in Polymer Science* **2006**, *31* (7), 603–632. <https://doi.org/10.1016/j.progpolymsci.2006.06.001>.
3. LAVALL, R.; ASSIS, O.; CAMPANAFILHO, S. β -Chitin from the Pens of Loligo Sp.: Extraction and Characterization. *Bioresource Technology* **2007**, *98* (13), 2465–2472.
<https://doi.org/10.1016/j.biortech.2006.09.002>.
4. Sikorski, P.; Hori, R.; Wada, M. Revisit of α -Chitin Crystal Structure Using High Resolution X-Ray Diffraction Data. *Biomacromolecules* 2009, *10* (5), 1100–1105.
<https://doi.org/10.1021/bm801251e>.

Chapter 6 Summary and Important findings

The textbook model of insect wing formation [1] indicates that the formation of an insect's wing would leave the membrane of that wing to be free of chitin. We have found this to be not the case, and the wing membranes of cicadas, ladybugs, honeybees, and amber phantom butterflies do contain chitin. Moreover, the relative contribution of the chitin content to protein and lipid content varies from species to species. These differences indicate that the underlying chemical composition, and consequently the biological mechanisms that create these insect wings are different from species to species.

In addition, it has been determined that the crystal structure of chitin undergoes conformational changes at low temperatures. These changes are not detectable in X-ray crystallography spectra but are detectable using DNP-MAS Solid State NMR spectroscopy.

We have shown that MAS-DNP can produce high quality ^{13}C CPMAS spectra and ^{13}C - ^{13}C DQ/SQ correlation spectra with only a few milligrams of natural abundance sample within a reasonable amount of scan time.

These findings are worth further investigation because insects play an important role in the biosphere that supports life on Earth. A more sophisticated understanding of these differences in the chemical composition of insect wings could be exploited in the future to create pesticides that inhibit wing growth in specific species of undesired or invasive insects, and spare other species of insects. Insect species that spread disease, such as malaria spreading mosquitos *Anopheles stephensi*, [2] or species that cause famine such as the desert locust *Schistocerca gregaria*, [3] would be far less capable of harm if their ability to fly was hindered or eliminated.

In addition, further study of insect wing structure and chemical composition could provide pathways to the development of ultralight and tough materials for numerous applications. Such applications include Micro Aerial Vehicles [4], bactericidal [5], and hydrophobic surfaces [6].

References

1. Klowden, M. J. *Physiological Systems in Insects*; Elsevier/Academic Press: Amsterdam ; Boston, 2007.
2. Mnzava, A.; Monroe, A. C.; Okumu, F. Anopheles Stephensi in Africa Requires a More Integrated Response. *Malaria Journal* **2022**, *21* (1). <https://doi.org/10.1186/s12936-022-04197-4>.
3. Smith, C. W.; Herbert, R.; Wootton, R. J.; Evans, K. E. The Hind Wing of the Desert Locust (*Schistocerca Gregaria* Forskal). II. Mechanical Properties and Functioning of the Membrane. *Journal of Experimental Biology* **2000**, *203* (19), 2933–2943. <https://doi.org/10.1242/jeb.203.19.2933>.
4. Song, F.; Yan, Y.; Sun, J. Review of Insect-Inspired Wing Micro Air Vehicle. *Arthropod Structure & Development* **2022**, 101225. <https://doi.org/10.1016/j.asd.2022.101225>.
5. Román- Kustas, J.; Hoffman, J. B.; Reed, J. H.; Gonsalves, A. E.; Oh, J.; Li, L.; Hong, S.; Jo, K. D.; Dana, C. E.; Miljkovic, N.; Cropek, D. M.; Alleyne, M. Molecular and Topographical Organization: Influence on Cicada Wing Wettability and Bactericidal Properties. *Advanced Materials Interfaces* **2020**, *7* (10), 2000112. <https://doi.org/10.1002/admi.202000112>.
6. Nguyen, S.; Webb, H.; Mahon, P.; Crawford, R.; Ivanova, E. Natural Insect and Plant Micro-/Nanostructured Surfaces: An Excellent Selection of Valuable Templates with Superhydrophobic and Self-Cleaning Properties. *Molecules* **2014**, *19* (9), 13614–13630. <https://doi.org/10.3390/molecules190913614>.